creative commons
COMMONS DEED

저작자표시-비영리-동일조건변경허락 2.0 대한민국

이용자는 아래의 조건을 따르는 경우에 한하여 자유롭게

- 이 저작물을 복제, 배포, 전송, 전시, 공연 및 방송할 수 있습니다.
- 이차적 저작물을 작성할 수 있습니다.

다음과 같은 조건을 따라야 합니다:

저작자표시. 귀하는 원저작자를 표시하여야 합니다.

비영리. 귀하는 이 저작물을 영리 목적으로 이용할 수 없습니다.

동일조건변경허락. 귀하가 이 저작물을 개작, 변형 또는 가공했을 경우에는, 이 저작물과 동일한 이용허락조건하에서만 배포할 수 있습니다.

- 귀하는, 이 저작물의 재이용이나 배포의 경우, 이 저작물에 적용된 이용허락조건을 명확하게 나타내어야 합니다.
- 저작권자로부터 별도의 허가를 받으면 이러한 조건들은 적용되지 않습니다.

저작권법에 따른 이용자의 권리는 위의 내용에 의하여 영향을 받지 않습니다.

이것은 이용허락규약(Legal Code)을 이해하기 쉽게 요약한 것입니다.

Disclaimer

dCollection

이학박사 학위 논문

Polymer Nanocomposites *via* Surface Functionalization of Nanoparticles:

Synthesis, Characterization, and Applications

나노 입자의 표면 기능화를 통한

고분자 나노복합체의 합성 및 분석과 응용

2014 년 8 월

서울대학교 대학원

화학부 무기화학전공

김 영 재

Ph. D. Dissertation

Polymer Nanocomposites *via* Surface Functionalization of Nanoparticles: Synthesis, Characterization, and Applications

Supervisor : Professor Jin-Kyu Lee

Major : Inorganic Chemistry

August 2014

By Young-Jae Kim

Department of Chemistry

The Graduate School

Seoul National University

Abstract

Polymer Nanocomposites *via* Surface Functionalization of Nanoparticles: Synthesis, Characterization, and Applications

Young-Jae Kim

Department of Chemistry, Inorganic Chemistry

The Graduate School

Seoul National University

Nanoparticles have been extensively studied because they possess novel properties that come from the quantum effect and a high surface area to volume ratio. Among the many interesting applications of nanoparticles, polymer nanocomposites have been studied extensively because nano-sized inorganic materials are expected to effectively enhance the thermal, mechanical, and electrical properties of polymers without sacrificing the advantages of polymers such as flexibility and easy processability.

In this thesis, various polymer nanocomposites were fabricated by incorporating nanoparticles *via* surface functionalization with a ligand that has a structure similar to polymer repeating unit in order to enhance compatibility

between polymer and nanoparticle. As a result, nanoparticles were successfully incorporated in polymer matrices without aggregation. Various metal oxide such as SiO_2, TiO_2 and $BaTiO_3$ were used as nanofiller due to their high thermal stability, mechanical properties, and outstanding electrical properties (high-*k*). Thermal, mechanical, and electrical properties of polymer nanocomposites were investigated depending on the content of nanoparticles. Also polymer nanocomposite with enhanced electrical properties was applied to an organic thin film transistor. The thesis chapters are organized by the following.

Chapter 1 briefly describes the research background of polymer nanocomposites, categorization of synthetic methods of polymer nanocomposites, surface modification of nanoparticles, and the application of polymer nanocomposites.

In Chapter 2, SiO_2-Triacethylcellulose (TAC) nanocomposite films having up to 40 wt% of incorporated silica nanoparticles were successfully fabricated by deliberately designing a surface ligand that has a structure similar to that of TAC repeating units and effectively modifying the surface of silica nanoparticles through chemical bonding. The thermal properties including glass transition temperature (T_g), crystallization temperature (T_c), and melting temperatures (T_m) and optical properties of SiO_2-TAC nanocomposite were investigated.

In Chapter 3, SiO_2-polyimide (PI) nanocomposites were prepared by surface

modification of silica nanoparticles in order to create structural similarity between the polyimide and the SiO_2 surface. SiO_2-PI nanocomposites showed enhanced processability (low glass transition temperature), thermal (coefficient of thermal expansion) and mechanical (hardness and modulus) properties.

In Chapter 4, TiO_2-polyvinylphenol (PVP) and $BaTiO_3$-PVP nanocomposites were successfully fabricated by ligand exchange with 4-hydroxybenzoic acid, which is similar in structure to the repeat unit in PVP. The dielectric constant of PVP nanocomposites was increased by high-k TiO_2 and $BaTiO_3$. As a result, organic thin film transistors (OTFTs) with TiO_2-PVP nanocomposites dielectric exhibited enhanced device performance.

Keywords: polymer nanocomposite, nanoparticle, surface modification, thermal and mechanical properties, electrical property, gate insulator

Student Number: 2008-20310

Contents

List of Figures

Chapter 1

Chapter 2

Chapter 3

Chapter 4

APPENDIX

Chapter 1

Chapter 2

Chapter 3

List of Scheme

Chapter 2

Chapter 3

Chapter 4

Part 1.

Appendix

Chapter 1

Chapter 2

Chapter 3

List of Tables

Chapter 1

Chapter 2

Chapter 3

Chapter 4

Chapter 1.

Research Background

1.1 Introduction

Polymer/inorganic composite materials are defined as polymer in which inorganic fillers are incorporated. When inorganic filler has nanosize, it refers to polymer nacomposite. Polymer nanocomposites have been receiving great attention for a long time. Since inorganic nanomaterials can provide desirable properties such as high refractive index,[1] dielectric constant,[2] electrical conductivity,[3] thermal conductivity,[3] and hardness[4] to polymers without sacrificing advantages of polymer such as flexibility and processability when used as complementary additive components. Various inorganic nanomaterials such as clay, semiconducting nanocrystals, metal nanoparticles, and ceramic nanoparticles have been employed for those purposes.

In situ and *ex situ* synthesis are the primary methods used to prepare polymer nanocomposites.[1] *In situ* synthesis methods generate nanoparticles inside a polymer matrix by *in situ* sol-gel reactions[5] or *in situ* gas-solid reactions,[6] and therefore, one-step fabrication is possible. On the other hand, in *ex situ* synthesis methods, pre-made nanoparticles are blended with polymers, or the polymers are synthesized with the nanoparticles.[7-8] Therefore, the properties of the nanoparticles can be easily controlled. Among *ex situ* synthesis methods, blending is the simplest and the most convenient way to prepare polymer nanocomposites.[4] However, nanoparticles tend to aggregate during the mixing, which leads to deterioration of the thermal, mechanical, and optical properties of the resulting composites. Surface modification of nanoparticle by chemical and/or physical interactions is generally employed to solve these problems.[4] The synthetic method of polymer nanocomposites, surface modification of nanopraticles, and characterization and properties of nanocomposites are discussed more detail in Section 1.2, 1.3 and 1.4, respectively. Various applications of polymer nanocomposites are described in Section 1.5.

1.2 Synthetic method of polymer nanocomposites

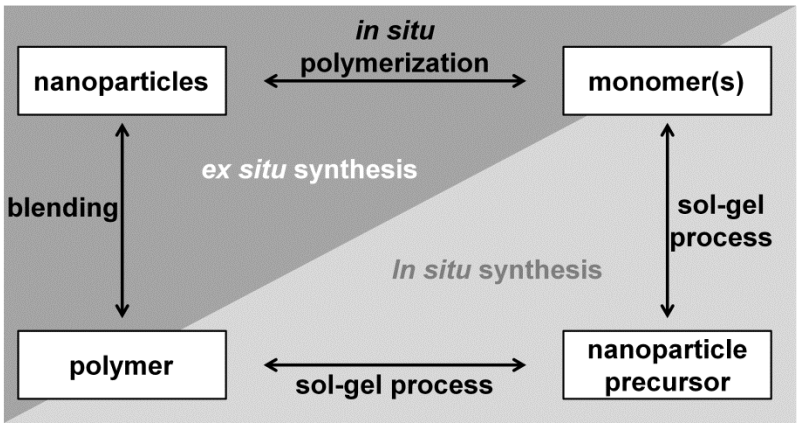

Figure 1.1. The general synthetic method to prepare polymer nanocomposites[9]

The synthetic method of polymer nanocomposites is categorized into *in situ* and *ex situ* synthesis methods according to the starting materials. In *in situ* synthesis method, nucleation and growth of nanoparticles are occurred inside polymer matrix or with polymerization. On the other hand, in *ex situ* method, pre-synthesized nanoparticles are blended with polymer, or the polymers are synthesized with the nanoparticles.

In situ synthesis methods, the nanoparticles are generated from their respective nanoparticle precursors inside a polymer by *in situ* sol-gel reactions[5] or *in situ* gas-solid reactions[6]. The sol-gel reaction, in particular, is widely used method to fabricate nanocomposites and is performed with monomer or in presence of polymer which have functional group to improve interaction with three-dimensional oxide network (inorganic phase)[1] by chemical bonding[10] or ionic interaction[11]. It is well known that the sol-gel reaction is based on the hydrolysis and condensation of metal alkoxides

(Figure 1.2a, b).[12] The reaction rate of metal alkoxides in sol-gel process is depends on many factors including the reaction temperature, the nature of solvent, and catalyst, which affect domain size of inorganic phase and interaction between organic and inorganic phase. Thus it is difficult to ensure full control of the shape, size, size distribution, crystallinity, and surface properties of the nanoparticles during the reaction. Moreover, the thermal, mechanical, and optical properties of the resulting nanocomposites can be influenced by unreacted reactants or byproduct, which is usually considered to be a main drawback of *in situ* methods.[1]

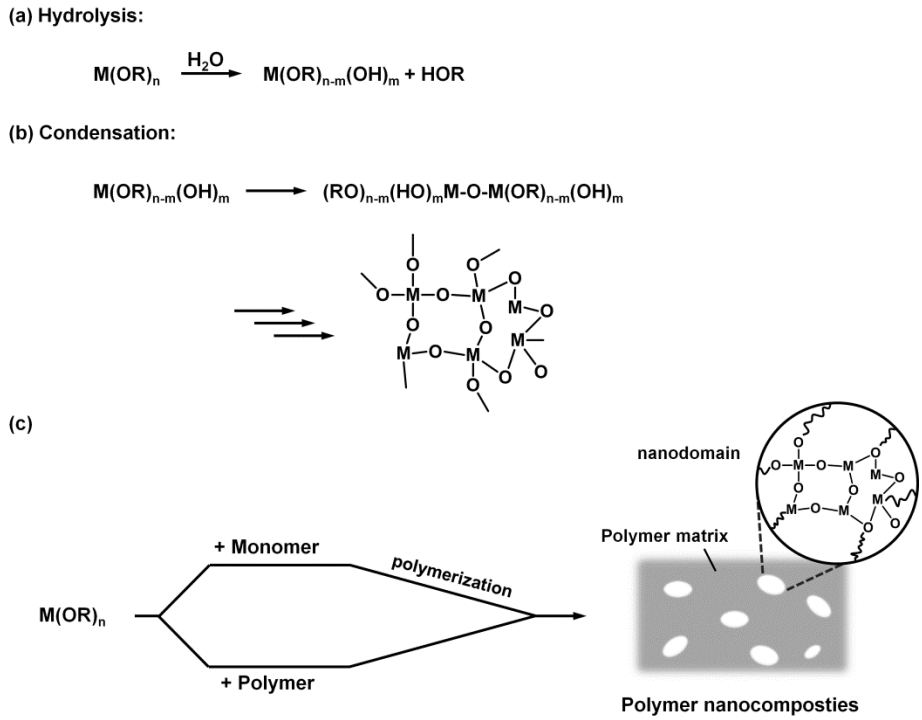

Figure 1.2. Sol-gel reaction[12] and *in situ* sol-gel process for preparation of polymer nanocomposite[1].

Another important method for fabrication of polymer nanocomposites is *ex-situ* synthetic method: polymerization of monomer in presence of nanomaterials (*in situ* polymerization) or incorporating pre-made nanomaterials into polymer the matrix (blending)[1]. In *in situ* polymerization process, three continuous steps are generally acquired. First, the nanomaterials are pre-modified with appropriate ligands and then modified nanomaterials are dispersed into monomers. The mixture of modified nanomaterials and monomers is followed polymerization, and then the nanocomposites are generated during polymerization. Therefore, the dispersion of nanomaterials and the adhesion between polymer and nanomaterials are the main factors to determine properties of resulting nanocomposite.[9]

Blending method is the most conventional and simplest method for preparing polymer nanocomposites. Melt blending and solution blending are commonly used method. In melt process, nanomaterials are dispersed into melted polymer and then polymer nanocomposites are obtained by extrusion.[13] Solution blending is liquid-state processing method that nanoparticles and dissolved polymer are mixed in solvent.[9] However, the nanoparticles tend to aggregate in large agglomers during the mixing process due to their high surface energy and low compatibility with polymers, which leads to deterioration of the mechanical and optical properties of the resulting composites. Thus, the key challenge with these methods are improving the compatibility of the nanoparticles with the polymer and maintaining good dispersibility within the polymer matrix.

1.3 Surface modification of nanoparticles

To improve dispersibility of nanomaterials in polymer mitrix, the surface modification of nanomaterials with appropriate molecules is essential. The surface modification of nanomaterials by chemical interaction is a useful method to improve dispersibility of nanomaterials in polymer or various liquid media. For example, $BaTiO_3$ was modified by pentafluorobenzyl phosphonic acid (PFBPA) to afford good compatibility with fluoroelastomers, poly(vinylidenefluoride-*co*-hexafluoropropylene) (P(VDF-HFP))[14]. To enhance hydrophonic interaction with the syndiotactic polypropylene matrix, Al_2O_3 nanoparticles was modified with two different silane coupling agents, (octyl) triethoxysilane and (3-chloropropyl) triethoxysilane.[15] To interact with hydroxyl groups in poly(vinyl alcohol), TiO_2 was modified with γ-aminopropyltriethoxy silane as a coupling agent.[16] To obtain SiO_2-PS and SiO_2-PMMA nanocomposites via *in-situ* polymerization, polymerization is initiated from surface of SiO_2 which are modified with (3-(2-bromopropionyl) propyl) dimethylethoxysilane and (3-(2-bromoisobutyryl)propyl) dimethylethoxysilane, in which could serve as a styrene ATRP (atomic-transfer radical polymerization) initiator and a methacrylate ATRP initiator, respectively.[17]

The common molecules used for modifying metal oxide nanoparticles are silanes, carboxylate and phosphonates. Silane coupling agent is the most used modifier agents for metal oxide surfaces[9, 18-19], especially for silica nanoparticles (Figure 1.3.). The general structure of the silane coupling agent can be represented as $RSiX_3$. The X reacts with hydroxyl groups on the SiO_2 surface through a condensation reaction, which are chloro, epoxy, and alkoxy groups. The organic group, R can be substituted with various other functional

groups in order to enhance the interaction between the polymer and the nanoparticles. This is main advantages of silane coupling agent that they can possess numerous functionalities. Surface modification of silane coupling agent is applicable to various metal oxide such as TiO_2, ZrO_2, Al_2O_3, and HfO_2.

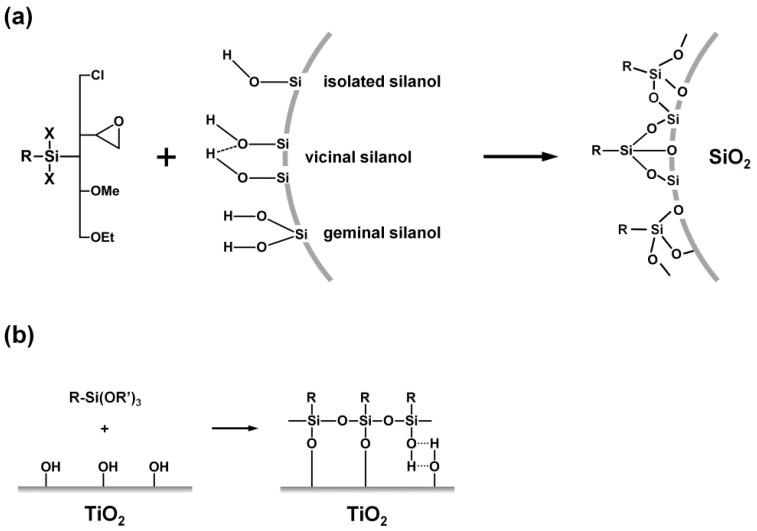

Figure 1.3. Surface modification of (a) SiO_2[9] and (b) TiO_2[19] by silane coupling agent.

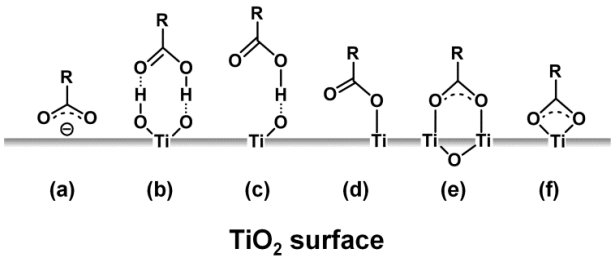

Figure 1.4. Possible binding model of carboxylate ligand on TiO_2 by adsorption and chemisorption: (a) electrostatic, (b, c) hydrogen bonding, (d) ester-like linkage, (e) bidentate bridging and (f) bidentate chelating.[20]

Carboxylate ligands are often used modifiers for modifying metal oxide nanoparticles, especially for TiO_2 nanoparticles. It is suggested that carboxylic group interact with TiO_2 by simple adsorption such as electrostatic attraction and hydrogen bonding and chemisorption through ester linkage, bridging and chelating (Figure 1.4).[20]

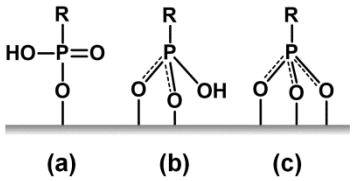

Figure 1.5. (a) Monodentate, (b) bidentate, and (c) tridentate anchorage of a phosphonate ligand on a surface of metal oxide.[21]

The modification of metal oxide surface by phosphonate can be done by mono-, bi-, and tridentate chelating (Figure 1.5.).[21] Surface modification with phosphonate is widely used for metal oxide surface such as Al_3O_3 or TiO_2. Phosphonate form more robust bonds with TiO_2 than silane coupling agent that P-O-Ti bonds more stable than Ti-O-Si under alkaline conditions. On the other hand, phosphonate ligands are not suitable for SiO_2 because Si-O-P bond are easily hydrolyzed, even under neutral conditions.[21] Thus, in order to maintain the stability of ligand on the nanoparticles surface, selection of suitable anchoring is also important.

1.4 Characterization and properties

It is well known that nanoparticles in polymer matrix have significantly impact on the properties of nanocomposites such as thermal, mechanical, electrical, and optical properties.[9] ***Thermal properties*** are the properties of materials that change with temperature. They are investigated by thermal analysis techniques including TGA (thermal gravimetric analysis), DSC (differential scanning calorimeter), TMA (thermal mechanical analysis), DMA (dynamic mechanical analysis), and so on. TGA and DSC are widely used methods to study the thermal properties of polymer nanocomposites. Thermal stability, the onset of degradation, and the percent of nanofiller in polymer matrix are demonstrated by TGA. DSC is efficiently used to investigate the thermal transition behavior of polymer nanocomposties related to molecular mobility. Glass transition temperature (T_g), crystalline temperature (T_c), and melting temperature (T_m) are determined by DSC. TMA can demonstrate the dimension stability of materials, thus, coefficient of thermal expansion (CTE) can be obtained by TMA. DMA is most useful for studying the viscoelastic behavior of the polymer as it subjected to a periodic force. The storage modulus (G'), loss modulus (G''), and tan δ ($=G''/G'$) are three important factors to determine molecular mobility transition of a polymer as it is subjected to a periodic force.

In general, nanofiller in polymer matrix hinder movement of polymer chains,[22-24] as a result thermal properties are enhanced with increasing of nanoparticles content. In some case, however, the thermal stability of the nanocomposites is not enhanced by addition of nanoparticles.[25-26] In addition, T_g of nanocomposites is affected by variety reasons such as size of nanofiller, filler loading, dispersion condition, and interfacial interaction between

nanofiller and polymer, thus, the effect of the nanofiller on the glass transition behavior of polymer is controversial.[27] In some case, enhancement of T_g is observed.[23, 28] In other cases, the polymer nanocomposites showed a depression of the T_g.[27, 29]

A reduction in coefficient of thermal expansion (CTE) by incorporating nanofiller in polymer matrices was also reported.[30-31] Polymer generally have CTEs one or two order of magnitude higher than that of ceramics.[32] Therefore, addition of ceramic nanofiller is one of most useful strategy to reduce CTE.

Traditionally, the main purpose to fabricate nanocomposites is to improve ***mechanical properties*** including tensile strength, flexural strength, hardness, modulus and stiffness because nanofiller act as reinforcing component in polymer matrix.[33-36] Tensile test is the most widely used method to determine the mechanical properties of nanocomposites. Young's modulus, tensile strength, and the elongation at break are three main parameters obtained.[9] Hardness is also important parameters to determine materials resistant against external force. Scratch hardness (resistance to fracture or plastic deformation due to friction from a sharp object), indentation hardness (resistance to plastic deformation due to impact from a sharp object), and rebound hardness (height of the bound of an object dropped on the material) are three principal types of hardness.[9]

Electrical properties of nanocomposites are associated with dielectric and conductivity properties. Conductive nanomaterials such as carbon based nanomaterials and metal nanomaterials have been used as nanofiller in polymer matrices to increase conductivity of polymer. Meanwhile, dielectric constant of nanocomposites can be achieved by incorporating high-*k* metal oxide or conductive nanomaterials.[2]

Besides that, inorganic UV-absorbers and nanomaterials having high refractive index (RI) are also used to provide ***optical properties*** such as UV-shielding effect[37] and high refractive index[1].

1.5 Applications of polymer nanocomposites

Various types of inorganic nanoparticles have been used for preparing polymer nanocomposites including metals (e.g., Al, Ni, Fe, Au, and Ag), metal oxide (e.g.,TiO_2, Al_2O_3, HfO_2, and ZnO), non-metal oxides (e.g.,SiO_2), and carbon based materials (e.g.,CNT and graphene). It is possible to provide and enhance the desired properties of the polymer nanocomposites by incorporating the appropriate nanoparticles. Resulting polymer nanocomposites have outstanding mechanical, electrical and optical properties to polymer, thus the nanocomposites can be applied to various fields, such as optics,[38] electronics,[39-41] mechanics, energy,[42-43] biology and medicine, and so on.[13, 44-45] Some of potential applications of polymer nanocomposites are listed in Table 1.1.

Table 1.1 Potential applications of polymer nanocomposites

Nanoparticle	Properties	Nanocomposties	Applications	Ref.
TiO_2	High-*k*	PVP/TiO_2	OTFTs	41
	High refractive index	PMMA/TiO_2	Optical films	38
$BaTiO_3$	High-*k*	Polyvinylalcohol/$BaTiO_3$	OTFTs	40
	Piezoelectric properties	wood cellulose fibers/$BaTiO_3$	Piezoelectric device	43
	microwave shielding properties	Polyaminlin/$BaTiO_3$	electronics	39
ZnO	Antimicrobial properties	Low density polyethylene/ZnO/Ag	orange juice package	45
SiO_2	Physicochemeical properties	Sulfonated Poly(styrene-*co*-maleic anhydride) -Poly ethylene glycol)/SiO_2	Fuel Cell	42

1.6 References

[1] Lu, C. L.; Yang, B., *J. Mater. Chem.* **2009,** *19*, 2884-2901.

[2] Ortiz, R. P.; Facchetti, A.; Marks, T. J., *Chem. Rev.* **2010,** *110*, 205-239.

[3] Jones, W. E.; Chiguma, J.; Johnson, E.; Pachamuthu, A.; Santos, D., *Materials* **2010,** *3*, 1478-1496.

[4] Zou, H.; Wu, S. S.; Shen, J., *Chem. Rev.* **2008,** *108*, 3893-3957.

[5] Schottner, G., *Chem. Mater.* **2001,** *13*, 3422-3435.

[6] Wang, J. Y.; Chen, W.; Liu, A. H.; Lu, G.; Zhang, G.; Zhang, J. H.; Yang, B., *J. Am. Chem. Soc.* **2002,** *124*, 13358-13359.

[7] Barbey, R.; Lavanant, L.; Paripovic, D.; Schuwer, N.; Sugnaux, C.; Tugulu, S.; Klok, H. A., *Chem. Rev.* **2009,** *109*, 5437-5527.

[8] Ghosh, S.; Goswami, S. K.; Mathias, L. J., *J. Mater. Chem. A* **2013,** *1*, 6073-6080.

[9] Zou, H.; Wu, S.; Shen, J., *Chem. Rev.* **2008,** *108*, 3893-3957.

[10] Hsiue, G.-H.; Kuo, W.-J.; Huang, Y.-P.; Jeng, R.-J., *Polymer* **2000,** *41*, 2813-2825.

[11] Tamaki, R.; Chujo, Y., *Chem. Mater.* **1999,** *11*, 1719-1726.

[12] Brinker, C. J.; Scherer, G. W., *Sol-gel Science: The Physics and Chemistry of Sol-gel Processing*. Academic Press: **1990**.

[13] Kango, S.; Kalia, S.; Celli, A.; Njuguna, J.; Habibi, Y.; Kumar, R., *Prog. Polym. Sci.* **2013,** *38*, 1232-1261.

[14] Kim, P.; Jones, S. C.; Hotchkiss, P. J.; Haddock, J. N.; Kippelen, B.; Marder, S. R.; Perry, J. W., *Adv. Mater.* **2007,** *19*, 1001-1005.

[15] Truong, L. T.; Larsen, Å.; Holme, B.; Diplas, S.; Hansen, F. K.; Roots, J.; Jørgensen, S., *Surf. Interface. Anal.* **2010,** *42*, 1046-1049.

[16] Mallakpour, S.; Barati, A., *Prog. Org. Coat.* **2011,** *71*, 391-398.

[17] von Werne, T.; Patten, T. E., *J. Am. Chem. Soc.* **2001,** *123*, 7497-7505.

[18] Neouze, M.-A.; Schubert, U., *Monatsh. Chem. Chem. Mon.* **2008,** *139*, 183-195.

[19] Zhao, J.; Milanova, M.; Warmoeskerken, M. M. C. G.; Dutschk, V., *Colloid. Surface A* **2012,** *413*, 273-279.

[20] Weng, Y.-X.; Li, L.; Liu, Y.; Wang, L.; Yang, G.-Z., *J. Phys. Chem. B.* **2003,** *107*, 4356-4363.

[21] Mutin, P. H.; Guerrero, G.; Vioux, A., *J. Mater. Chem.* **2005,** *15*, 3761-3768.

[22] Al-Kandary, S.; Ali, A. A. M.; Ahmad, Z., *J. Appl. Polym. Sci.* **2005,** *98*, 2521-2531.

[23] Tsai, M.-H.; Huang, Y.-C.; Tseng, I. H.; Yu, H.-P.; Lin, Y.-K.; Huang, S.-L., *Thin Solid Films* **2011,** *519*, 5238-5242.

[24] Wang, H.; Xu, P.; Zhong, W.; Shen, L.; Du, Q., *Polym. Degrad. Stab.* **2005,** *87*, 319-327.

[25] Kashiwagi, T.; Morgan, A. B.; Antonucci, J. M.; VanLandingham, M. R.; Harris, R. H.; Awad, W. H.; Shields, J. R., *J. Appl. Polym. Sci.* **2003,** *89*, 2072-2078.

[26] Liu, Y.-L.; Hsu, C.-Y.; Hsu, K.-Y., *Polymer* **2005,** *46*, 1851-1856.

[27] Sun, Y.; Zhang, Z.; Moon, K.-S.; Wong, C. P., *J. Polym. Sci., Part B: Polym. Phys.* **2004,** *42*, 3849-3858.

[28] Kim, Y. J.; Ha, S. W.; Jeon, S. M.; Yoo, D. W.; Chun, S. H.; Sohn, B. H.; Lee, J. K., *Langmuir* **2010,** *26*, 7555-7560.

[29] Sun, Y.; Zhang, Z.; Wong, C. P., *Polymer* **2005,** *46*, 2297-2305.

[30] Gonzalez-Benito, J.; Castillo, E.; Caldito, J. F., *Eur. Polym. J.* **2013,** *49*, 1747-1752.

[31] Chiang, P. C.; Whang, W. T.; Tsai, M. H.; Wu, S. C., *Thin Solid Films* **2004,** *447*, 359-364.

[32] González-Benito, J.; Castillo, E.; Caldito, J. F., *Eur. Polym. J.* **2013,** *49*, 1747-1752.

[33] Jia, X. L.; Zhang, Q.; Zhao, M. Q.; Xu, G. H.; Huang, J. Q.; Qian, W. Z.; Lu, Y. F.; Wei, F., *J. Mater. Chem.* **2012,** *22*, 7050-7056.

[34] Wang, L. H.; Tian, Y.; Ding, H. Y.; Li, J. D., *Eur. Polym. J.* **2006,** *42*, 2921-2930.

[35] Dhakal, H. N.; Zhang, Z. Y.; Richardson, M. O. W., *Polym. Test.* **2006,** *25*, 846-852.

[36] Hu, Y. C.; Shen, L.; Yang, H.; Wang, M.; Liu, T. X.; Liang, T.; Zhang, J., *Polym. Test.* **2006,** *25*, 492-497.

[37] Li, S.; Toprak, M. S.; Jo, Y. S.; Dobson, J.; Kim, D. K.; Muhammed, M., *Adv. Mater.* **2007,** *19*, 4347-4352.

[38] Lee, L. H.; Chen, W. C., *Chem. Mater.* **2001,** *13*, 1137-1142.

[39] Saini, P.; Arora, M.; Gupta, G.; Gupta, B. K.; Singh, V. N.; Choudhary, V., *Nanoscale* **2013,** *5*, 4330-4336.

[40] Schroeder, R.; Majewski, L. A.; Grell, M., *Adv. Mater.* **2005,** *17*, 1535-1539.

[41] Chen, F. T.; Chu, C. W.; He, J.; Yang, Y.; Lin, J. L., *Appl. Phys. Lett.* **2004,** *85*, 3295-3297.

[42] Saxena, A.; Tripathi, B. P.; Shahi, V. K., *J. Phys. Chem. B.* **2007,** *111*, 12454-12461.

[43] Mahadeva, S. K.; Walus, K.; Stoeber, B., *ACS Appl. Mater. Inter.* **2014**.

[44] Sanchez, C.; Julian, B.; Belleville, P.; Popall, M., *J. Mater. Chem.* **2005,** *15*, 3559-3592.

[45] Emamifar, A.; Kadivar, M.; Shahedi, M.; Soleimanian-Zad, S., *Food Control* **2011,** *22*, 408-413.

Chapter 2.

Fabrication of SiO_2-Triacetylcellulose (TAC) Nanocomposites by Surface Modification of Silica Nanoparticles

2.1 Abstract

SiO_2-Triacethylcellulose (TAC) nanocomposite films having up to 40 wt% of incorporated silica nanoparticles were successfully fabricated by deliberately designing a surface ligand that has a structure similar to that of polymer repeating units and effectively modifying the surface of silica nanoparticles through chemical bonding. Cross-sectional TEM analysis reveals no significant aggregation in all SiO_2-TAC nanocomposite films. Thermal analysis results suggested that SiO_2-TAC nanocomposites had higher T_g and T_c values as compared to neat TAC, and the increase in T_g and T_c was affected by the silica content. The transparency of all the nanocomposite films was over 80% in the visible range, confirming the excellent compatibility of nanoparticles with TAC. In this study, the interaction between nanoparticles and polymer matrices was enhanced by modifying the surface of nanoparticles with a ligand that has a structure similar to that of polymer repeating units.

2.2 Introduction

Nanoparticles have been extensively studied because they possess novel properties that are attributed to their high surface areas and enhanced reactivity of surface atoms; such properties have never been observed in bulk materials. Among the many interesting applications of nanoparticles, polymer composites with nanoparticles have been studied extensively because nano-sized materials are expected to effectively enhance the physical properties of polymers, such as toughness, stiffness, scratch resistance, and heat resistance, via the introduction of a relatively large amount of nano-sized filler materials as compared to conventional micron-sized ones, without causing phase separation. It has been reported that various inorganic materials such as exfoliated clay,[1] carbon nanotubes,[2] semiconductor nanocrystals,[3] silica nanoparticles,[4] and metal nanoparticles[5] could be used as nanofillers. However, these materials tend to aggregate due to their high surface energy, although most nanoparticles have an original diameter of less than 100 nm, thereby hampering their dispersion in a polymer matrix. Therefore, in order to fabricate nanocomposites without any aggregation, which can deteriorate the physical and optical properties of polymers, it is very critical to deliberately design the surface ligands and to develop a technique for the surface-modification of nanoparticles.

The conventional and simple way to prepare polymer nanocomposites is to direct mix nanoparticles with polymers; however, this normally causes serious aggregation problems. In order to increase the interaction between the polymer and the nanoparticles, surface modification of nanoparticles is usually carried out by employing surfactants or macromolecules, modifying them directly using silane coupling agent, or grafting polymer chains with similar chemical structures.[4] Although it cannot be easily used for other

polymers, surface-initiated polymerization was used with several well-known polymers such as polystyrene,[6-7] poly(methyl methacrylate),[7-8] poly(ethylene terepthalate),[9] and poly(vinyl chloride)[10] to graft polymer chains on nanoparticle surfaces. Direct surface-modification of nanoparticle surfaces, especially for silica nanoparticles, using the silane coupling agent, $RSi(OR')_3$,[11-12] has been actively studied. The organic group R can be substituted with various other functional groups in order to enhance the interaction between the polymer and the nanoparticles.

A film of triacetyl cellulose (TAC), a cellulose derivative containing ~60 mol% of acetylated groups, has been widely used as protective film for polarizing plates,[13] photographic film, and as an optical compensation film in liquid-crystal display (LCD) manufacturing due to its high transparency, smoothness, and optical isotropy. To prevent the shrinkage of a polarizing film (PVA) and evaporation of polarizing elements such as iodine or dye, protective films fabricated in a sandwich form require good heat- and moisture-resistant properties.[13] Silica nanoparticles are expected to enhance the properties of TAC without degrading its optical characteristics if their effective size is smaller than 100 nm by reducing light-scattering in the range of visible light.[14-15] However, probably due to the rather complex chemical structure of TAC, homogeneously well-dispersed nanocomposites consisting of TAC and nanoparticles have never been realized thus far.

In this research, the surface of silica nanoparticles are modified through the chemical bonding of $RSi(OR')_3$, a compound that has a structure similar to that of polymer repeating units. The strong interaction between the surface-modified silica nanoparticles and the TAC matrix resulted in an increase in the amount of incorporated nanoparticles to approximately 40 wt%, without causing any significant degradation in the optical characteristics of TAC. We

believe that this approach, which modifies the surface of nanoparticles using organic ligands that have a structure similar to that of polymer repeating units, can be used as a general method that can be applied to various polymers to prepare useful organic-inorganic nanocomposites.

2.3 Experimental Section

D-glucose, TMS (trimethoxysilane), DMAP (4-(dimethylamino) pyridine), allyl alcohol, 50WX8-400 ion exchange resin, acetic anhydrous, platinum-1,3-divinyltetramethyldisiloxane, Pt(dvs), and potassium bromide were purchased from Aldrich. Pyridine was purchased from Fluka; TAC from LG Chem.; toluene from Burdick & Jackson; TEOS (tetraethyl orthosilicate) from TCI; and $CDCl_3$ for NMR solvent from Cambridge Isotope Laboratories. All organic solvents were used without any further purification. All reactions were carried out in N_2 atmosphere.

Synthesis of allyl-2,3,4,6-tetra-O-acetyl-D-glucopyranoside (1)[16-17]

A reaction mixture of D-glucose (202.7 mg, 1.12 mmol) and 50WX8-400 ion exchange resin (202.7 mg) in allyl alcohol (4 mL) was stirred for 12 h at 70°C. After cooling the mixture to room temperature, it was filtered through a pad of Celite with methanol. After the filtration of resin and removal of the solvent *in vacuo*, colorless sticky oil was left as residue. The dried mixture and DMAP (15.0 mg) were dissolved in pyridine (7 mL). After cooling to 0°C, acetic anhydride (1.05 mL, 11.1 mmol) was added dropwise and stirred at 0°C for 10 min, and further stirred at room temperature. After 12 h, the solvent was removed and the residue was extracted with ethyl acetate and sequentially washed twice with 1N HCl and water. It was dried over anhydrous $MgSO_4$, and the solvent was removed using an evaporator. The yellowish residue was purified by silica gel column chromatography (ethyl acetate/*n*-hexane = 1/2) to afford 204.6 mg of colorless sticky oil 1 in 46.8% yield.

^{1}H NMR (500 MHz, $CDCl_3$): α-anomer; δ = 5.9 (m, 1H, C*H*=CH_2), 5.52 (t, 1H, H3), 5.3 (d, 1H, CH=C*H*$_2$), 5.2 (d, 1H, CH=C*H*$_2$), 5.1 (d, 1H, H1), 5.06

(dd, 1H, H4), 4.9 (dd, 1H, H2), 4.26 (dd, 1H, H6), 4.21(dd, 1H, C$\underline{H_2}$-CH=CH_2), 4.19-4.01 (m, 3H, H6', H5, C$\underline{H_2}$-CH=CH_2), 2.09, 2.07, 2.03, 2.01 (each s, 12H, 4×OAc), β-anomer; δ = 5.86 (m, 1H, C$\underline{H}$=CH_2), 5.3 (d, 1H, CH=C$\underline{H_2}$), 5.2 (d, 1H, CH=C$\underline{H_2}$), 5.2 (t, 1H, H3), 5.1 (t, 1H, H4), 5.02 (t, 1H, H2), 4.56 (d, 1H, H1), 4.34 (m, 1H, CH_2-CH=CH_2), 4.27 (dd, 1H, H6), 4.14 (dd, 1H, H6'), 4.09 (dd, 2H, C$\underline{H_2}$-CH=CH_2), 3.7 (m, 1H, H5), 2.09, 2.07, 2.03, 2.01 (each s, 12H, 4×OAc). ^{13}C NMR (500MHz, $CDCl_3$): α-anomer; δ = 169.7, 170.2, 170.3, 170.7 (4×O$\underline{C}$OCH_3), 133.2 ($\underline{C}$H=CH_2), 118.3 (CH=$\underline{C}H_2$), 118.3 (CH=$\underline{C}H_2$), 95.0 (C1), 70.9 (C2), 70.3 (C3), 68.9 ($\underline{CH_2}$-CH=CH_2), 68.7 (C4), 67.5 (C5), 62.0 (C6), 20.8 (4×OCO$\underline{C}H_3$). β-anomer; δ = 169.5, 169.6, 170.5, 170.8 (4×O$\underline{C}$OCH_3), 133.5 ($\underline{C}$H=CH_2), 117.8 (CH=$\underline{C}H_2$), 99.7 (C1), 73.0 (C3), 71.9 (C5), 71.5 (C2), 70.2 ($\underline{CH_2}$-CH=CH_2), 68.6 (C4), 62.1 (C6), 20.8 (4×OCO$\underline{C}H_3$). Anal. Found: C, 52.30; H, 6.23%. Calcd. for $C_{17}H_{24}O_{10}$: C, 52.57; H, 6.23%

Synthesis of (trimethoxysilyl)propyl-2,3,4,6-tetra-O-acetyl-D-glucopyranoside (TSPAG, 2)[18-19]

Allyl-2,3,4,6-tetra-O-acetyl-D-glucopyranoside (2.98 g, 7.7 mmol) was dissolved in anhydrous toluene, and TMS (11.5 mmol, 1.5 equiv.), and a catalytic amount of Karstedt solution, Pt(dvs), was added to this mixture. This mixture was stirred at 65°C for one day (Be careful not to set temperature above 70℃, because Karstedt solution decomposes and turned dark brown solution[18]). After cooling the mixture to room temperature, activated carbon was added to it and stirred for 10 min. The mixture was then immediately filtered through a pad of Celite. Solvent and the excess TMS were removed *in*

vacuo. (Trimethoxysilyl)propyl-2,3,4,6-tetra-O-acetyl-D-glucopyranoside was obtained as colorless sticky oil (3.55 g, 90.7%) and kept in N_2 atmosphere.

^{1}H NMR (500 MHz, $CDCl_3$): δ = 5.49 (t, 1H, H3α), 5.22 (t, 1H, H3β), 5.08 (t, 1H, H4β), 4.99 (t, 1H, H2β), 5.08 - 5.04 (m, 2H, H1α, H4α), 4.8 (dd, 1H, H2α), 4.5 (d, 1H, H1β), 4.2 (m, 2H, H6), 4.1 (m, 2H, H6'), 4.03 (m, 1H, H5α), 3.8 (m, 1H, C*H*$_2$-CH_2-CH_2β), 3.7 (m, 1H, H5β), 3.66 (C*H*$_2$-CH_2-CH_2α), 3.6 (m, 18H, 6×OC*H*$_3$), 3.46 (m, 4H, C*H*$_2$-CH_2-CH_2β), 3.41 (m, 4H, C*H*$_2$-CH_2-CH_2α), 2.09, 2.07, 2.03, 2.01 (each s, 24H, 8×OAc), 1.7 (m, 4H, CH_2-C*H*$_2$-CH_2), 0.6 (m, 4H, CH_2-CH_2-C*H*$_2$). ^{13}C NMR (500 MHz, $CDCl_3$): δ = 170.9 - 169.5 (4×O*C*OCH_3), 101.0 (C1β), 95.9 (C1α), 73.0 (C3β), 72.2 (*C*H_2-CH_2-CH_2β), 71.9 (C5β), 71.5 (C2β), 71.1 (C2α), 70.8 (*C*H_2-CH_2-CH_2α), 70.4 (C3α), 68.8 (C4α), 68.6 (C4β), 67.4 (C5α), 62.1 (C6β), 61.7 (C6α), 50.7 (6×O*C*H_3), 22.9 (CH_2-*C*H_2-CH_2α,β), 22.8 (8×OCO*C*H_3), 5.5 (CH_2-CH_2-*C*H_2α), 5.2 (CH_2-CH_2-*C*H_2β).

Preparation and modification of silica nanoparticles

Silica nanoparticles were prepared by a previously reported method.[20] 118 mL of ethanol, 2.5 mL of aqueous ammonium hydroxide solution, and 2.0 mL of TEOS were mixed and stirred for 12 h room temperature in a 250 mL one-neck flask. The mixture was centrifuged for 30 min at 15000 rpm. The precipitate was redispersed in ethanol, followed by centrifugation. This centrifugation-redispersion procedure was repeated more than three times. Further the mixture was centrifuged at 3800 rpm for 10 min, and the supernatant containing silica nanoparticles was collected into a two-neck flask. TSPAG (2) was dissolved in anhydrous ethanol and added to the mixture through a cannula. The mixture was refluxed with vigorous stirring in N_2

atmosphere for 2 days. After cooling, the dispersion of the modified silica was purified by centrifugation with dichloromethane (for 30 min at 15000 rpm, 4 times) to remove the excess compound 2. Then, the dispersed solution was centrifuged at 3800 rpm for 10 min to remove any particle aggregates, and the supernatant containing the modified silica nanoparticles was obtained.

Preparation of SiO_2-TAC nanocomposites

0.2 g of TAC flakes were dissolved overnight in dichloromethane by sonication. The dispersion containing the modified silica nanoparticles was added to the TAC solution and stirred vigorously at room temperature for a day. Four different samples with 5, 10, 20, and 40 wt% of SiO_2-TAC nanocomposite dispersions were prepared by varying the quantities of modified silica nanoparticles. To fabricate the SiO_2-TAC nanocomposite films, the SiO_2-TAC nanocomposite dispersions were poured into glass dishes and gradually evaporate the solvent at room temperature. The SiO_2-TAC nanocomposite films were obtained by peeling them off from the glass substrates.

Characterization

Fourier-transform infrared (FT-IR) spectra were recorded using a JASCO FT/IR-600 Plus spectrometer for wavelengths ranging from 400 to 4000 cm^{-1} to study the surface of silica nanoparticles. ^{1}H and ^{13}C NMR spectra were measured using a Varian NMR System 500MHz NMR spectrometer. Data were reported as follows; chemical shifts in ppm from tetramethylsilane as an internal standard in $CDCl_3$, integration, and multiplicity (s = singlet, d = doublet, t = triplet, dd = doublet-doublet, m = multiplet). Transmission

electron microscopy (TEM) images were acquired using a Hitachi-7600 TEM instrument operated at 100 kV. Nanocomposite films were microtomed in a MODEL MT-X Ultramicrotome with CR-X, Boeckeler Instruments, Inc.

Thermal gravimetric analysis (TGA) measurements were performed on TGA Q-5000 IR (TA Instruments Inc.). TGA was performed by heating the samples from 30°C to 600°C at a heating rate of 10°C/min under N_2 atmosphere. Differential scanning calorimetry (DSC) measurements were carried out using a DSC-Q1000 (TA Instruments Inc.). The samples were dried at 80°C for 12 hr. Further, the samples were cooled to -10°C and then heated to 310°C at 10°C/min; the cooling/heating cycle between -10°C and 310°C was repeated at a rate of 10°C/min. Transmittance was measured using a UV-visible spectrometer (Sinco, S-3100).

2.4 Results and Discussion

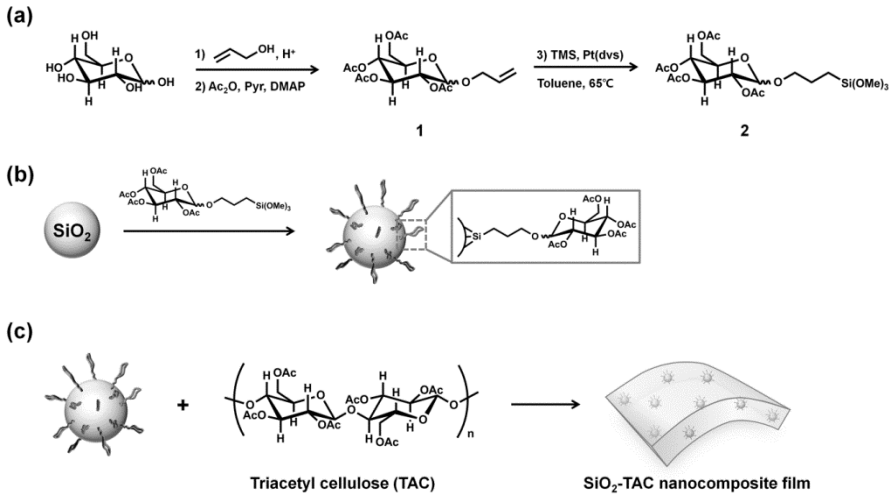

Scheme 2.1. (a) Synthesis of (trimethoxysilyl) propyl-2,3,4,6-tetra-O-acetyl-D-glucopyranoside, TSPAG (2), (b) Surface modification of silica nanoparticle with TSPAG to introduce (2,3,4,6-Tetra-O-acetyl-D-glucopyranoside) propyl moiety on the surface, and (c) fabrication of SiO_2-TAC nanocomposite film.

Silica particles having a diameter of 33 ± 4 nm and with a good size distribution were prepared, and they were well dispersed in water without exhibiting any aggregation; the dispersion is shown in Figure 2.1a. Since TAC is hydrophobic and silica nanoparticles are hydrophilic, surface modification was performed on the silica nanoparticles such that they were compatible (well-mixable) with the TAC matrix. The newly synthesized ligand (TSPAG, 2) with a structure similar to that of the repeating units of TAC, was attached to the surface of the silica nanoparticles by heating TSPAG and silica nanoparticles in ethanol; this is illustrated in Scheme 2.1. After attaching

TSPAG, the surfaces of the silica nanoparticles were observed using TEM. Predictably, there were no significant changes in their shape or size (32 ± 4 nm) because the actual size of TSPAG moiety is very small as compared to the size of the silica nanoparticles (Figure 2.1).

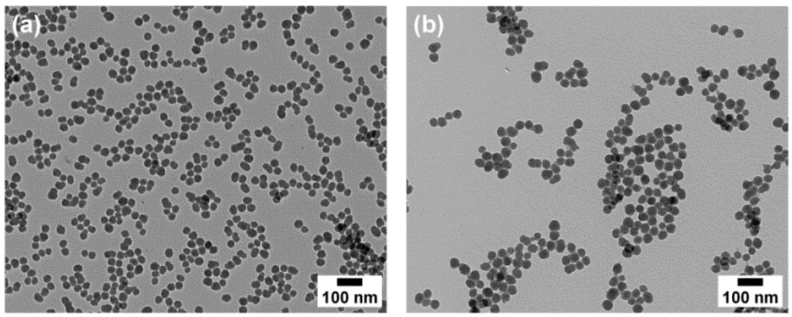

Figure 2.1. TEM images of (a) bare silica particles and (b) TSPAG modified silica nanoparticles.

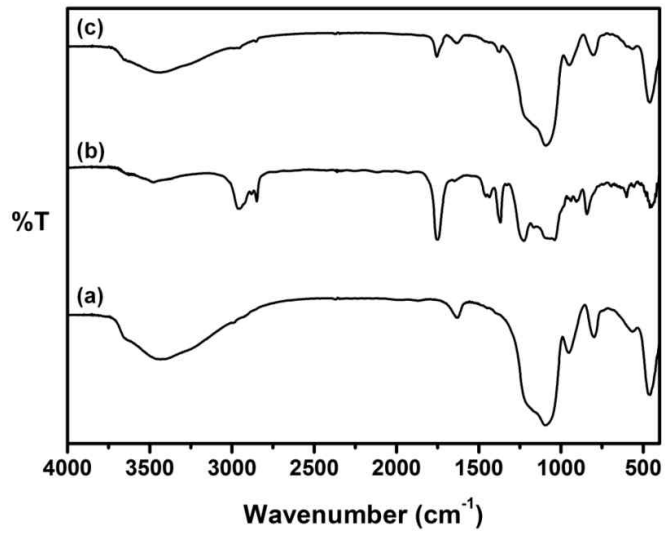

Figure 2.2. FT-IR spectra of (a) bare silica nanoparticles, (b) (trimethoxysilyl)propyl-2,3,4,6-tetra-O-acetyl-D-glucopyranoside (TSPAG), and (c) TSPAG-modified silica nanoparticles.

FT-IR and TGA data confirmed surface modification along with a change in the dispersibility of silica nanoparticles. Figure 2.2 shows FT-IR spectra of unmodified silica nanoparticles (Figure 2.2a), TSPAG (Figure 2.2b) and TSPAG-modified silica nanoparticles (Figure 2.2c). From the FT-IR spectrum of TSPAG-modified silica nanoparticles, Figure 2.2c, characteristic peaks from the organic ligand (Figure 2.2b) can be clearly seen at around 2950 and 1670 cm^{-1}. TGA curves of unmodified and TSPAG-modified silica nanoparticles are shown in Figures 2.3a and 2.3b, indicating weight losses of 13% and 18%, respectively, for the temperatures ranging from 30°C to 600°C. An additional 5% weight loss seen in TSPAG-modified silica nanoparticles can possibly be attributed to the thermal degradation of organic groups on the surface.

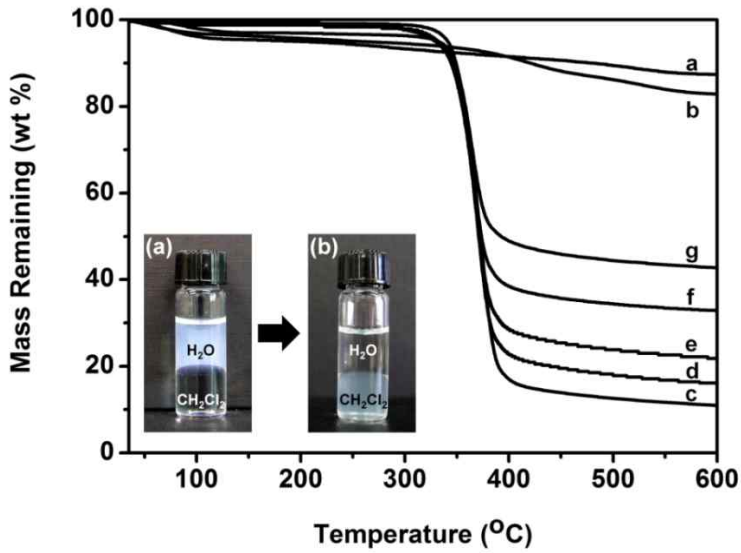

Figure 2.3. TGA of (a) bare silica nanoparticles, (b) TSPAG modified silica nanoparticles, (c) neat TAC film , SiO_2-TAC nanocomposites with (d) 5 wt% SiO_2, (e) 10 wt% SiO_2, (f) 20 wt% SiO_2, and (g) 40wt% SiO_2; inset photographs of (a) before and (b) after surface modification.

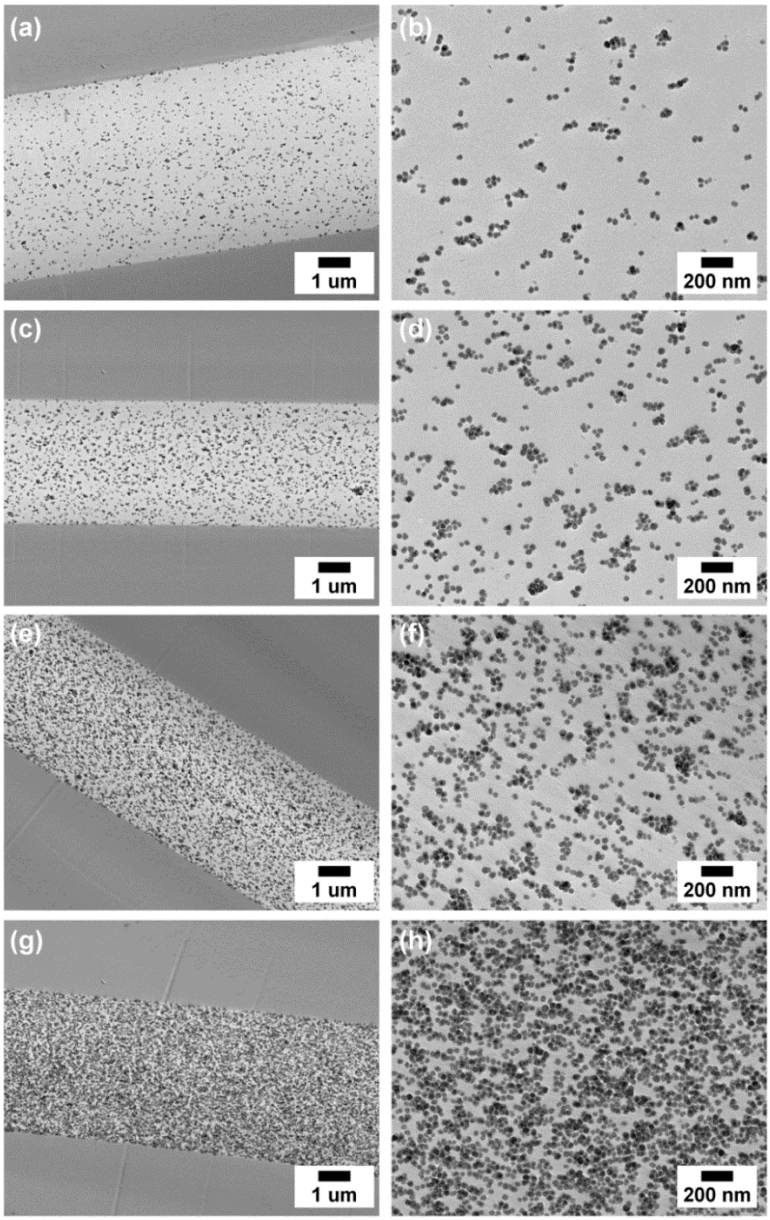

Figure 2.4. Cross-sectional TEM images of SiO_2-TAC nanocomposite films: (a, b) 5 wt% SiO_2, (c, d) 10 wt% SiO_2, (e, f) 20 wt% SiO_2 and (g, h) 40 wt % SiO_2. (a), (c), (e), and (g) are in low magnification; (b), (d), (f), and (h) are in high magnification.

Since TAC is very soluble in dichloromethane, the modified silica nanoparticles must be dispersed in dichloromethane in order to fabricate homogeneously incorporated SiO_2-TAC nanocomposites. As shown in the inset of Figure 2.3, the modified silica nanoparticles were well-dispersed in dichloromethane while the unmodified silica particles were dispersed in water. The dispersion containing the modified silica nanoparticles was very stable over a month; aggregation was not observed in this period. However, the boiling point of dichloromethane is not sufficiently high enough to produce good quality films by the spin-coating method. SiO_2-TAC nanocomposite films were prepared by solvent-casting method: gradually evaporating the solvent from solution containing TAC and modified silica nanoparticles. Figure 2.4 shows TEM images of SiO_2-TAC nanocomposite films of varying compositions by weight. The thickness of the films and the distribution of silica nanoparticles in them were determined from TEM images of cross-sectioned samples, cut using a microtome. The thickness of solution-cast films ranged from 4 to 6 μm, and the nanoparticles were homogeneously dispersed throughout the TAC matrices. The number of silica nanoparticles in the composite films was directly proportional to the wt% of silica nanoparticles. As expected, the TSPAG moieties, whose chemical structure is similar to that of TAC, on the surface of the silica nanoparticles lead to an increase in the interaction between polymer chains and the silica nanoparticles. This increased interaction allows a greater number of silica nanoparticles to be homogeneously dispersed in the TAC matrix, without generating microphase aggregates.

TGA was performed on neat TAC and SiO_2-TAC nanocomposite samples of four different proportions of silica nanoparticles (5, 10, 20, and 40 wt%) to determine their thermal properties (Figure 2.3). In all the samples, there was

almost no weight loss up to around 330°C; most started decomposing at around 400°C, and gradually decomposed further at higher temperatures. Higher residual weight (%) was observed in samples containing a greater number of silica nanoparticles. This is because silica nanoparticles are stable at these temperatures.

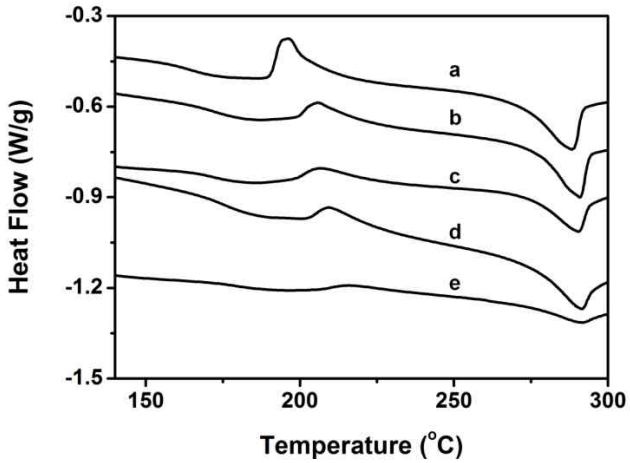

Figure 2.5. DSC traces of (a) neat TAC, SiO_2-TAC nanocomposites with (b) 5 wt% SiO_2, (c) 10 wt% SiO_2, (d) 20wt% SiO_2, and (e) 40 wt% SiO_2.

Table 2-1. DSC data of TAC and SiO_2-TAC nanocomposite films

	TAC	**5 wt% SiO_2**	**10 wt% SiO_2**	**20 wt% SiO_2**	**40 wt% SiO_2**
T_g (℃)	165	173	173	178	181
T_c (℃)	191	206	207	210	216
T_m (℃)	288	291	290	291	291
ΔT ($=T_m-T_c$)	98	85	84	82	75
ΔH_c (J/g)	12	6	5	4	2
ΔH_m (J/g)	20	13	9	13	6

The dispersion of silica nanoparticles in TAC leads to a change in its glass transition temperature, T_g. T_g of SiO_2-TAC nanocomposites gradually increased from that of pure TAC film (Figure 2.5 and Table 2.1). Interactions between nanoparticles and polymer chains, which disturb polymer chain mobility, could possibly have led to an increase in T_g[21]. An increase in the silica content in the TAC matrices lead to an increase in the crystallization temperature (T_c) and a proportional decrease in its heat capacity (ΔH_c). These results indicate that silica nanoparticles could improve crystallization of TAC matrices. The degrees of super-cooling, $\Delta T = (T_m - T_c)$, of nanocomposites were smaller than that of neat TAC, and gradually decreased as the nanoparticle content was increased. These results imply that the addition of silica nanoparticles into a TAC matrix can affect its rate of crystallization. This is consistent with the findings of a previous study, which states that silica nanoparticles lead to easier crystallization of the polymer due to the nucleation effect.[22] However, as shown in Figure 2.5 and Table 1, the difference in melting temperatures (T_m) of neat TAC and SiO_2-TAC nanocomposites is very small, and they are almost equal at about 3 °C, irrespective of the silica nanoparticle content. Since the melting temperatures of all the composite samples are almost equal, there appears to be no significant change in crystal size of the TAC.[23]

To investigate any migration of the modified silica within the polymer matrix at high temperatures, SiO_2-TAC nanocomposite film with a 10 wt% of silica was annealed at 210°C for 12 h. Post annealing, there was no significant change in morphology, as observed by cross-sectional TEM (Figure 2.6), confirming the excellent compatibility of surface-modified silica nanoparticles with the TAC matrix, and the thermal stability of nanocomposite

films.

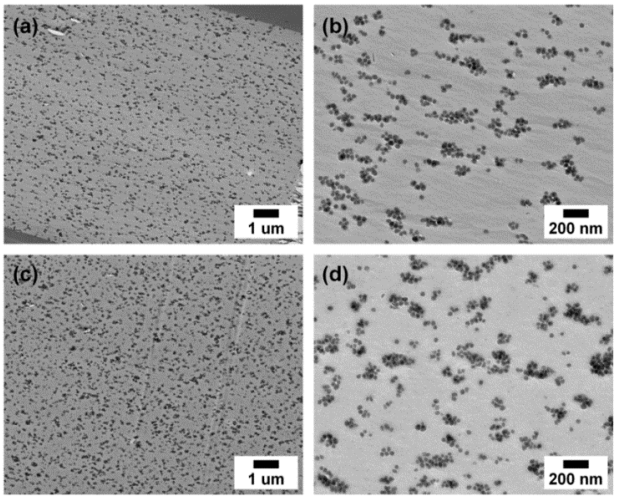

Figure 2.6. Cross-sectional TEM images of SiO_2-TAC nanocomposite films with 10 wt% SiO_2: (a, b) before and (c, d) after anealing at 210℃ for 12 h.

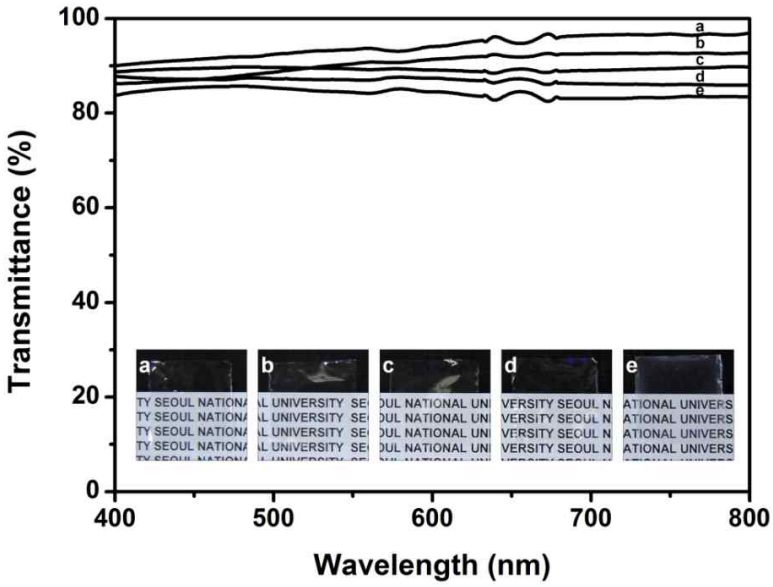

Figure 2.7. Transmittance spectra of (a) neat TAC, SiO_2-TAC nanocomposites with (b) 5wt% SiO_2, (c) 10 wt% SiO_2, (d) 20 wt% SiO_2, and (e) 40 wt% SiO_2. Inset: digital photographs of nanocomposite films.

The transparency of SiO_2-TAC nanocomposite films, which is another important property, was monitored by a UV-visible spectrometer (Figure 2.7) In the visible region, transparency of neat TAC was 80~93%, and the transparencies of the composite films were also in the same regions (See digital photos in Figure 2.7). Although transparency decreased gradually with an increase in silica contents, the composite film having 40 wt% of silica nanoparticles has a transparency of over 80% in the range from 400 nm to 800 nm, also confirming that the level of aggregation of silica nanoparticles was not significant to induce scattering of light in visible region.

2.5. Conclusion

The surfaces of 33 nm sized silica particles were successfully modified, by attaching a TSPAG, TAC monomer moiety, in order to increase the interaction between the silica nanoparticles and the TAC matrix. As expected, the modified silica nanoparticles were homogeneously dispersed in TAC matrices up to compositions of 40wt% of the nanoparticles. The results from the thermal analysis show that SiO_2-TAC nanocomposites have higher T_g and T_c values as compared to neat TAC. The difference in values of T_g and T_c is a function of the silica content. The transparency of all the nanocomposite films was over 80% in the visible range, confirming the excellent compatibility of nanoparticles with the TAC matrix, without any microphase aggregation.

Acknowledgements

I would like to thank Seung-Min Jeon and Prof. Byeong-Hyeok Sohn for preparing cross-sectional TEM samples by microtoming.

2.6. References

[1] Paul, D. R.; Robeson, L. M., *Polymer* **2008,** *49*, 3187-3204.

[2] Coleman, J. N.; Khan, U.; Gun'ko, Y. K., *Adv. Mater.* **2006,** *18*, 689-706.

[3] Holder, E.; Tesslerb, N.; Rogach, A. L., *J. Mater. Chem.* **2008,** *18*, 1064-1078.

[4] Zou, H.; Wu, S.; Shen, J., *Chem. Rev.* **2008,** *108*, 3893-3957.

[5] Sih, B. C.; Wolf, M. O., *Chem. Commun.* **2005**, 3375-3384.

[6] Schmid, A.; Tonnar, J.; Armes, S. P., *Adv. Mater.* **2008,** *20*, 3331-3336.

[7] Ciprari, D.; Jacob, K.; Tannenbaum, R., *Macromolecules* **2006,** *39*, 6565-6573.

[8] Chinthamanipeta, P. S.; Kobukata, S.; Nakata, H.; Shipp, D. A., *Polymer* **2008,** *49*, 5636-5642.

[9] Yao, X.; Tian, X.; Xie, D.; Zhang, X.; Zheng, K.; Xu, J.; Zhang, G.; Cui, P., *Polymer* **2009,** *50*, 1251-1256.

[10] Guo, Y.; Wang, M.; Zhang, H.; Liu, G.; Zhang, L.; Qu, X., *J. Appl. Polym. Sci.* **2008,** *107*, 2671-2680.

[11] Li, X.; Cao, Z.; Zhang, Z.; Dang, H., *Appl. Surf. Sci.* **2006,** *252*, 7856-7861.

[12] Lebret, V.; Raehm, L.; Durand, J. O.; Smaihi, M.; Werts, M. H. V.; Blanchard-Desce, M.; Methy-Gonnod, D.; Dubernet, C., *J. Sol-Gel Sci. Techn.* **2008,** *48*, 32-39.

[13] Sata, H.; Murayama, M.; Shimamoto, S., *Macromol. Symp.* **2004,** *208*, 323-333.

[14] Novak, B. M., *Adv. Mater.* **1993,** *5*, 422-433.

[15] Khrenov, V.; Klapper, M.; Koch, M.; Mullen, K., *Macromol. Chem. Phys.* **2005,** *206*, 95-101.

[16] Lu, C.; Chen, X.; Xie, Z.; Lu, T.; Wang, X.; Ma, J.; Jing, X.,

Biomacromolecules **2006,** *7*, 1806-1810.

[17] Wolfenden, M. L.; Cloninger, M. J., *J. Am. Chem. Soc.* **2005,** *127*, 12168-12169.

[18] Behr, A.; Naendrup, F.; Obst, D., *Adv. Synth. Catal.* **2002,** *344*, 1142-1145.

[19] Sabourault, N.; Mignani, G.; Wagner, A.; Mioskowski, C., *Org. Lett.* **2002,** *4*, 2117-2119.

[20] Ha, S.-W.; Camalier, C. E.; Jr., G. R. B.; Lee, J.-K., *Chem. Commun.* **2009**, 2881-2883.

[21] Al-Kandary, S.; Ali, A. A. M.; Ahmad, Z., *J. Appl. Polym. Sci.* **2005,** *98*, 2521-2531.

[22] Rong, M. Z.; Zhang, M. Q.; Zheng, Y. X.; Zeng, H. M.; Walter, R.; Friedrich, K., *Polymer* **2001,** *42*, 167-183.

[23] Lu, H.; Xu, X.; Li, X.; Zhang, Z., *Bull. Mater. Sci.* **2006,** *29*, 485-490.

Chapter 3.

Polyimide nanocomposites with functionalized SiO_2 nanoparticles: Enhanced processability, thermal and mechanical properties

3.1 Abstract

SiO_2-polyimide nanocomposites were successfully fabricated by surface modification of silica nanoparticles. In order to create structural similarity between the polymer and the SiO_2 surface and to generate interfacial interaction with the polymer chain, (3-trimethoxysilylpropyl) diethylenetriamine was attached to the surface, and then, the surface amines were reacted with phthalic anhydride. The modified silica nanoparticles in polyamic acid solution were subjected to thermal imidization to obtain SiO_2-polyimide (PI) nanocomposite films. Cross-sectional transmission electron microscopy results showed no significant aggregation in any of the SiO_2-PI nanocomposite films having up to 20 wt% of silica nanoparticles. The effects of silica nanoparticles as a filler material on the thermal, optical, and mechanical properties of the SiO_2-PI nanocomposite films were studied in comparison with those of PI by UV-Vis spectrometery, thermal gravimetric analysis, thermal mechanical analysis, and nanoindentation

3.2 Introduction

Aromatic polyimides are important industrial polymers used in many applications such as packaging and insulation for large-scale integrated circuits because of their high thermal stability, high chemical resistance, mechanical properties, and low dielectric constants.[1-2] However, their disadvantages include high glass transition temperatures (T_g)[3-4] and high thermal expansion coefficients (CTE).[1] The high T_g of polyimides, which is caused by their rigid back bones and strong interaction, makes them difficult to process.[3] In addition, the higher CTE of polyimides compared with that of metals causes interfacial stress induced by the thermal expansion mismatch between the polyimide and the metal during thermal cycling in the manufacturing process. This leads to device failure via interfacial decohesion or cracks in microelectronic applications.[5-6] Many efforts to reduce polymer CTE have been undertaken by using inorganic fillers such as nanoparticles,[7] nanotubes,[8] and clay.[9] SiO_2 nanoparticles are most widely used as a nanofillers due to their low CTE (~0.55 $\times 10^{-6}$ $^{\circ}C^{-1}$), high thermal stability, optical transparency, and easy surface modification.[10] There have been many attempts to fabricate SiO_2-polyimide nanocomposites in order to reduce the CTE of the polyimide. Most of the SiO_2-polyimide nanocomposites were prepared by the in situ sol-gel method[1, 11-14] using a silica precursor, while only a few of them were prepared by blending processes.[7, 15-16] Because polyimides and SiO_2 are incompatible, SiO_2 tends to accumulate in large aggregations in a polymer matrix.[15] To improve the compatibility between polyimide and SiO_2, surface modification of silica nanoparticles with oleic acid has been performed.[7, 16] However, no significant changes in thermal properties such as T_g and thermal decomposition temperature (T_d) were

observed. Therefore, to obtain the desired properties of polyimide nanocomposites without aggregation of silica nanoparticles, an appropriate surface ligand to be used for the modification of the nanoparticles is needed.

Herein, SiO_2-polyimide nanocomposites were fabricated by surface modification of SiO_2, using functional groups with chemical and structural similarities to the polymer chains. Silica nanoparticles prepared by the Stöber method[17] were modified by a simple two-step reaction: surface Si-OH groups were reacted with (3-trimethoxy-silylpropyl) diethylenetriamine (DETAS) to introduce a large number of amine sites onto the surface,[18] which could then react with phthalic anhydride, generating amic acid terminal groups (Scheme 3.1). We successfully incorporated silica nanoparticles up to 20 wt% in the polymers without aggregation, and compared the thermal, optical, and mechanical properties, along with the CTE, with those of the pristine polyimide to understand the effects of the silica nanoparticles.

3.3 Experimental Section

Poly(pyromellitic dianhydride-co-4,4′-oxydianiline) amic acid solution (12.8 wt% ± 0.5 wt% in 80% NMP, 20% aromatic hydrocarbon), *N*-methyl-2-pyrrolidone, triethyl amine, phthalic anhydride, and KBr were purchased from Aldrich. Ethanol was purchased from J. T. Baker, tetraethyl orthosilicate (TEOS) from TCI, and (3-trimethoxysilylpropyl) diethylenetriamine (DETAS) from Gelest. All organic solvents were used without any further purification.

Synthesis and modification of silica nanoparticles

2.5 mL of aqueous ammonium hydroxide solution and 2.5 mL of deionized water were mixed with 118 mL of EtOH. Then, 2.0 mL of TEOS was added and stirred for 12 h at room temperature. The silica suspension was centrifuged for 20 min at 20000 rpm. The precipitate was redispersed in EtOH, followed by centrifugation under the same conditions. This centrifugation-redispersion procedure was repeated more than two times. Further, the silica suspension was centrifuged at 3800 rpm for 10 min in order to remove any aggregated products, and the supernatant was collected for the next reaction.

4.0 mL of DETAS was added to the dispersed SiO_2 solution (400 mg of SiO_2 nanoparticles in 40 mL of EtOH), and the mixed solution was stirred at room temperature for 12 h. The mixture was centrifuged for 20 min at 20000 rpm, and then, the precipitate was redispered in EtOH. This centrifugation-redispersion procedure was repeated more than two times to obtain the dispersed solution of the DETAS-modified SiO_2 nanoparticles (DETAS-SiO_2). To the dispersed solution of DETAS-SiO_2 in 40 mL of EtOH, 1.7 g of phthalic anhydride and 0.16 mL of triethylamine were added. The mixture was refluxed with vigorous stirring for 12 h. After cooling, the dispersion was

centrifuged for 20 min at 20000 rpm, and then, the precipitate was redispered in N-methyl-2-pyrrolidone (NMP). This precedure was repeated more than two times to remove the excess phthalic anhydride and triethylamine. The dispersed solution was centrifuged at 3800 rpm for 10 min to remove any aggregated particles, and the dispersed solution of phthalic anhydride-modified silica nanoparticles (P-SiO_2) was reserved for the next process.

Preparation of SiO_2-polyimide nanocomposites

P-SiO_2 suspension (30 mg/mL in NMP) was added to appropriate amounts of poly(pyromellitic dianhydride-co-4,4′-oxydianiline) amic acid (PAA) solution to prepare the composite films containing 5, 10, and 20 wt% of SiO_2. And then NMP was added to each mixture to make the weight percent of PAA in each mixture in 8 wt%. The mixed solutions were stirred vigorously at room temperature for one day. To fabricate the SiO_2-polyimide nanocomposite films, the SiO_2-PAA nanocomposite dispersions were poured into glass dishes and degassed in vacuum. Then, the SiO_2-PAA nanocompsite dispersions were heated at 60 °C for 12 h, 100 °C for 1 h, 150 °C for 1 h, 200 °C for 1 h, 250 °C for 1 h, and finally at 350 °C for 1 h 30 min in a vacuum oven to carry out the imidization process as suggested in the literature.[19] The stepwise curing is conventional way to convert polyamic acid into polyimide. The imidization reaction started at around 100 °C and nearly completed at around 200 °C. However higher temperature are needed to completely remove the solvent and obtain fully imidized film.[20] It has been reported that imidization is completed at 350 °C and above.[21] The SiO_2-polyimide nanocomposite films were obtained by peeling them off from the glass substrates.

Characterization

To study the surfaces of the silica nanoparticles, Fourier-transform infrared (FT-IR) spectra were recorded using a NICOLET iS10 system. The dynamic light scattering (DLS) and the zeta potential of the particles in ethanol were measured using a zetameter (Zetasizer, Malvern instruments). ^{13}C CP-MAS NMR spectra were measured using a Bruker Avance 400MHz WB. Transmission electron microscopy (TEM) images were acquired using a Hitachi-7600 instrument operated at 100 kV. Nanocomposite films were microtomed in a model MT-X Ultramicrotome with CR-X, Boeckeler Instruments, Inc.

Thermal gravimetric analysis (TGA) measurements were performed using an SDT Q600 apparatus (TA Instruments Inc.). TGA was performed by pre-heating the sample at 100 °C for 60 min and then heating it from 100 °C to 1000 °C at a heating rate of 10 °C/min under N_2-atmosphere. Transmittance was measured using a UV-Vis spectrometer (Sinco, S-3100). Thermal mechanical analyses (TMA), using a TMA-Q400 system, were performed to measure the T_g and CTE of the nanocomposite films under the tension mode (load = 50 mN), by heating them from 25 °C to 400 °C at a heating rate of 5 °C/min under nitrogen.

Nanoindentation tests were performed on 50–60 mm-thick polyimide and SiO_2-PI nanocomposite films using an Ultra Nanoindentation Tester (UNHT, CSM instruments). The loading and unloading rates were both 250 mN/min. A holding time of 3 s was maintained at the maximum load. At least seven indentations were performed on each sample, and the average values were determined.

In an indentation test, hardness is defined as the indentation at the maximum load, P_{max}, divided by the projected area of tip-sample contact, A, and is calculated for a perfect Berkovich indenter as follows:

$$\mathrm{H} = \frac{P_{max}}{A}$$

$$A = 24.5{h_c}^2$$

Here the contact depth, h_c, can be determined by taking into account the response of the material's elastic deflection, h_d:

$$h_c = h_{max} - h_d$$

$$h_c = \varepsilon \frac{P_{max}}{S}$$

where h_{max} and S are the maximum indentation depth and initial unloading stiffness, respectively, and ε is a geometrical constant (0.75 for a Berkovich indenter). The contact stiffness of the sample, S, is given by the initial unloading slope.

The effective elastic modulus is formulated in terms of the unloading slope S and contact area A as

$$E_{eff} = \frac{\sqrt{\pi} \cdot S}{2 \cdot \beta \cdot \sqrt{A}}$$

For a Berkovich indenter, the indenter geometry parameter β is 1.034.

3.4 Results and Discussion

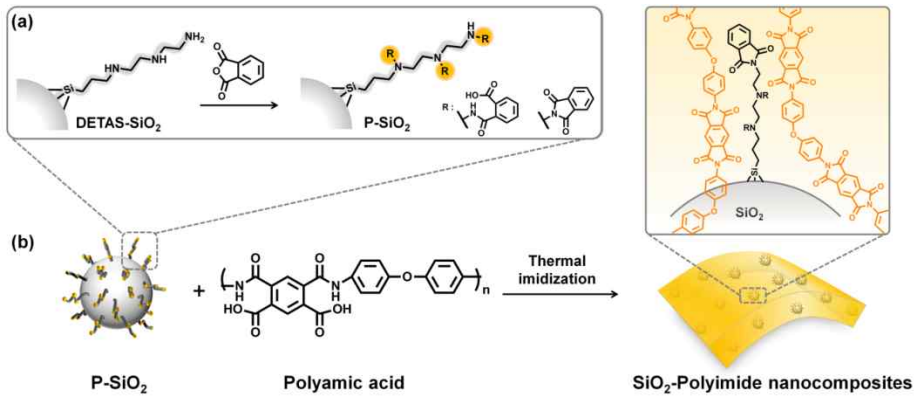

Scheme 3.1. Schematic illustrations of (a) the surface modification of silica nanoparticles by (3-trimethoxysilylpropyl) diethylenetriamine (DETAS) and the reaction between the suface amines and phthalic anhydride and (b) the fabrication of SiO_2-PI nanocomposite film by thermal imidization.

Figure 3.1a shows a TEM image of silica nanoparticles with diameters of 30±4 nm. And hydrodynamic size of SiO_2 measured by DLS is 46±1 nm (Figure 3.5a), which indicated that SiO_2 were well dispersed in ethanol without any aggregation. As shown in the Figure 3.2, unmodified SiO2 nanoparticles tend to generate the large aggregation within the polyimide matrix. Therefore, surface modification is needed to improve dispersability of SiO_2 in polyimide matrix. To introduce a ligand with a structure similar to the repeating units of polymer on the silica surface, a large number of amine groups were introduced on the silica surface by attaching DETAS to the surface of the SiO_2 nanoparticles to generate DETAS-SiO_2, and then, the amine groups of DETAS-SiO_2 were reacted with phthalic anhydride in EtOH (Scheme 3.1a), to form imide or amic acid groups *via* the phthalic anhydride-

ring opening reactions. As was expected, the amic acid moiety on the nanoparticle surfaces acted as a plasticizer by interacting with the polymer chains as reported that dimethyl phthalate could be used as plasticizers for polyimide to decrease T_g and T_d.[22]

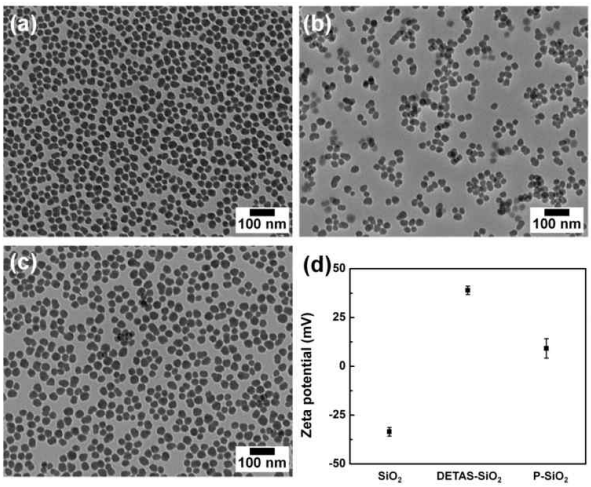

Figure 3.1. TEM images of (a) bare silica nanoparticles, (b) DETAS-SiO_2, and (c) P-SiO_2. (d) Zeta potential values of bare and modified silica nanoparticles in EtOH.

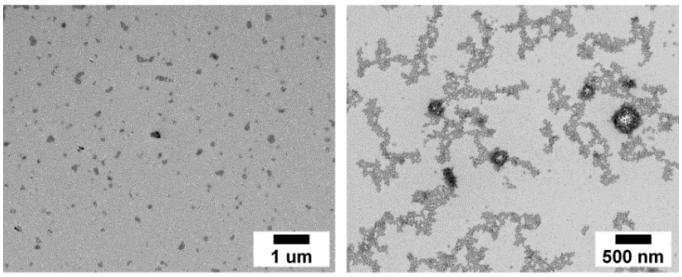

Figure 3.2. TEM images of bare SiO_2-PI nanocomposites. The TEM images were obtained by spin-coating SiO_2-PAA solution onto a TEM grid, followed by thermal imidization.

After the modification, the surfaces of the SiO_2 nanoparticles was characterized by FT-IR, solid-state ^{13}C-NMR, zeta-potentail, and TGA. A strong absorption band at 1710 cm^{-1}, which corresponded to a C=O stretching vibration from the amic acid moiety, was clearly observed in the FT-IR spectrum of the P-SiO_2 (Figure 3.3c). In addition, new peaks at 110–130 ppm and 160–170 ppm, corresponding to aromatic carbons and carbonyl carbon, respectively, were found in the solid-state ^{13}C-NMR spectrum of the P-SiO_2 (Figure 3.4b). As shown in Figure 3.1a–c, the nanoparticles were well dispersed in the solvents (EtOH and NMP) without showing any significant changes in size or shape during the surface modification reactions. Furthermore, the surface charge of the bare SiO_2 generated a negative zeta potential of -33.6 mV due to a hydroxyl group, as shown in Figure 3.1d. After attaching DETAS, however, the zeta potential changed from -33.6 mV to 38.9 mV, which is attributed to positively charged amine groups in the DETAS on the silica surface, even neutral conditions. The zeta-potential of the P-SiO_2 was 9.1 mV since most of the amine groups of the DETAS formed neutral imide linkages with phtalic anhydride and some amic acid units had zwitter-ion-type charges.

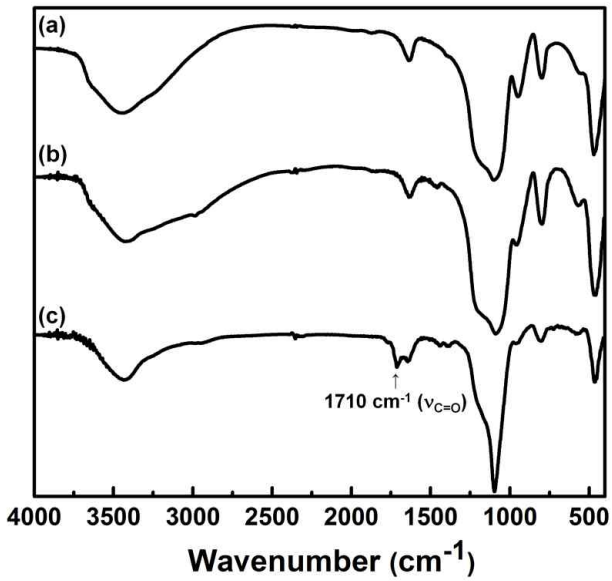

Figure 3.3. FT-IR spectra of (a) unmodified silica nanoparticles, (b) DETAS-SiO_2, and (c) P-SiO_2.

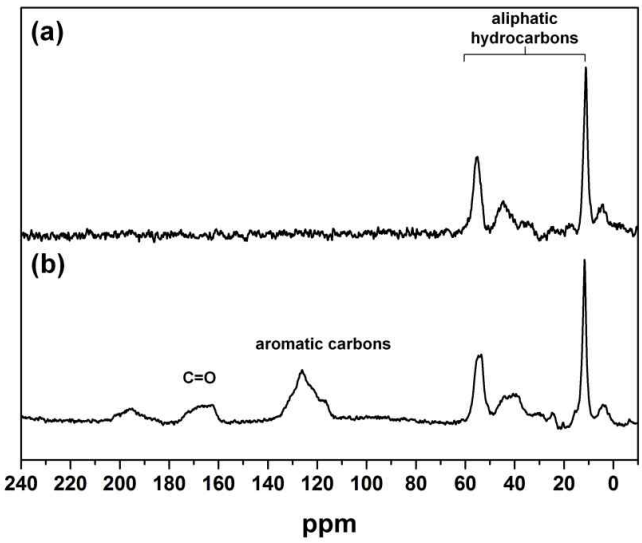

Figure 3.4. Solid ^{13}C CP/MAS NMR spectra of (a) DETAS-SiO_2 and (b) P-SiO_2.

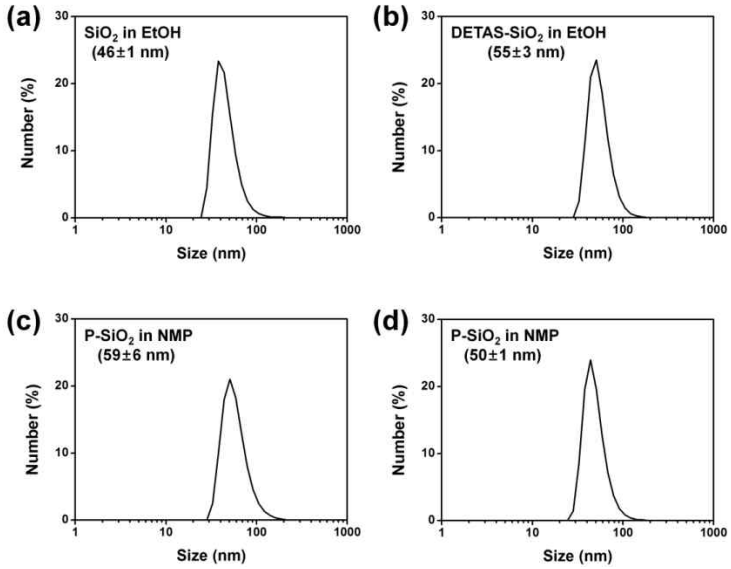

Figure 3.5. Size distributions of (a) SiO_2 in EtOH, (b) DETAS-SiO_2 in EtOH, (c) as-prepared P-SiO_2 in NMP, and (d) P-SiO_2 in NMP after being stored for one year.

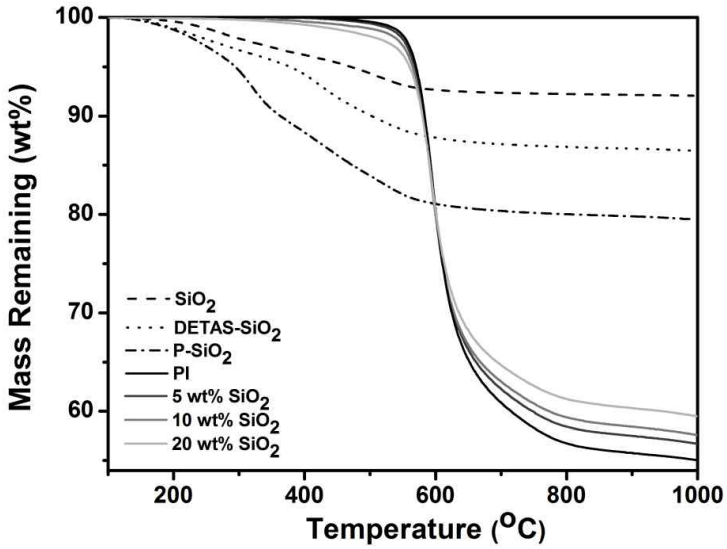

Figure 3.6. TGA curves for bare silica, modified silica nanoparticles (DETAS-SiO_2 and P-SiO_2), neat polyimide film, and SiO_2-polyimide nanocomposite films with various SiO_2 contents.

TGA curves for bare SiO_2, DETAS-SiO_2, and P-SiO_2 are shown in Figure 3.6. The amount of weight loss gradually increased in the temperature range from 100 to 1000 °C. An additional 5.6 % and 12.6 % weight loss resulted from the attached organic units on the surfaces of the SiO_2 nanoparticles after the surface modification. The mole percentage of organic groups on the surface of SiO_2 nanoparticles could be calculated from TGA data as summarized in Table 3.1.

Table 3.1. Calculated molar ratio of organic groups on SiO_2 nanoparticles by TGA.

	Weight percent (wt%)	**Molecular weight (g/mol)**	**Relative amount from 100 g Sample (mol)**	**Mole percent of organic groups (mol%)**
SiO_2	87.4	60 (for fully condensed SiO_2)	1.5	
DETAS on the DETAS-SiO_2	5.6	265.43 (for DETAS)	2.1×10^{-2}	1.4
Phthalic anhydride on the P-SiO_2	7	148.12 (for phtalic anhydride)	4.7×10^{-2}	3.1

Since polyamic acid was dissolved in and is usually processed in NMP, the P-SiO_2 was dispersed in the NMP in order to homogeneously incorporate the SiO_2 nanoparticles in the polyamic acid. As shown in Figure 3.1c and Figure 3.5c, the P-SiO_2 nanoparicles were well dispersed in NMP without generating aggregation. Furthermore, the dispersed P-SiO_2 solution in NMP showed the excellent long-term stability over the one year (Figure 3.5d). Three different

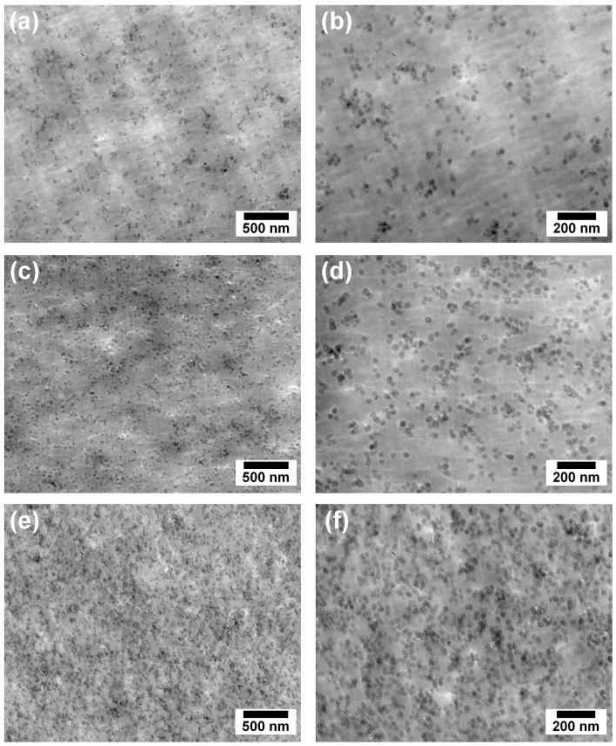

Figure 3.7. Cross-sectional TEM images of SiO_2-PI nanocomposite films: (a, b) 5, (c, d) 10, and (e, f) 20 wt% of SiO_2. (a), (c) and (e) are under low magnification; (b), (d) and (f) are under high magnification.

SiO_2-polyamic acid nanocomposite solutions (5, 10, 20 wt% of SiO_2) were prepared by mixing the appropriate amounts of polyamic acid solution with the P-SiO_2 nanoparticles dispersed in the NMP solution. The SiO_2-polyimide nanocomposite films were produced using the thermal imidization method, by gradually heating the SiO_2-polyamic acid nanocomposite solution up to 350 °C, as described in the experimental section. Figure 3.7 shows cross-sectional TEM images of SiO_2-PI nanocomposite films. It was clearly observed that the silica nanoparticles were homogeneously dispered in the polyimide matrices

without showing signs of aggregation. This indicates that the ligands on the SiO_2 surface have similar chemical structures to the repeating units of the polyimide, and thus, the compatibility between the polymer chain and the nanoparticles is enhanced. As a result, aggregations were not observed in any of the SiO_2-polyimide nanocomposite films having up to 20 wt% of SiO_2 nanoparticles.

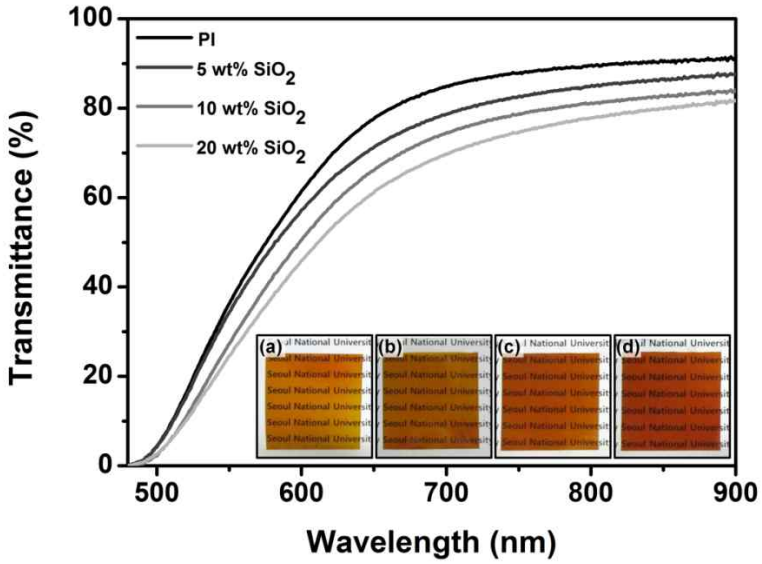

Figure 3.8. Transmittance spectra of neat PI film and SiO_2-PI nanocomposite films with various SiO_2 contents. Inset: digital photographs of nanocomposite films clearly showing the transparency; (a) neat PI film, SiO_2-PI nanocomposite films with (b) 5, (c) 10, and (d) 20 wt% of SiO_2.

Transparency of SiO_2-PI nanocomposite films, which can be measured using a UV-Vis spectrometer, is another important property for optical applicaions.

Stong absorption in the UV- vis region from all of the samples is attributed to an intrinsic feature of polyimides (Figure 3.8), which exhibit charge transfer interactions between electron donor and acceptor[2] even though the thickness of the PI films ranged from 50 μm to 60 μm. Although the transparency gradually decreased with increasing silica content, no serious degradation in transparency was found in any of the samples. This result also indicates that the silica nanoparticles are homogeneously dispersed in the polyimide matrices; thus, scattering of light in the visible region is negligible.

Table 3.2. Thermal and mechanical properties of PI and SiO_2-PI nanocomposite films

	T_d (°C)[a]	T_g (°C)[b]	CTE (10^{-6}/°C)[c]	Hardness (MPa)	Modulus (GPa)
Polyimide	570.1	381.3	33.9	215.4±2.5	3.20±0.03
5 wt% SiO_2-PI	567.7	379.1	30.8	229.7±1.6	3.48±0.04
10 wt% SiO_2-PI	564.7	376.3	30.6	249.9±2.8	3.50±0.05
20 wt% SiO_2-PI	560.3	363.3	27.8	283.9±4.3	3.71±0.05

[a] Temperature at which 5 % weight loss was recorded by TGA; [b] T_g determined by TMA; [c] CTE was determined over a range of 100–250 °C.

T_g values of the PI and SiO_2-PI nanocomposite films were determined by TMA, and the results are listed in Table 3.2; the T_g values of the nanocomposites gradually declined as the silica content increased. Because of

the large surface area of the nanoparticles, the interface between the polymer and the nanoparticle can change and affect the thermal properties of the nanocomposites.[23] We assume that ligands on the nanoparticle surfaces acted as plasticizers for the polyimide. As a result, the chain kinetics of the polymer are changed at the polyimide-nanoparticle interface regions,[24] and thus, T_g decreases from 381.3 to 363.3 °C as the SiO_2 content increases. This result indicates that SiO_2-polyimide nanocomposites have better processability due to the plasticizing effect of the P-SiO_2 surface ligands.

TGA curves for the SiO_2-PI nanocomposite films with various silica contents are also shown in Figure 3.6. For all of the samples, almost no weight loss was found up to around 300 °C, and then, the films gradually decomposed at higher temperatures. The T_d values of the nanocomposites, which were determined as the temperatures at which 5 % weight loss occured on the TGA curves, are summarized in Table 3.2. Although the T_d values decreased slightly with inceasing silica content, T_d for each of the nanocomposites was higher than 500 °C, indicating good thermal stability for practical applications. The decreasing T_d values with increasing silica content can be explained by the same reasoning as for the decreasing of T_g values. As expected, the remaining weight (wt%) at 1000 °C was proportional to the amount of silica nanoparticles in each of the polyimide films.

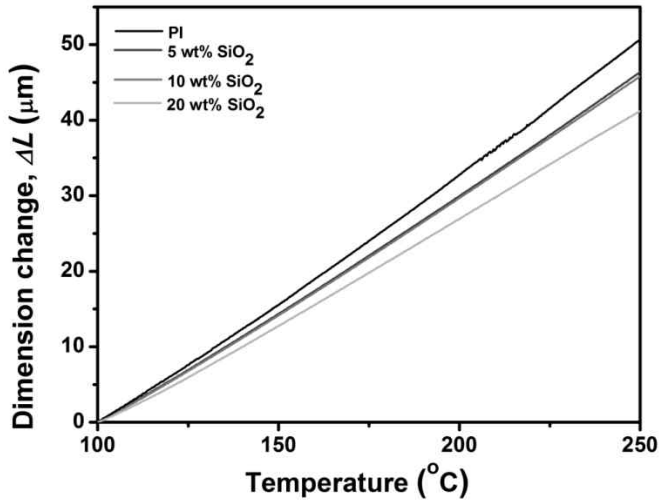

Figure 3.9. Thermal expansion of neat PI film and SiO_2-PI nanocomposite films with various SiO_2 contents.

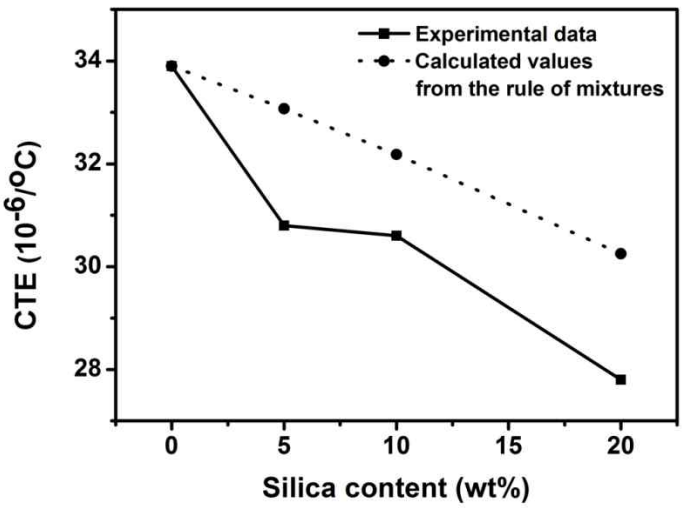

Figure 3.10. CTE values for neat PI and SiO_2-PI nanocomposite films

Table 3.3. The experimental and calculated value of coefficients of thermal expansion of polyimide and SiO_2-polyimide nanocomposites

wt. %	vol. %	Experimental value (10^{-6}/°C)	Calculated value (10^{-6}/°C)
Neat PI	-	33.9	-
5	2.2	30.8	33.1
10	4.6	30.6	32.2
20	9.8	27.8	30.2

To quantify the effect of the SiO_2 nanoparticles on the thermal expansion of the PI nanocomposites, TMAs were performed. Figure 3.9 shows the thermal expansion curves for the PI and nanocomposite films in the temperature range from 100 to 250 °C. The coefficient of thermal expansions, α, for the nanocomposite films, which were calculated based on the thermal expansion curves by following equation, are shown in Table 3.2.

$$\alpha = \frac{1}{L_0}\frac{\Delta L}{\Delta T}$$

Where L_0 is the initial length of sample and ΔL is the length change at a given temperature difference (ΔT). As expected, reductions in the CTE are observed with the incorporation of silica nanoparticles into the PI matrix. The CTEs for neat PI and nanocomposites with 5, 10, and 20 wt% SiO_2 were 33.9, 30.8, 30.6 and 27.8 $°C^{-1}$, repectively, as shown in Figure 3.10. SiO_2 has a relatively low CTE (~0.55×10^{-6} $°C^{-1}$) in comparison with PI (33.9×10^{-6} $°C^{-1}$), resulting in reductions of the thermal expansion of the nanocomposites as the

SiO_2 content increases. In order to predict the theoretical CTE values of the nanocomposites, the CTE of each nanocomposite was calculated by the simplest rule of mixtures model,[25] assuming that there is no interfacial interaction between the polymer and the nanoparticles. The mathematical equation is described as follows:

$$\alpha_c = \alpha_f \phi_f + \alpha_m \phi_m$$

where the subscripts c, *m, f* represent nanocomposites, polymer, and filler phase, respectively. α and ϕ are coefficient of thermal expansion and the volume fraction of the constituents. The coefficient of thermal expansion for polyimide and SiO_2 are 33.9 and 0.55 (10^{-6}/°C), respectively. These calculated values are shown along with the experimental data in Table 3.3 and Figure 3.10; significant differences between the two sets of data are apparent confirming the important interfacial interaction between the, polymer and the surface-modified SiO_2 nanoparticles.

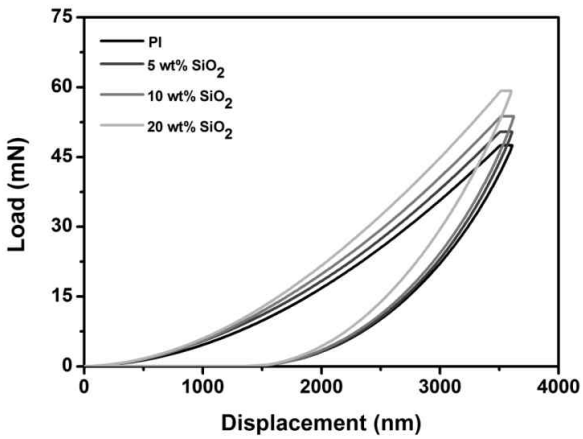

Figure 3.11. Load *vs.* indenter displacement for neat PI film and SiO_2-PI nanocomposite films with different SiO_2 contents

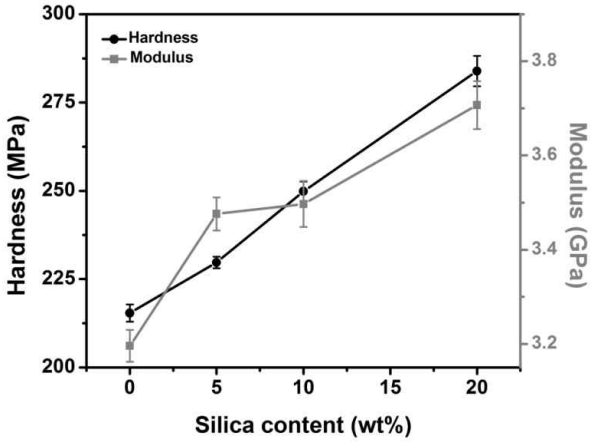

Figure 3.12. Hardness and effective elastic modulus values for neat PI and SiO_2-PI nanocomposite films with different SiO_2 contents.

Nanoindentation tests were performed to investigate the effect of nanoparticle reinforcement on the nanocomposite's mechanical properties. Figure 3.11 shows load-displacement curves for neat PI and the nanocomposites with various silica contents. The similarities among the curves indicates that the nanocomposites are based on polyimide matrices. The curves gradually shift upwards and the maximum penetration depth decreases as the silica content in the PI matrices increases, since silica nanoparticles lead to nanocomposites with high resistance to plastic deformation.[26-27] The elastic displacement is recovered during unloading. The initial unloading slopes (stiffness, *S*) increase with silica content, and thus, the effective elastic moduli are enhanced. The average hardness *H* and effective elastic modulus E_{eff} values are calculated from the nanoindentation curves using the Oliver-Pharr method[28] and are shown in Figure 3.12. Both *H* and E_{eff} for the polyimide nanocomposites increased markedly with the SiO_2 content

in the polyimide. This result indicated that the SiO_2 in the polymer matrix acts as a reinforcement against deformation, thus improving it's mechanical properties.

3.5 Conclusions

SiO_2-polyimide nanocomposites were successfully prepared by attaching a DETAS to SiO_2 surfaces and subsequently reacting them with phthalic anhydride in order to increase the compatibility and generate interfacial interactions between the silica nanoparticles and the polyimide. The modified silica nanoparticles were homogeneously dispersed in polyimide matrices up to 20 wt% of SiO_2 nanoparticles, without showing any microphase aggregation or significant decreases in transparency for any of the nanocomposite films. T_d and T_g values decreased with increasing silica content, probably due to the plasticizing effect of the surface ligands on the P-SiO_2. CTE values decreased with increases in the silica content; the CTE value of 20 wt% SiO_2-PI nanocomposite was 27.8×10^{-6} $°C^{-1}$, which is significantly smaller than that of parent polyimide (33.9×10^{-6} $°C^{-1}$). The nanoindentation results showed that both H and E_{eff} were enhanced with increasing silica content, corroborating the potential of these modified SiO_2 nanofillers for applications requiring a low CTE and high thermal stability, along with optical transparency.

Acknowledgements

I would like to thank Jeong-Hee Kim and Prof. Byeong-Hyeok Sohn for preparing cross-sectional TEM samples by microtoming. I would also like to extend my appreciation to Jong-Heon Kim and Prof. Dongil Kwon for their nanoindentation test.

3.6 References

[1] Li, Y.; Fu, S. Y.; Li, Y. Q.; Pan, Q. Y.; Xu, G. S.; Yuu, C. Y., *Compos. Sci. Technol.* **2007,** *67*, 2408-2416.

[2] Hasegawa, T.; Horie, K., *Prog. Polym. Sci.* **2001,** *26*, 259-335.

[3] Hsiao, S. H.; Guo, W. J.; Chung, C. L.; Chen, W. T., *Eur. Polym. J.* **2010,** *46*, 1878-1890.

[4] Chen, B.-K.; Wu, T.-Y.; Lin, C.-H.; Wong, J.-M., *Fiber. Polym.* **2013,** *14*, 1051-1057.

[5] Wang, Z. D.; Lu, J. J.; Li, Y.; Fu, S. Y.; Jiang, S. Q.; Zhao, X. X., *Compos. Part A-Appl. S.* **2006,** *37*, 74-79.

[6] Zhmurkin, D. V.; Gross, T. S.; Buchwalter, L. P.; Kaufman, F. B., *J. Electron. Mater.* **1996,** *25*, 976-982.

[7] Tang, J. C.; Lin, G. L.; Yang, H. C.; Jiang, G. J.; Chen-Yang, Y. W., *J. Appl. Polym. Sci.* **2007,** *104*, 4096-4105.

[8] Fu, S. Y.; Zheng, B., *Chem. Mater.* **2008,** *20*, 1090-1098.

[9] Hsiao, S. H.; Liou, G. S.; Chang, L. M., *J. Appl. Polym. Sci.* **2001,** *80*, 2067-2072.

[10] Knopp, D.; Tang, D. P.; Niessner, R., *Anal. Chim. Acta.* **2009,** *647*, 14-30.

[11] Schottner, G., *Chem. Mater.* **2001,** *13*, 3422-3435.

[12] Ahmad, Z.; Mark, J. E., *Chem. Mater.* **2001,** *13*, 3320-3330.

[13] Ragosta, G.; Musto, P., *Express Polym. Lett.* **2009,** *3*, 413-428.

[14] Chen, B. K.; Chiu, T. M.; Tsay, S. Y., *J. Appl. Polym. Sci.* **2004,** *94*, 382-393.

[15] Shang, Z. P.; Lu, C. L.; Lu, X. D.; Gao, L. X., *J. Appl. Polym. Sci.* **2008,** *109*, 3477-3483.

[16] Tang, J. C.; Yang, H. C.; Chen, S. Y.; Chen-Yang, Y. W., *Polym. Composite.* **2007,** *28*, 575-581.

[17] Stober, W.; Fink, A.; Bohn, E., *J. Colloid. Interf. Sci.* **1968,** *26*, 62-&.

[18] Jung, H. S.; Moon, D. S.; Lee, J. K., *J. Nanomater.* **2012,** *2012*, 593471.

[19] Li, H.; Liu, G.; Liu, B.; Chen, W.; Chen, S., *Mater. Lett.* **2007,** *61*, 1507-1511.

[20] Kotera, M.; Nishino, T.; Nakamae, K., *Polymer* **2000,** *41*, 3615-3619.

[21] Jou, J. H.; Huang, P. T., *Macromolecules* **1991,** *24*, 3796-3803.

[22] Totu, E.; Segal, E.; Covington, A. K., *J. Therm. Anal. Calorim.* **1998,** *52*, 383-391.

[23] Sun, Y. Y.; Zhang, Z. Q.; Moon, K. S.; Wong, C. P., *J. Polym. Sci., Part B: Polym. Phys.* **2004,** *42*, 3849-3858.

[24] Ash, B. J.; Schadler, L. S.; Siegel, R. W., *Mater. Lett.* **2002,** *55*, 83-87.

[25] Katz, H. S.; Mileski, J. V., *Handbook Of Fillers For Plastics*. Springer: **1987**.

[26] Dhakal, H. N.; Zhang, Z. Y.; Richardson, M. O. W., *Polym. Test.* **2006,** *25*, 846-852.

[27] Hu, Y. C.; Shen, L.; Yang, H.; Wang, M.; Liu, T. X.; Liang, T.; Zhang, J., *Polym. Test.* **2006,** *25*, 492-497.

[28] Oliver, W. C.; Pharr, G. M., *J. Mater. Res.* **1992,** *7*, 1564-1583.

Chapter 4.

Polymer Nanocomposites for Electronic Applications

Abstract

Polymer nanocomposites with high-*k* metal oxide (TiO_2 and $BaTiO_3$) were successfully fabricated for dielectric layer in organic thin film transistor (OTFTs). The surface of the each nanoparticle was modified by the ligands to enhance their compatibility with the polymer. Consequently, no significant aggregation of the nanoparticles, even at high concentration of nanofiller, was found in all the nanocomposites, as observed by transmission electron microscopy (TEM). Dielectric properties and OTFTs performance are only demonstrated with TiO_2-PVP nanocomposites. TiO_2-PVP nanocomposites exhibited a low leakage current density (~10^{-8} A/cm^{-2}). With an increase in the concentration of TiO_2 nanoparticles added, the dielectric constant of the nanocomposites also increased proportionately as compared to that of pristine PVP. The performance of the OTFTs in terms of the charge carrier mobility, on/off ratio, threshold voltages, and hysteresis was evaluated. In addition, the relationship between the concentration of TiO_2 nanoparticles and the device performance is discussed in detail.

Introduction

Organic thin film transistors (OTFTs) are receiving increased attention because of their numerous advantages, such as low-cost, light-weight, easy processing, and flexibility.[1-3] Figure 4.1 shows the common device configurations of OTFTs. Depending on the position of the gate electrode, structure of OTFTs is divided into two types, bottom-gate or top-gate. Two configurations employed in bottom-gate structure known as top contact and bottom contact, depending on the position of the source and drain electrodes[4].

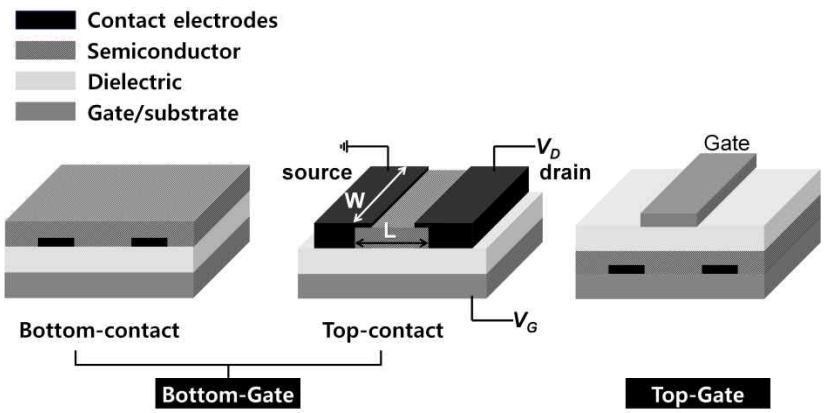

Figure 4.1. Different configurations of organic field-effect transistors.

The operation of an OTFT can be explained as follows[4]. The positive/negative voltage applied to the gate electrode, negative/positive charges are induced in interface between insulator and semiconductor. The gate voltage (V_G) and the capacitance of the insulator (C) affect the accumulated charge density in insultor/semiconductor interface. The OTFTs device is "off" state, when no voltage is applied in source and gate. With increasing both V_G and V_D (voltage between source and drain), the source-

drain current (I_D) flowing along the semiconductor material is increased linearly at low drain voltage followed by saturated at higher V_D. The standard source-drain current equation in linear region is

$$|I_D|_{lin} = C\mu V_D(V_G - V_{th} - V_D/2)^2 W/L$$

The standard source-drain current equation in saturation region is

$$|I_D|_{sat} = C\mu(V_G - V_{th})^2 W/2L$$

Where W is the channel width, L is the channel length, V_{th} is the threshold voltage and μ is the field-effect mobility. In above equation, source-drain current can be increased by V_G. However, the high operating voltage is not appropriate for various OTFTs applications such as portable electronics and smart cards.[5] Another way to increase source-drain current is increasing capacitance of the insulator as described by following equation:

$$C = \varepsilon_0 k/d$$

Where ε_0 is the permittivity of vacuum, k is the dielectric constant of the insulator, and d is the thickness of insulator. This above equation indicated that the source-drain current can be enhanced by either increasing k or decreasing d, because source-drain current is proportional to the capacitance of the dielectric. However, the thickness of the insulator is decreased, leakage current exponentially increased[4]. Clearly, to operate OTFTs at low voltage, insulator with high-k is needed.

Polymers such as poly(4-vinylphenol) (PVP), polystyrene (PS)[6], poly(methylmethacrylate) (PMMA)[6], poly(perfluorobutenylvinylether) (CYTOP)[6], and polyimide[7] are ubiquitously used as dielectric gate materials for OTFTs, but their low-*k* (*k*: dielectric constant) values (Figure 4.2, Table 4.1) cause a serious impediment to their applications.[8] This is because OTFTs based on polymer dielectrics require a high operating voltage. To this end, various inorganic materials having high dielectric constants (Table 4.2) have been incorporated; however, even they have disadvantages owing to their limited flexibility, and expensive and complicated fabrication, both of which entail high annealing temperatures and vacuum deposition processes.[4] However, reports have shown that solution-processed polymer-inorganic nanoparticle composites might overcome the limitations of both polymer and inorganic dielectric materials.[7, 9-11] High-*k* inorganic fillers, which include nanopariticles such as titanium dioxide (TiO_2)[12], aluminum oxide (Al_2O_3)[12], barium titanate ($BaTiO_3$)[13], and hafnium dioxide (HfO_2)[14], are commonly used to enhance the dielectric constant of polymer-based nanocomposite, without significantly affecting the advantages of the polymer matrix, such as easy processing and flexibility.

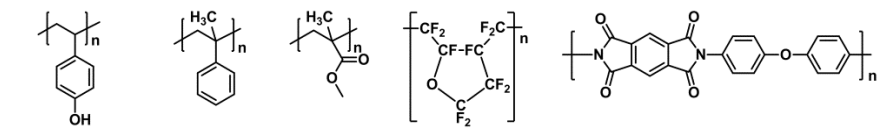

Figure 4.2. Common organic polymers used as gate insulators

Table 4.1. Dielectric properties for various polymer gate dielectrics

Dielectric	Method	Thickness (nm)	Dielectric constant, *k*	Ref
PVP	Spin coating	147	3.5	this work
PS	spin coating	500-700	2.5	6
PMMA	spin coating	600-900	3.6	6
Cytop	spin coating	450-600	2.1	6
Polyimide	spin coating	400-500	3.7	7

Table 4.2. Dielectric properties for various inorganic gate dielectrics

Dielectric	Method	Thickness (nm)	Dielectric constant, *k*	Ref
TiO_2	sputtering	97	41	12
HfO_2	sol-gel	20	11	14
Al_2O_3	sputtering	93	8.4	12
$BaTiO_3$	sol-gel	3,000	720	13

Polymer nanocomposites with electrically conductive nanofiller such as metal nanoparticles[15-16] or carbon-based nanostructure[17-18] is another approach towards high-*k* nanocomposite dielectrics. Because interfacial polarization between the conductive filler and polymer interface contribute to the enhanced dielectric constant.[19]

Despite these benefits, nanocomposite based OTFTs have suffered from the problem of high leakage current density due to the lack of compatibility between polymer and inorganic nanoparticles. In addition, if nanoparticles are poorly distributed in the nanocomposite dielectrics, the roughness at the

interface between the gate insulator and semiconductor increased, and eventually deteriorates the performance of the OTFTs by carrier scattering and trapping.[7, 10, 20-21]

In this chapter, TiO_2-PVP and $BaTiO_3$-PVP nanocomposite dielectrics were fabricated. To increase compatibility between nanoparticle and polymer, each nanoparticles is modified with ligands which have structurally similarity of polymer are introduced on the surface of nanoparticles. The enhancement of dielectric constant is achieved in both TiO_2-PVP and $BaTiO_3$-PVP nanocomposites dielectrics due to relatively high dielectric constant of TiO_2 and $BaTiO_3$ compare to that of PVP.

Chapter 4

Part 1. TiO_2-PVP Nanocomposite Dielectrics for Organic Thin Film Transistors

4.1.1 Introduction

In this part, TiO_2-PVP nanocomposite was fabricated for gate insulator in OTFTs, which consists of poly(4-vinylphenol) (PVP) as the matrix, poly(melamine-co-formaldehyde) methylated/butylated (PMF) as the cross-linker, and TiO_2 nanoparticles as the filler. To enhance the compatibility of the nanoparticles with the matrix, the surface of the nanoparticles were modified with 4-hydroxybenzoic acid, a ligand similar in structure to the repeat units in PVP. The ligands were later cross-linked with PMF in a curing process. As shown in our previous research, the interactions between the polymer and the surface ligands on the nanoparticles, which have similar chemical structures, was strong enough to produce homogeneously disperse nanoparticle/polymer composites.[22] No considerable aggregation of TiO_2 nanoparticles was found using a transmission electron microscopy (TEM), even when the concentration of the nanoparticles in the composite was as high as 31 wt %. Various nanocomposite films of TiO_2-PVP were prepared by spin-coating on an indium tin oxide (ITO)-glass substrate, as a gate insulator layer, and the dielectric constant of the nanocomposites increased proportionally with the concentration of TiO_2. All the nanocomposite insulator films exhibited a

reasonably low leakage current density (~10^{-8} A/cm^2). Once incorporated in an OTFT as the gate insulator, the increased dielectric constant of the nanocomposite as compared to that of pristine PVP enhanced the device performance such as field-effect mobility, on/off ratio, and threshold voltage. In particular, OTFTs with a TiO_2-PVP nanocomposite dielectric layer could successively operate at a low gate voltage, V_G = -5 V.

4.1.2 Experimental Section

Titanium (IV) *n*-propoxide, toluene, stearic acid, *t*-butylamine, pentacene, 4-hydroxybenzoic acid (4HBA), poly (4-vinylphenol) (PVP, Mw = 25,000), poly(melamine-co-formaldehyde) methylated/butylated (PMF) were purchased from Aldrich. Acetone, tetrahydrofuran (THF), isopropyl alcohol, and chloroform were purchased from Samchun Chemical Co. Ethanol was purchased from J. T. Baker. All organic solvents were reagent grade and used without further purification.

Synthesis of TiO_2 nanoparticles

TiO_2 nanoparticles were obtained using a two-phase thermal synthesis method, which was a slight modification of a method reported elsewhere.[23] A solution containing 0.2 mL of *t*-butylamine in 20 mL of water was prepared in a Teflon-lined steel autoclave. 0.3 mL of titanium(IV) *n*-propoxide was added to a solution of 1 g of stearic acid dissolved in 20 mL of toluene and the final solution was transferred to the autoclave. The autoclave was sealed and heated to 180 °C for 12 h without any stirring of its contents and cooled to room temperature. The reaction solution precipitated with ethanol and the precipitate was centrifuged for 10 min at 4,000 rpm. The precipitate was redispersed in a small amount (~3 mL) of chloroform with vortexing and then reprecipitated with ethanol. This precipitation/redispersion procedure was repeated twice. The dispersion of TiO_2 nanoparticles in chloroform was centrifuged at 4,000 rpm for 10 min to remove any aggregated particles. A white colored supernatant, which was a dispersion of stearic acid-stabilized TiO_2 nanoparticles (SA-TiO_2), was collected for the next step.

A solution of 4-hydroxybenzoic acid (2 g of 4HBA in 20 mL of THF) was

added drop by drop to a dispersion of SA-TiO_2 (200 mg SA-TiO_2 in 20 mL of chloroform). The mixture was stirred at 60 °C for 24 h and then cooled to room temperature. 4HBA-modified TiO_2 nanoparticles were precipitated by adding a large excess (400 mL) of chloroform followed by centrifugation for 10 min at 4,000 rpm. The precipitate was redispersed in a small amount (~3 mL) of ethanol with vortexing and then reprecipitated with chloroform. This precipitation/redispersion procedure was repeated twice. The dispersion of 4HBA-modified TiO_2 nanoparticles in ethanol was centrifuged at 4,000 rpm for 10 min to remove any aggregated particles, and the yellow colored supernatant (4HBA-TiO_2) was collected for the next step.

Preparation of TiO_2-PVP nanocomposite solutions

PVP and PMF (2:1 wt. ratio) were added to an appropriate amount (see the concentration below) of 4HBA-TiO_2 (13 mg/mL in ethanol), and the mixture was stirred vigorously at room temperature for one day. Four different solutions, which could produce 3, 7, 14, and 31 wt % of TiO_2 in nanocomposite films, respectively, were prepared by varying the amount of 4HBA-TiO_2 nanoparticles.

Fabrication of OTFTs

OTFTs were fabricated on ITO glass substrates (thickness: 120 nm, sheet resistance: 15 Ω/sq). ITO glass substrates were cleaned sequentially with isopropyl alcohol, acetone, distilled water in an ultrasonic bath, and then dried with nitrogen. TiO_2-PVP nanocomposite films were prepared from the nanocomposite solutions having different concentrations of TiO_2 nanoparticles, by spin-coating them on cleaned ITO glass substrates at 4,000 rpm for 60 sec

followed by curing at 200 °C for 1 h. In order to make the surface of 7 wt % TiO_2-PVP nanocomposite film smooth, a 0.5 wt % of PVP solution was further spin-coated on the nanocomposite film at 4,000 rpm for 60 sec, and then cured at 200 °C for 30 min (7 wt % TiO_2-PVP/PVP nanocomposite). Pentacene was subsequently deposited thermally at a pressure of ~3×10^{-6} Torr (thickness: 500 Å, growth rate: 0.5 Å/s). Finally, the top contact gold (Au) electrodes (thickness: 60 nm) were deposited thermally at a pressure of ~3×10^{-6} Torr (growth rate: 5 Å/s) using a shadow mask with a channel length (L) and width (W) of 150 μm and 1,000 μm, respectively.

Characterization

Fourier-transform infrared (FT-IR) spectra were recorded on a spectrometer (NICOLET iS10) in the wavelength range from 400 to 4000 cm^{-1}, to study the surface of the TiO_2 nanoparticles. Transmission electron microscopy (TEM) images were acquired using a microscope (Hitachi-7600) operating at 100 kV. Atomic force microscopy was performed on a microscope (AFM, Veeco Multimode 8) operated in the tapping mode. X-ray diffraction patterns of TiO_2 nanoparticles and pentacene films deposited on various dielectrics were recorded using Bruker New D8 Advance instrument. The static contact angles of distilled water and diiodomethane (DIM) on different nanocomposite dielectrics were obtained by a Kruss DSA 10 contact angle analyzer. The surface energy of each nanocomposite dielectric was calculated from the corrected contact angles using the Owens-Wendt equation.

The performance of the OTFTs was characterized using a probe station equipped with an Agilent 4155B semiconductor parameter analyzer. The capacitance of the dielectric nanocomposites were measured using an Agilent

4284A 1 kHz precision inductance-capacitance-resistance (LCR) meter at driving frequencies of 1 kHz, 10 kHz, 100 kHz, and 1 MHz. All electrical characterizations of the OTFTs were carried out at ambient conditions and a dark environment. The thickness of the dielectric nanocomposites was measured using K-MAC, ST2000-DLXn instrument.

4.1.3 Results and Discussion

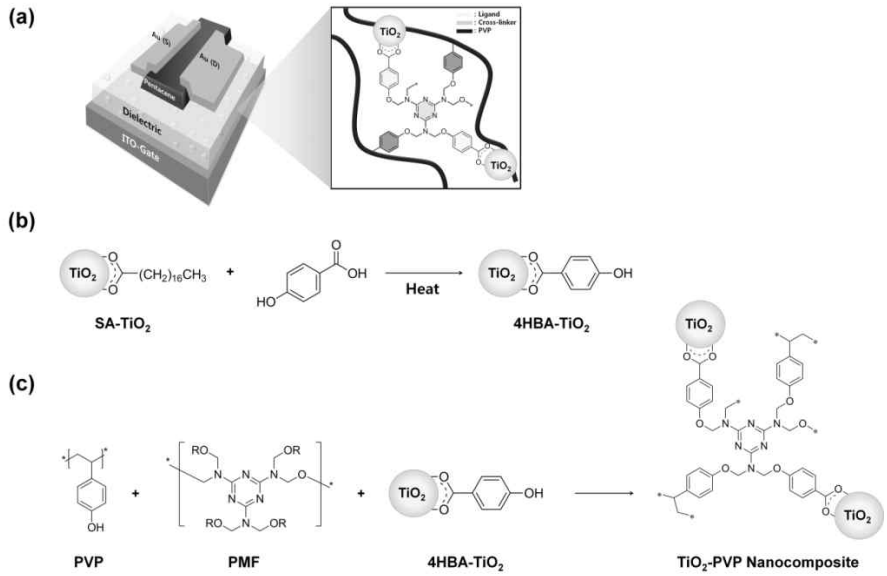

Scheme 4.1.1. (a) A schematic of an OTFT fabricated with a TiO_2-PVP nanocomposite as the gate insulator; (b) ligand exchange on 5 nm sized TiO_2 nanoparticles; and (c) fabrication of TiO_2-PVP nanocomposite dielectrics.

TiO_2 nanoparticles capped by stearic acid (SA-TiO_2) were dispersed well in chloroform (Figure 4.1.1a). Due to the long alkyl chain originated from the stearic acid, SA-TiO_2 were not dispersed in ethanol, N-metyl-2-pyrrolidone (NMP), and propylene glycol monomethyl ether acetate (PEGMEA), which are commonly employed solvent for dissolving PVP. As a result, precipitation was occurred in all solutions after few hours (Figure 4.1.2a). The SA-TiO_2 in ethanol dispersion was added to the 2 : 1 weight ratio of PVP and PMF mixture, and then stirred vigorously at room temperature for a day. The concentration of TiO2 in polymer is 7 wt%. As shown in Figure 4-2b, turbid solution was obtained, which means that the nanoparticles form aggregation

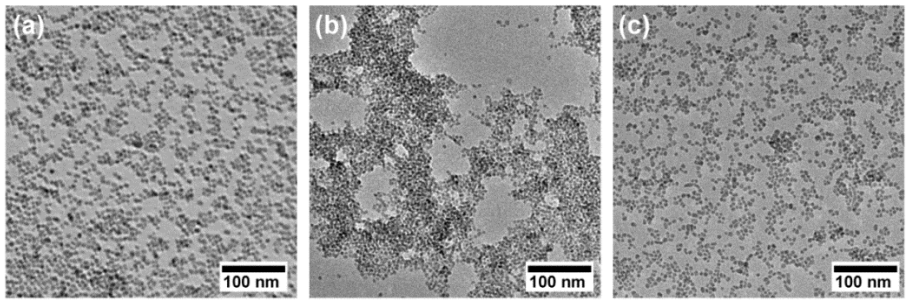

Figure 4.1.1. TEM images of (a) SA-TiO_2, (b) aggregated and (c) mono-dispersed 4HBA-TiO_2.

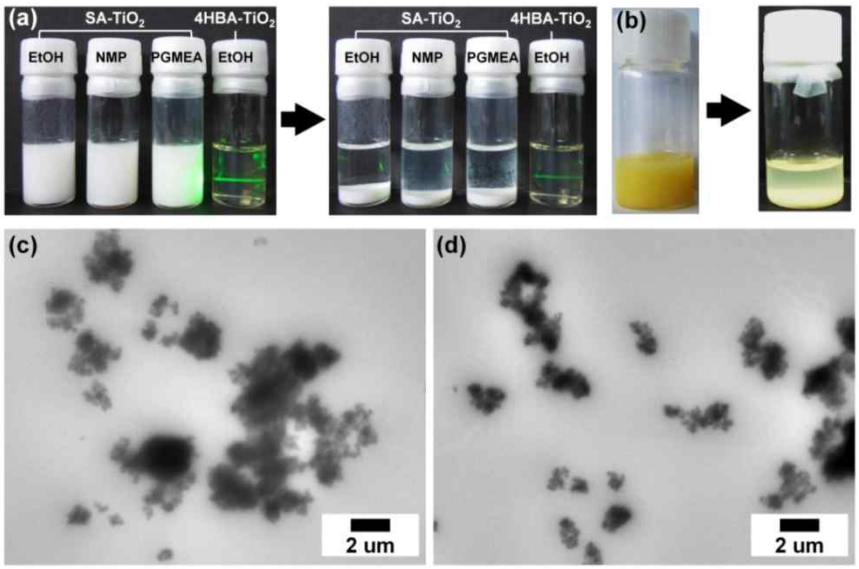

Figure 4.1.2. (a) Digital photographs of SA-TiO_2 dispersed in various solvent, (b) SA-TiO_2-PVP nanocomposite solution and (c), (d) TEM images of 7 wt% SA-TiO2-PVP nanocomposite.

in polymer solution. Furthermore, nanoparticles generated microphase aggregation in polymer matrix as shown in TEM images (Figure 4.1.3c,d), because highly hydrophobic surfaces of SA-TiO_2 are less compatible with the

polar hydroxyl group in PVP. Therefore, a ligand exchange reaction was performed with the ligand, 4-hydroxybenzoic acid, having a chemical structure similar to the monomer of PVP, in order to increase the interaction between the polymer and the nanoparticles. SA-TiO_2 were well dispersed not in ethanol but in chloroform while 4-hydroxybenzoic acid were very soluble not in chloroform but in ethanol. When a solution of 4-hydroxybenzoic acid in ethanol added to a dispersion of SA-TiO_2 in chloroform, nanoparticles form large aggregation during the mixing (Figure 4.1.1b). Therefore, in order to ligand exchange without any aggregation, 4-hydroxybenzoic acid was dissolved in THF and the solution was added to a dispersion of SA-TiO_2 in chloroform, because both of 4-hydroxybenzoic acid and SA-TiO_2 were well dissolved (dispersed) in THF. The colorless SA-TiO_2 dispersion rapidly turned yellow as soon as the solution of 4-hydroxybenzoic acid was added due to the ligand to TiO_2 charge transfer transition within the surface.[24] The mixture was heated to 60 ℃ (Scheme 4.1.1). After the ligand exchange with 4-hydroxybenzoic acid (4HBA), 4HBA-TiO_2 nanoparticles were dispersed well in ethanol without any aggregation of the nanoparticles (Figure 4.1.1c). However, this was not the case in chloroform. TEM image showed no significant change in the size or shape of the nanoparticles after the ligand exchange (Figure 4.1.1c). The X-ray diffraction (XRD) patterns of SA-TiO_2 and 4HBA-TiO_2 nanoparticles matched well to that of the bulk anatase TiO_2 (Figure 4.1.3a). The crystal sizes of SA-TiO_2 and 4HBA-TiO_2 nanoparticles were calculated as 5.5 nm using the Scherrer equation, which was in good agreement with those found in the TEM images. Figure 4.1.3b shows the FT-IR spectra of SA-TiO_2, 4-hydroxybenzoic acid, and 4HBA-TiO_2; confirming the presence of 4-hydoxybenzoic acid ligand on the surface of 4HBA-TiO_2 as

the 4HBA capped nanoparticles exhibited FT-IR absorption peaks at 1608, 1496, 1409, 1278, 1172, 1097 and 1043 cm^{-1} due to the presence of 4-hydoxybenzoic acid.

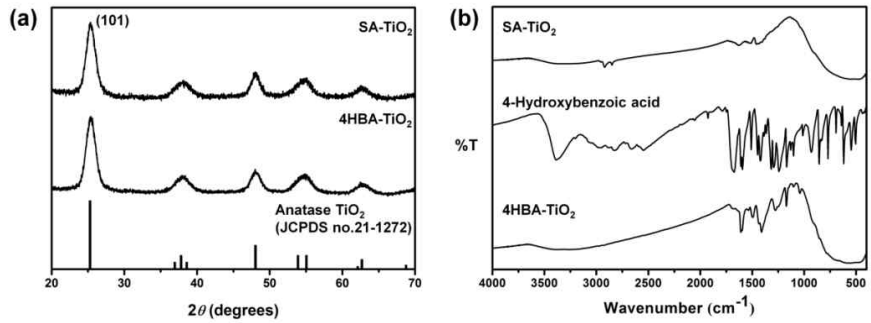

Figure 4.1.3. (a) XRD patterns of SA-TiO_2 nanoparticles and 4HBA- TiO_2 nanoparticles. (b) FT-IR spectra of SA-TiO_2 nanoparticles, 4-hydroxybenzoic acid and 4HBA-TiO_2 nanoparticles.

TiO_2-PVP nanocomposite solutions were prepared by mixing PVP, PMF, and 4HBA-TiO_2 dispersed in ethanol, and stirring the mixture for one day. As shown in Figure 4.1.4a, no precipitation was found in any of the solutions, even after 24 h. The TEM images of four different samples show that TiO_2 nanoparticles were homogeneously dispersed in the PVP matrix and no significant aggregation was found even at 31 wt % of TiO_2 nanoparticles in PVP (Figure 4.1.4b-e). This proves that the chemical interaction between the ligands and the polymer chains enhanced the miscibility of the inorganic nanoparticles and the organic polymer. Figure 4.1.5 shows the AFM images of the surface of different TiO_2-PVP nanocomposite dielectric layers having different compositions. The root-mean-square roughness (R_{rms}) values obtained for an area of 1 μm × 1 μm area are summarized in Table 4.1.1. As

can be seen, the surface roughness of the nanocomposite films increased proportionately with the concentration of TiO_2 in the PVP matrix.

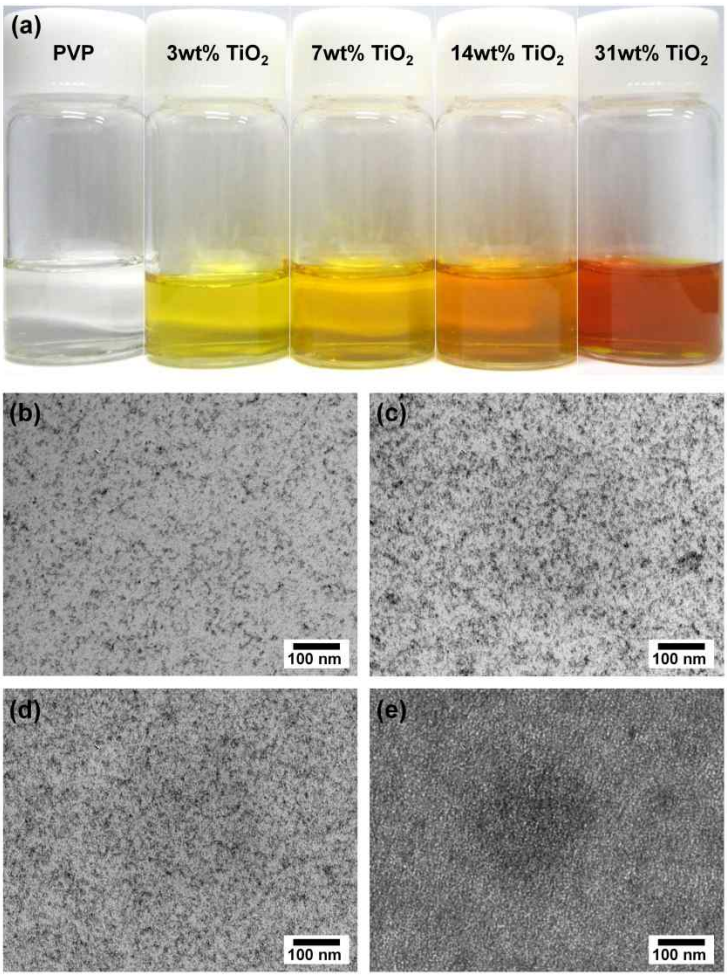

Figure 4.1.4. (a) PVP and TiO_2-PVP nanocomposite solutions. TEM images of TiO_2-PVP nanocomposites having: (b) 3, (c) 7, (d) 14, and (e) 31 wt % of TiO_2 in PVP. The TEM images were obtained by spin-coating TiO_2-PVP nanocomposite solutions onto a TEM grid, followed by curing at 200 °C for 1 h.

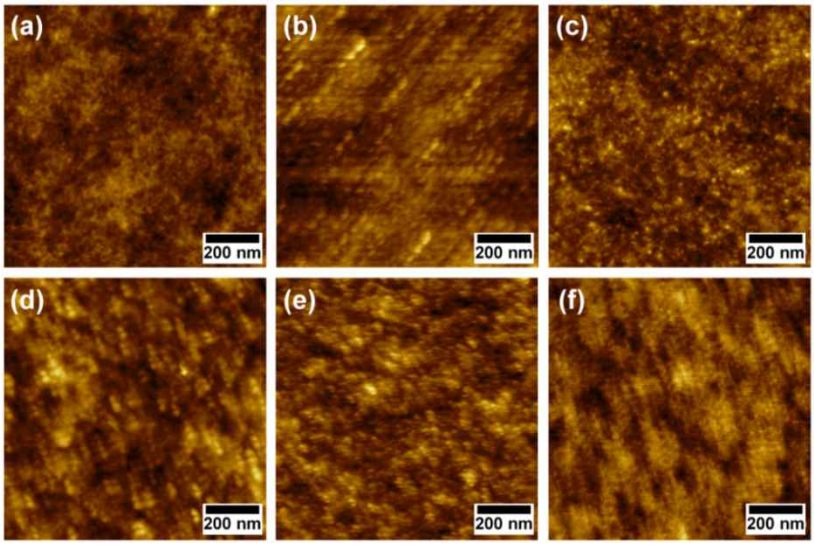

Figure 4.1.5. AFM images of the surface of dielectric layers of (a) PVP and TiO_2-PVP nanocomposites having (b) 3, (c) 7, (d) 14, (e) 31 wt % of TiO_2 nanoparticles in PVP, and (f) 7 wt % TiO_2/PVP.

AFM images show the morphology of 50 nm thick pentacene layers deposited on a PVP layer and various TiO_2-PVP nanocomposite dielectric layers (Figure 4.1.6). The grain sizes of pentacene gradually decreased as the content of TiO_2 in the nanocomposite increased (Figure 4.1.6g). As reported earlier, we found that the growth of pentacene was seriously affected by the surface energy and roughness of the dielectric layers.[25-26] Since there was no considerable difference in the surface energies (γ) of the different TiO_2-PVP nanocomposite dielectric layers (Table 4.1.1), the surface roughness increase from 0.26 to 2.13 nm could have played a major role in controlling the grain size of the pentacene layers. X-ray diffraction was performed to investigate the crystallinity of pentacene deposited on different dielectric layers (Figure 4.1.6h). First-order diffraction peaks at a scattering angle of 5.76°, with a corresponding *d*-spacing of 15.3 Å, was observed in all the samples. The

intensity of this peak decreased with the increase in the concentration of TiO_2 in the dielectric layers. This result is in good agreement with the observation of the grain size of pentacene from the AFM images; smaller grain size showed lower intensity, because rough dielectric surfaces disturb the ordering of pentacene molecules, which causes a reduction of grain size and the intensity of the XRD peaks.

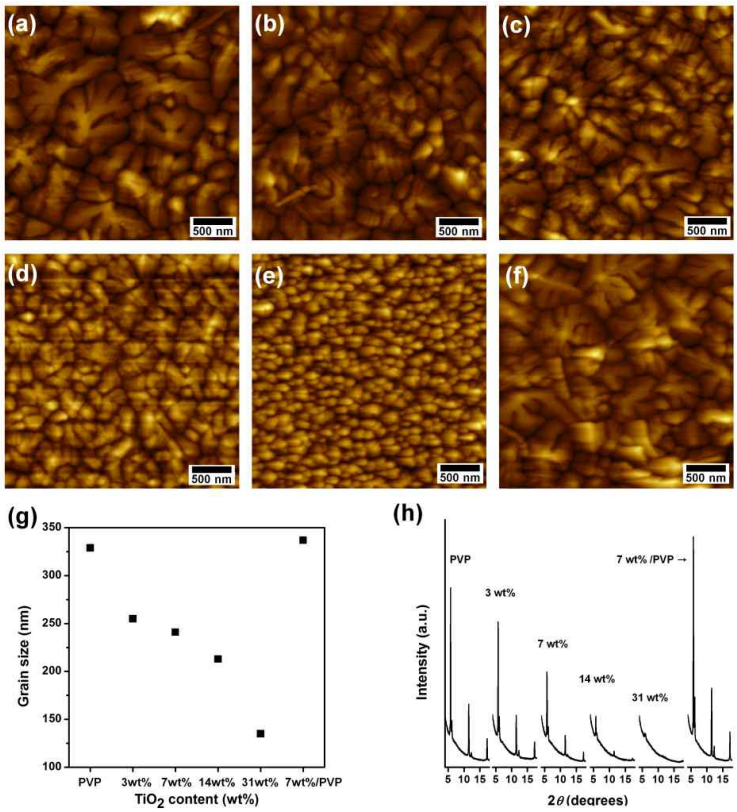

Figure 4.1.6. AFM images of the morphology of pentacene deposited on (a) PVP and TiO_2-PVP nanocomposites having: (b) 3, (c) 7, (d) 14, (e) 31 wt % of TiO_2 nanoparticles in PVP, and (f) 7 wt % TiO_2/PVP. (g) Average grain size, and (h) XRD patterns of the pentacene film on different nanocomposite dielectric layers.

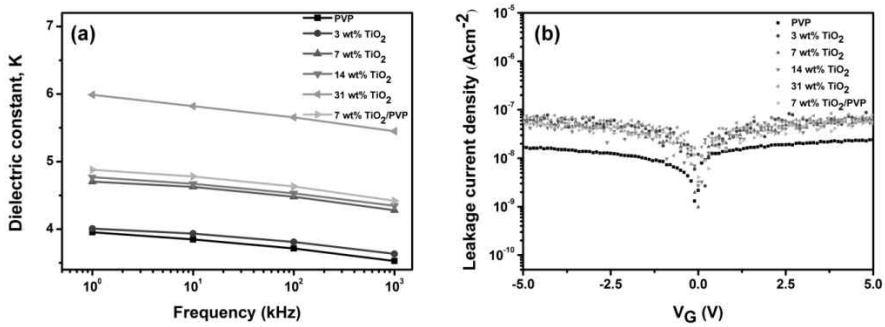

Figure 4.1.7. (a) Dielectric constant vs. frequency and (b) leakage current density of PVP and TiO¬2-PVP nanocomposites vs. gate volatage.

Table 4.1.1. Dielectric and surface properties of PVP and TiO_2-PVP nanocomposite.

	Thick-ness (nm)	k (1 MHz)	R_{rms} (nm)	Contact angle (°)		γ (mJ/m^2)
				H_2O	DIM	
PVP	147	3.53	0.26	81	42	41
3 wt% TiO_2–PVP	165	3.63	0.39	73	32	48
7 wt% TiO_2–PVP	176	4.28	0.54	77	32	47
14 wt% TiO_2–PVP	207	4.34	0.64	72	31	49
31 wt% TiO_2–PVP	326	5.45	2.13	76	36	46
7 wt% TiO_2-PVP/PVP	195	4.42	0.27	79	32	46

Table 4.1.2. Comparisons of the measured and calculated dielectric constants of PVP and TiO_2-PVP nanocomposites.

wt% of TiO_2	vol% of TiO_2	Experimental value of k (1 MHz)	Calculate k from Maxell model	Calculate k from Jaysundere-Smith model
Neat PVP	-	3.53	-	-
3	1	3.63	3.61	3.61
7	2	4.28	3.70	3.70
14	5	4.34	3.96	4.01
31	11	5.45	4.52	4.76

Figure 4.1.7a shows the dielectric constant of the nanocomposites as a function of the concentration of TiO_2 in the PVP matrix, measured in the frequency range from 1 kHz to 1 MHz. The dielectric constant of nanocomposites increased with the concentration of TiO_2 for the whole frequency range measured. Anatase TiO_2 has a relatively higher dielectric constant (k = 40)[27] compared the PVP, which is what would have contributed to an increase in the dielectric constant of nanocomposites. However, the dielectric constants of pristine PVP and nanocomposite dielectric layer with 31 wt% TiO_2 are 3.53 and 4.42, respectively; seemingly slight enhancement in dielectric constant of nanocomposite is obtained despite of the addition of a large amount of TiO_2. One thing to mention is that the wt% value were used because it was easy to weight and calculated the percentage of TiO_2, but these values are changed into much smaller ones when they are converted to vol% as show in Table 4.1.2. Dielectric constant was calculated using two different models, *Maxwell* model[28] and *Jaysundere-Smith* model[29]. The dielectric constant by Maxwell equation is

$$\varepsilon_c = \varepsilon_m \frac{\varepsilon_f + 2\varepsilon_m - 2(1-\phi_m)(\varepsilon_m - \varepsilon_f)}{\varepsilon_f + 2\varepsilon_m + (1-\phi_m)(\varepsilon_m - \varepsilon_f)}$$

where the subscripts *m, f* represent the polymer and the filler phase, respectively. ε and ϕ are the dielectric constant and the volume fraction of the constituents. The *Maxwell* model is based on a mean field approximation of single spherical filler surrounded by a continuous matrix, thus it is usually applied only for a low concentration of filler in matrix[30]. On the other hand, *Jaysundere-Smith* model considers interaction between fillers at a high concentration[31]. *Jaysundere-Smith* equation form is given below:

$$\varepsilon_c = \frac{\varepsilon_m \phi_m + \varepsilon_f \phi_f \frac{3\varepsilon_m}{(2\varepsilon_m + \varepsilon_f)}\left[1 + 3\phi_f \frac{(\varepsilon_f - \varepsilon_m)}{2\varepsilon_m + \varepsilon_f}\right]}{\phi_m + \phi_f \frac{3\varepsilon_m}{(2\varepsilon_m + \varepsilon_f)}\left[1 + 3\phi_f \frac{(\varepsilon_f - \varepsilon_m)}{2\varepsilon_m + \varepsilon_f}\right]}$$

The comparisons of the experimental and calculated values from both models of dielectric constant are listed in Table 4.1.2. It shows that no significant difference is observed between the experimental and calculated values from two models. Thus, it is believed that measured dielectric constant values in our experiments are reasonable. From the point that calculated values from both models are almost same, it is corroborated that most of TiO_2 are well dispersed in PVP matrix and the interparticle interaction is negligible in our nanocomposite system because they occupy low volume fraction (11 vol%) in polymer matrix even though large amount (31 wt%) in weight ratio of TiO_2 is added. The interestingly low leakage current density of PVP and TiO_2-PVP nanocomposites at ± 5 V is shown in Figure 4.1.7b. Even though it has been reported that typically nanoparticles in a polymer matrix cause a

large leakage current due to nanoparticle aggregation,[4, 10] the leakage current density of all the TiO_2-PVP nanocomposites in our work was about 10^{-8} A/cm^2. This result confirms that the TiO_2 nanoparticles were homogeneously embedded in the PVP matrix owing to the enhanced chemical interaction between the surface ligands and the polymer chains and the miscibility of inorganic nanoparticle and organic polymer, which can attribute to no significant changes in the leakage current.

Figure 4.1.8 shows the transfer characteristics of the OTFT devices with pristine PVP and TiO_2-PVP nanocomposites as the gate insulator. Charge carrier mobilities in the saturation region were determined from the slope of the $|I_D|^{1/2}$ *vs.* V_G curve at V_D = -5 V, according to Equation 3 [32]

$$|I_D| = C\mu(V_G - V_{th})^2 W/2L$$

Where C is the capacitance of the dielectric layer, W is the channel width, L is the channel length, V_G is the gate voltage, V_{th} is the threshold voltage and μ is the field-effect mobility. The values of the mobility (μ), on/off ratio, and threshold voltage (V_{th}), extracted from the transfer curves are summarized in

Table 4.1.3. It is to be noted that the OTFTs with 3, 7, and 14 wt % TiO_2-PVP nanocomposites as the gate insulator have a higher mobility compared to that of the OTFT with pristine PVP. The enhancement of mobility was probably due to the increased charge carrier density at the interface between the dielectric and the semiconductor pentacene, caused by the increased dielectric constant. However, an increase in the mobility was not observed in OTFTs with nanocomposites having concentration of nanoparticles beyond 14 wt %, even though the dielectric constant was enhanced. This phenomenon can be explained by the correlation between the mobility and the ordering of

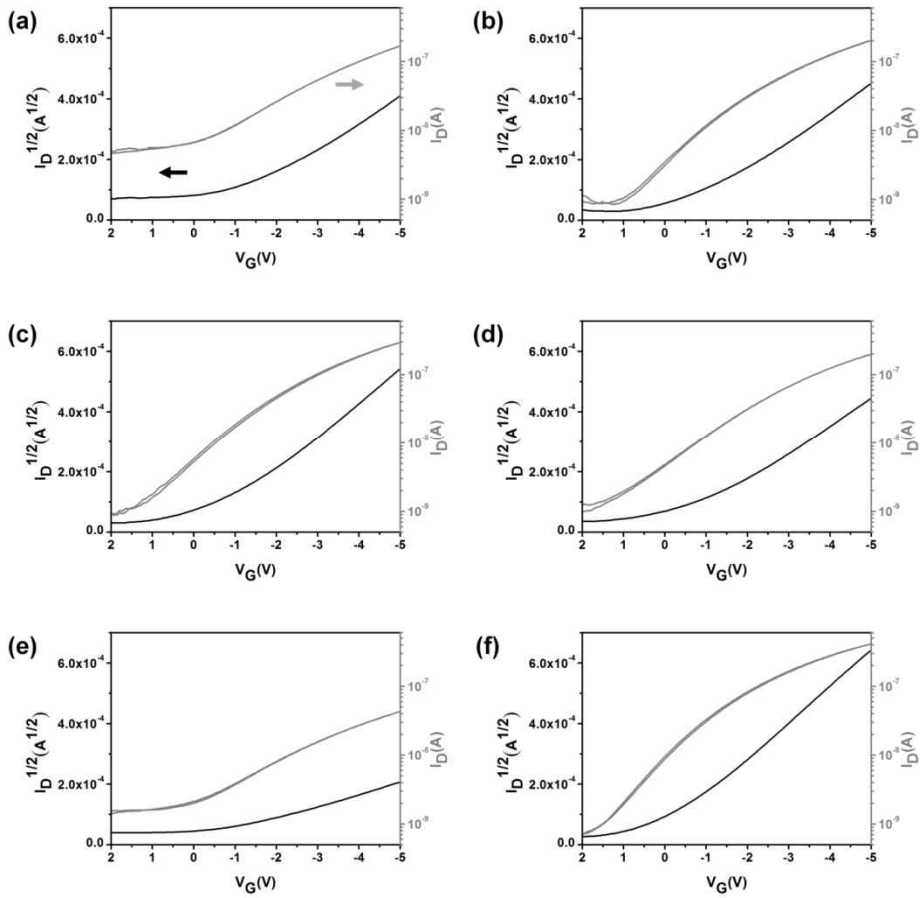

Figure 4.1.8 Transfer characteristics of OTFTs with (a) PVP and TiO_2-PVP nanocomposites having (b) 3, (c) 7, (d) 14, (e) 31 wt % TiO_2 nanoparticles in PVP, and (f) 7 wt % TiO_2/PVP as the gate insulator.

pentacene molecules. It is well known that charge carrier mobility is influenced by microstructure and morphology of the semiconductor molecules. Moreover, the surface roughness of dielectric layer on which the semiconductor film grows is an important factor in determining the morphology and grain size of the semiconductor layer.[21, 33-34] An increased

roughness causes a reduction of the π–π orbital overlap in conjugated molecules, which affects the disordering of pentacene on the dielectric surface. Therefore, the mobility is reduced by hindrance to the transportation of charges via the hopping process between neighboring pentacene molecules.[34-35] For OTFTs with nanocomposites having up to 7 wt % TiO_2, the charge carrier mobility was clearly affected by the charge carrier density. In other words, the charge carrier mobility was influenced by the dielectric constant. However, for OTFTs with nanocomposites having TiO_2 concentrations in PVP beyond 14 wt %, the mobility was affected not by the dielectric constant but by the morphology of pentacene molecules, which was further controlled by the surface roughness of the nanocomposite dielectric layer.

Table 4.1.3. Electrical properties of OTFTs with PVP and TiO_2-PVP nanocomposites as the gate insulator. (Operatiing voltage = -5 V)

	Mobility (cm^2/V s)	**On/off ratio**	**Threshold Voltage, V_{th} (V)**
PVP	0.114	2.7×10^1	-0.46
3 wt% TiO_2–PVP	0.147	2.4×10^2	-0.39
7 wt% TiO_2–PVP	0.184	3.2×10^2	-0.28
14 wt% TiO_2–PVP	0.141	1.6×10^2	-0.24
31 wt% TiO_2–PVP	0.035	2.7×10^1	-0.04
7 wt% TiO_2-PVP/PVP	0.220	5.7×10^2	0.32

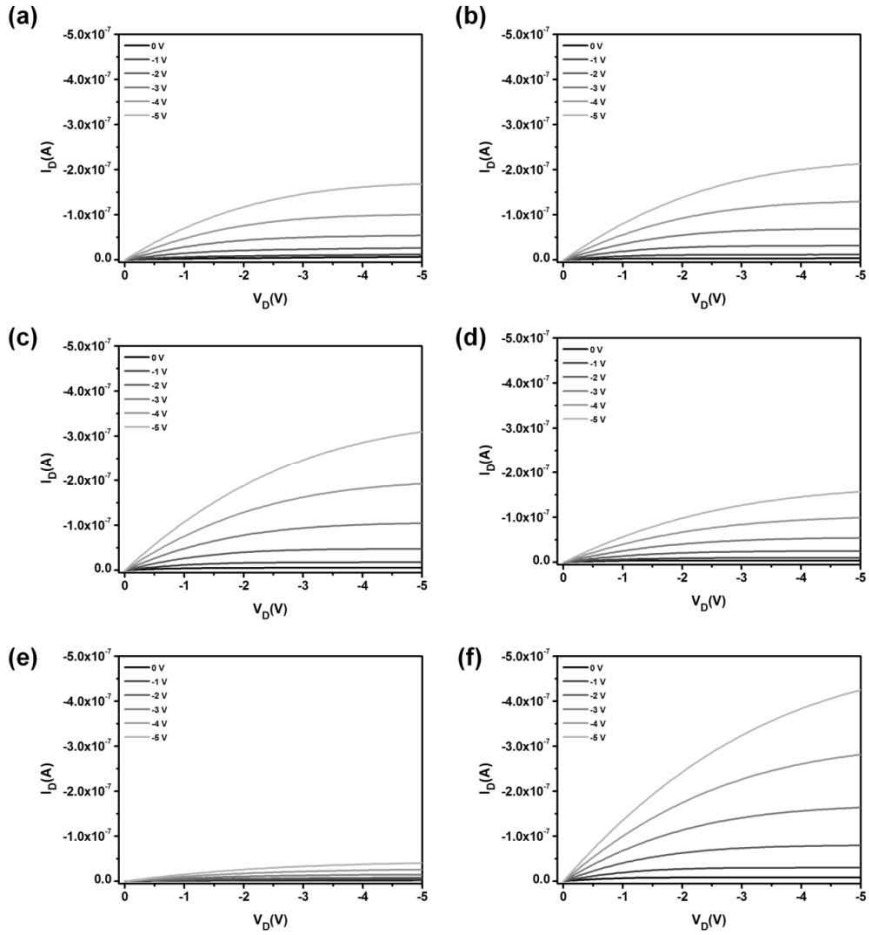

Figure 4.1.9. Output characteristics of OTFTs with (a) PVP and TiO_2-PVP nanocomposites having (b) 3, (c) 7, (d) 14, (e) 31 wt % of TiO_2 nanoparticles in PVP, and (f) 7 wt % TiO_2/PVP.

In order to reduce surface roughness and improve the interfacial properties, thin layer of PVP was over-coated on the 7 wt % TiO_2-PVP nanocomposite. As shown in Table 4.1.1, the surface roughness was significantly reduced from 0.54 to 0.27 nm, and accordingly, the intensity of the XRD patterns and the grain size of pentacene increased; and these values were similar to those

of pristine PVP. As expected, the charge carrier mobility of pentacene with 7 wt % TiO_2-PVP/PVP nanocomposite increased from 0.184 to 0.220 cm^2/ Vs. A similar trend was also observed in the on/off ratio values (Table 4.1.3). A lower value of the on/off ratio of an OTFT that contains a higher content of TiO_2 nanoparticles can be attributed to the smaller grain size of pentacene, which is induced by the surface roughness of nanocomposite dielectric layer. The threshold voltage (V_{th}) progressively reduced as the concentration of the TiO_2 nanoparticles in the PVP matrix increased. This is probably because of the enhancement of the dielectric constant with the increase in the concentration of TiO_2.[7, 21] In Figure 4.1.9, it can be seen that the output characteristics of OTFTs with different dielectrics corroborates well with the transfer characteristics.

Hysteresis in OTFTs is known to be a significant problem in device performance. The hydroxyl groups in dielectrics, in particular, are known to act as electron trap sites, leading to hysteresis. The amount of hysteresis is usually proportional to the amount of hydroxyl groups in the dielectric.[25, 36] It is well known that hysteresis in PVP-based dielectrics can be reduced by the cross-linker, PMF, because the hydroxyl groups of PVP are cross-linked with hydrogen, methyl or butyl groups of PMF during curing process.[37] As shown in Figure. 4.1.8, there was negligible amount of hysteresis in all the tested OTFTs, implying that only a small amount of hydroxyl groups was present in the dielectric layers. These results suggest that the polymer chains in PVP and the ligands on the TiO_2 nanoparticles cross-linked completely with PMF.

4.1.4 Conclusion

OTFT was successfully fabricated, which can operate at low voltages using nanocomposites as the gate dielectric material. These nanocomposite dielectrics (TiO_2-PVP) were made by grafting a PVP monomer–like ligand, 4-hydroxybenzoic acid, on 5 nm-sized TiO_2 nanoparticles in order to increase the interaction between TiO_2 and PVP. 4HBA-TiO_2 nanoparticles were homogeneously dispersed in the PVP matrix without any aggregation or phase separation of the nanoparticles, even when 31 wt % of TiO_2 was added. OTFTs with TiO_2-PVP nanocomposite dielectrics exhibited low leakage currents and negligible hysteresis. The dielectric constant of the nanocomposites increased with an increase in the content of TiO_2, and this further allowed the operation of OTFTs at a low voltage such as -5 V. In addition, OTFTs with TiO_2-PVP dielectrics showed better performance, such as higher mobility, on/off ratio, and threshold voltage than OTFTs with pristine PVP dielectric. However, for OTFTs with nanocomposites having a TiO_2 concentration above 14 wt %, the device performances deteriorated owing to increased surface roughness. This problem was overcome by an over-coat of a thin layer of PVP on 7 wt % TiO_2-PVP nanocomposites, leading to an enhanced field-effect mobility value of 0.220 cm^2 /Vs, among others. In summary, our method enables OTFTs to be applied to various applications.

Chapter 4

Part 2. $BaTiO_3$-PVP Nanocomposite Dielectrics for Organic Thin Film Transistors

4.2.1 Introduction

PVP nanocomposite dielectric with barium titanate ($BaTiO_3$) have also fabricated followed by the same experiments of TiO_2-PVP nanocomposites. $BaTiO_3$ normally exhibits a ferroelectric phase in single-crystal form. However, $BaTiO_3$ exhibits dielectric with a high dielectric constant when $BaTiO_3$ is nanocrystalline.[20, 38] 6 nm sized $BaTiO_3$ were obtained using a two-phase reaction. The ligand exchange reaction was performed by using 4-hydroxybenzoic acid which is similar in structure to the repeat unit in PVP. 4HBA-$BaTiO_3$ was well dispersed up to 14 wt% without no considerable aggregation, as observed by TEM. Even though, the relationship between dielectric constant the dielectric constant of $BaTiO_3$-PVP nanocomposite and concentration of $BaTiO_3$ in PVP weren't found, dielectric constant of $BaTiO_3$-PVP nanocomposites increased compared to that of pristine PVP.

4.2.2 Experimental Section

Barium acetate, Titanium (IV) *n*-propoxide, toluene, oleic acid, *t*-butylamine, pentacene, 4-hydroxybenzoic acid (4HBA), poly (4-vinylphenol) (PVP, Mw = 25,000), poly(melamine-co-formaldehyde) methylated/butylated (PMF) were purchased from Aldrich. Acetone, tetrahydrofuran (THF), isopropyl alcohol, and chloroform were purchased from Samchun Chemical Co. Ethanol was purchased from J. T. Baker. All organic solvents were reagent grade and used without further purification.

Synthesis of $BaTiO_3$ nanoparticles

$BaTiO_3$ nanoparticles were obtained using a two-phase thermal synthesis method.[39] 0.09 g of Barium acetate was added to 1.0 mL of oleic acid and heated to 180 °C for 30 min with vigorously stirring. After cooling to room temperature, 0.1 mL of titanium (IV) *n*-propoxide dissolved in 5 mL of toluene and 0.05 mL of *t*-butylamine in 10 mL of water were added, and then the final solution was transferred to the autoclave. The autoclave was sealed and heated to 180 °C for 12 h without any stirring of its contents and cooled to room temperature. The reaction solution precipitated with ethanol and the precipitate was centrifuged for 10 min at 4,000 rpm. The precipitate was redispersed in a small amount (~3 mL) of chloroform with vortexing and then reprecipitated with ethanol. This precipitation/redispersion procedure was repeated twice. The dispersion of $BaTiO_3$ nanoparticles in chloroform was centrifuged at 4,000 rpm for 10 min to remove any aggregated particles. A white colored supernatant, which was a dispersion of oleic acid-stabilized $BaTiO_2$ nanoparticles (OA-$BaTiO_3$), was collected for the next step.

A solution of 4-hydroxybenzoic acid (2 g of 4HBA in 20 mL of THF) was

added drop by drop to a dispersion of OA-$BaTiO_3$ (200 mg OA-$BaTiO_3$ in 20 mL of chloroform). The mixture was stirred at 60 °C for 24 h and then cooled to room temperature. 4HBA-modified $BaTiO_3$ nanoparticles were precipitated by adding a large excess of chloroform followed by centrifugation for 10 min at 4,000 rpm. The precipitate was redispersed in a small amount (~3 mL) of ethanol with vortexing and then reprecipitated with chloroform. This precipitation/redispersion procedure was repeated twice. The dispersion of 4HBA-modified $BaTiO_3$ nanoparticles in ethanol was centrifuged at 4,000 rpm for 10 min to remove any aggregated particles, and the yellow colored supernatant (4HBA- $BaTiO_3$) was collected for the next step.

Preparation of $BaTiO_3$-PVP nanocomposite solutions

PVP and PMF (2:1 wt. ratio) were added to an appropriate amount of 4HBA-$BaTiO_3$, and the mixture was stirred vigorously at room temperature for one day. Three different solutions, which could produce 3, 7 and 14 wt % of $BaTiO_3$ in nanocomposite films, respectively, were prepared by varying the amount of 4HBA-$BaTiO_3$ nanoparticles.

Characterization

Transmission electron microscopy (TEM) images were acquired using a microscope (Hitachi-7600) operating at 100 kV. The capacitance of the dielectric nanocomposites was measured using an Agilent 4284A 1 kHz precision inductance-capacitance-resistance (LCR) meter. All electrical characterizations of the OTFTs were carried out at ambient conditions and a dark environment. The thickness of the dielectric nanocomposites was measured using K-MAC, ST2000-DLXn instrument.

4.2.3 Results and Discussion

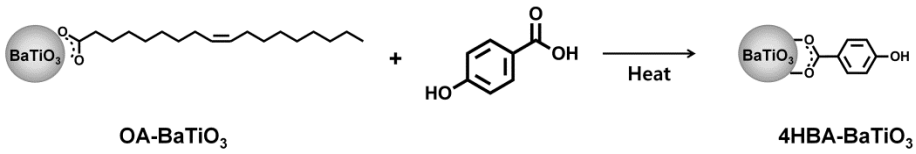

OA-$BaTiO_3$ 4HBA-$BaTiO_3$

Scheme 4.2.1. Ligand exchange reaction of $BaTiO_3$ with 4-hydroxybenzoic acid.

As prepared $BaTiO_3$ with 6 nm-size were dispersed in chloroform due to oleic acid on the surface (Figure 4.2.1a). To increase compatibility between $BaTiO_3$ and PVP, ligand exchange reaction with 4-hyrodoxybenzoic acid which has a structure similar to that of PVP was performed by reacting OA-$BaTiO_3$ with excess amount of 4-hyrodoxybenzoic acid in mixture of chloroform and THF. Figure 4.2.1b indicated that 4-hyrodoxybenzoic acid modified $BaTiO_3$ (4HBA-$BaTiO_3$) were well dispersed in EtOH, appropriate solvent for PVP.

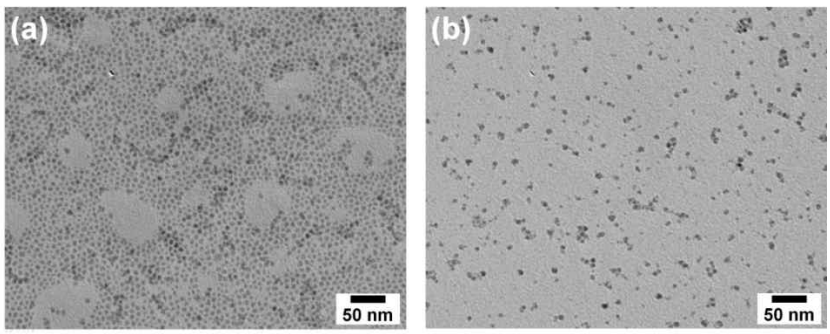

Figure 4.2.1. TEM images of (a) OA-$BaTiO_3$ and (b) 4HBA-$BaTiO_3$.

4HBA-$BaTiO_3$ dispersed in ethanol were mixed with PVP and PMF and then vigorously stirring the mixture for a day. The TEM images of $BaTiO_3$-PVP nanocomposite with varying amount of $BaTiO_3$ are presented in Figure 4.2.2. No significant aggregation of $BaTiO_3$ nanoparticles were found in all nanocomposite, indicating the compatibility between surface of $BaTiO_3$ and PVP enhanced due to the ligand.

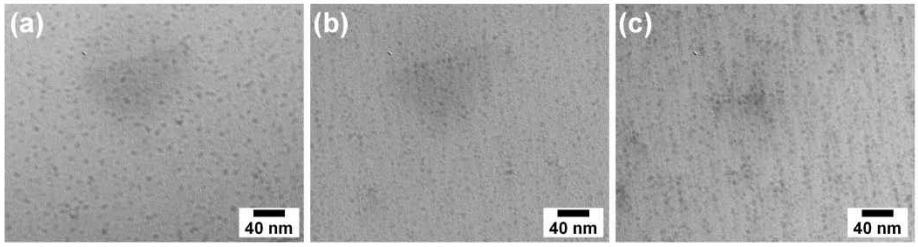

Figure 4.2.2. TEM images of $BaTiO_3$-PVP nanocomposites having: (a) 3, (b) 7 and (c) 14wt% of $BaTiO_3$ in PVP. The TEM images were obtained by spin-coating $BaTiO_3$-PVP nanocomposite solutions onto a TEM grid, followed by curing at 200 ℃ for 1 h.

Table 4.2.1. Dielectric constants of PVP and $BaTiO_3$-PVP nanocomposites.

	Thickness	Dielectric constant, k
PVP	209	3.43
3 wt% $BaTiO_3$–PVP	224	4.96
7 wt% $BaTiO_3$–PVP	247	4.23
14 wt% $BaTiO_3$–PVP	281	4.96

The dielectric properties of the nanocomposite with varying amount of $BaTiO_3$ are summarized in Table 4.2.1. The dielectric constant of pristine PVP and nanocomposite dielectrics with 4, 7 and 14 wt% $BaTiO_3$ are 3.43, 4.96,

4.23 and 4.98, respectively. Although the dielectric constant of $BaTiO_3$-PVP nanocomposites is not proportional concentration of $BaTiO_3$, the enhancement of dielectric constant of $BaTiO_3$-PVP nanocomposites was observed in all nanocomposite dielectrics compared to that of pristine PVP. The enhanced dielectric constant is attributed to relatively higher dielectric constant of $BaTiO_3$ compared to the PVP.

4.2.4 Conclusion

6 nm-sized $BaTiO_3$ was incorporated in PVP to generate high-k nanomcomposite dielectrics. The surface ligand of $BaTiO_3$ was exchanged with 4-hydroxybenzoic acid to enhance interaction between $BaTiO_3$ and PVP. As a result, $BaTiO_3$ were well dispersed in PVP without generating aggregation up to 14wt%. Although the dependence of the dielectric constant and concentration of $BaTiO_3$ was not demonstrated, $BaTiO_3$-PVP nanocomposites have higher dielectric constant compared with that of PVP.

Acknowledgements

I would like to thank Joohee Kim and Prof. Youn Sang Kim for helping with fabrication and characterization of OTFT devices.

References

[1] Forrest, S. R., *Nature* **2004,** *428*, 911-918.

[2] Gelinck, G. H.; Huitema, H. E. A.; Van Veenendaal, E.; Cantatore, E.; Schrijnemakers, L.; Van der Putten, J. B. P. H.; Geuns, T. C. T.; Beenhakkers, M.; Giesbers, J. B.; Huisman, B. H.; Meijer, E. J.; Benito, E. M.; Touwslager, F. J.; Marsman, A. W.; Van Rens, B. J. E.; De Leeuw, D. M., *Nature Mater.* **2004,** *3*, 106-110.

[3] Puigdollers, J.; Voz, C.; Orpella, A.; Quidant, R.; Martin, I.; Vetter, M.; Alcubilla, R., *Org. Electron.* **2004,** *5*, 67-71.

[4] Ortiz, R. P.; Facchetti, A.; Marks, T. J., *Chem. Rev.* **2010,** *110*, 205-239.

[5] Majewski, L. A.; Schroeder, R.; Grell, M., *Adv. Funct. Mater.* **2005,** *15*, 1017-1022.

[6] Yan, H.; Chen, Z. H.; Zheng, Y.; Newman, C.; Quinn, J. R.; Dotz, F.; Kastler, M.; Facchetti, A., *Nature* **2009,** *457*, 679-U1.

[7] Lee, W. H.; Wang, C. C.; Chen, W. T.; Ho, J. C., *Jpn. J. Appl. Phys.* **2008,** *47*, 8955-8960.

[8] Veres, J.; Ogier, S.; Lloyd, G.; de Leeuw, D., *Chem. Mater.* **2004,** *16*, 4543-4555.

[9] Lee, W. H.; Wang, C. C.; Ho, J. C., *J. Vac. Sci. Technol. B* **2009,** *27*, 601-605.

[10] Chen, F. C.; Chu, C. W.; He, J.; Yang, Y.; Lin, J. L., *Appl. Phys. Lett.* **2004,** *85*, 3295-3297.

[11] Wang, J. J.; Lee, W. H.; Ho, J. C.; Hu, T. S., *J. Mater. Sci-Mater. El.* **2009,** *20*, 355-358.

[12] Wang, G.; Moses, D.; Heeger, A. J.; Zhang, H.-M.; Narasimhan, M.; Demaray, R. E., *J. App. Phys.* **2004,** *95*, 316-322.

[13] Kumazawa, H.; Masuda, K., *Thin Solid Films* **1999,** *353*, 144-148.

[14] Tardy, J.; Erouel, M.; Deman, A. L.; Gagnaire, A.; Teodorescu, V.; Blanchin, M. G.; Canut, B.; Barau, A.; Zaharescu, M., *Microelectron. Reliab.* **2007,** *47*, 372-377.

[15] Shen, Y.; Lin, Y. H.; Li, M.; Nan, C. W., *Adv. Mater.* **2007,** *19*, 1418-1422.

[16] Shen, Y.; Lin, Y. H.; Nan, C. W., *Adv. Funct. Mater.* **2007,** *17*, 2405-2410.

[17] Liu, H. Y.; Shen, Y.; Song, Y.; Nan, C. W.; Lin, Y. H.; Yang, X. P., *Adv. Mater.* **2011,** *23*, 5104-5108.

[18] Kim, J. Y.; Lee, W. H.; Suk, J. W.; Potts, J. R.; Chou, H.; Kholmanov, I. N.; Piner, R. D.; Lee, J.; Akinwande, D.; Ruoff, R. S., *Adv. Mater.* **2013,** *25*, 2308-2313.

[19] Nan, C.-W.; Shen, Y.; Ma, J., *Annu. Rev. Mater. Res.* **2010,** *40*, 131-151.

[20] Schroeder, R.; Majewski, L. A.; Grell, M., *Adv. Mater.* **2005,** *17*, 1535-1539.

[21] Kim, P.; Zhang, X. H.; Domercq, B.; Jones, S. C.; Hotchkiss, P. J.; Marder, S. R.; Kippelen, B.; Perry, J. W., *Appl. Phys. Lett.* **2008,** *93*, 013302.

[22] Kim, Y. J.; Ha, S. W.; Jeon, S. M.; Yoo, D. W.; Chun, S. H.; Sohn, B. H.; Lee, J. K., *Langmuir* **2010,** *26*, 7555-60.

[23] Pan, D. C.; Zhao, N. N.; Wang, Q.; Jiang, S. C.; Ji, X. L.; An, L. J., *Adv. Mater.* **2005,** *17*, 1991-1995.

[24] Liu, Y.; Dadap, J. I.; Zimdars, D.; Eisenthal, K. B., *J. Phys. Chem. B* **1999,** *103*, 2480-2486.

[25] Park, J.; Bae, J. H.; Kim, W. H.; Kim, M. H.; Keum, C. M.; Lee, S. D.; Choi, J. S., *Materials* **2010,** *3*, 3614-3624.

[26] Zhang, M. H.; Tiwari, S. P.; Kippelen, B., *Org. Electron.* **2009,** *10*, 1133-1140.

[27] Albertin, K. F.; Valle, M. A.; Pereyra, I., *J. Intg. Cirts. Syst.* **2007,** *2*, 89-93.

[28] Goodman, G., *Ceramic Materials for Electronics*. Marcel Dekker: New York, **1991**.

[29] Jayasundere, N.; Smith, B. V., *J. App. Phys.* **1993,** *73*, 2462-2466.

[30] Yoon, D. H.; Zhang, J. P.; Lee, B. I., *Mater. Res. Bull.* **2003,** *38*, 765-772.

[31] Dang, Z. M.; Yuan, J. K.; Zha, J. W.; Zhou, T.; Li, S. T.; Hu, G. H., *Prog. Mater. Sci.* **2012,** *57*, 660-723.

[32] Bao, Z.; Locklin, J., In *Organic Field-Effect Transistors*, CRC Press: New York, **2007**, p 554.

[33] Fritz, S. E.; Kelley, T. W.; Frisbie, C. D., *J. Phys. Chem. B* **2005,** *109*, 10574-10577.

[34] Klauk, H.; Halik, M.; Zschieschang, U.; Schmid, G.; Radlik, W.; Weber, W., *J. App. Phys.* **2002,** *92*, 5259-5263.

[35] Lee, W. H.; Cho, J. H.; Cho, K., *J. Mater. Chem.* **2010,** *20*, 2549-2561.

[36] Choi, C. G.; Baez, B. S., *Electrochem. Solid-State Lett.* **2007,** *10*, H347-H350.

[37] Lim, S. C.; Kim, S. H.; Koo, J. B.; Lee, J. H.; Ku, C. H.; Yang, Y. S.; Zyung, T., *Appl. Phys. Lett.* **2007,** *90*, 173512.

[38] Shaw, T. M.; Trolier-McKinstry, S.; McIntyre, P. C., *Annu. Rev. Mater. Sci.* **2000,** *30*, 263-298.

[39] Zhao, N. N.; Nie, W.; Mao, J.; Yang, M. Q.; Wang, D. P.; Lin, Y. H.; Fan, Y. D.; Zhao, Z. L.; Wei, H.; Ji, X. L., *Small* **2010,** *6*, 2558-2565.

APPENDIX

Chapter 1. Cytop Nanocomposite Dielectrics

1.1 Introduction

Poly (perfluorobutenylvinylether), commercially known as Cytop (Asahi Glass Co.), is hydroxyl group free amorphous fluoropolymer. It has lower leakage current densities, and higher breakdown voltage than those of other polymer. In addition, negligible hysteresis was found in OTFTs with Cytop, because Cytop does not have hydroxyl group in molecule.[1] In general, hysteresis mainly induced by charge trapping of at hydroxyl group in insulator or interface between insulator and semiconductor.[2-3] Despite of these benefit, Cytop has low dielectric constant (k=2.1-2.2)[4], high gate voltage is need to operate OTFTs.

Here, Cytop nanocomposites with high dielectric inorganic filler were fabricated for enhancing dielectric constant of polymer. To obtain homogeneously disperse nanofiller/polymer composite, nanoparticles were modified by (3-trimethoxy-silylpropyl) diethylenetriamine (DETAS), and then react with 1,2-epoxy-1H,1H,2H,3H,3H-heptadecafluoroundecane to introduce a large number of fluorine on the surface of nanoparticles. Cytop nanocomposites without aggregation were successfully fabricated.

1.2 Experimental section

Tetraethyl orthosilicate (TEOS), 1,2-epoxy-1H,1H,2H,3H,3H-heptadecafluoroundecane and heptacosafluorotributylamine were purchased from TCI. Cytop solution from LG Display and (3-trimethoxysilylpropyl)diethylenetriamine (DETAS) from Gelest. Titanium (Ⅳ) ethoxide was purchased from Aldrich.

Synthesis of SiO_2

The synthetic method of 30 nm sized SiO_2 nanoparticlces is the same as describe in 2.3. Experimental section.

Synthesis of TiO_2

100 nm sized TiO_2 was received from Joohyun Lim. 1.7 mL of $Ti(OEt)_4$ and 0.4 mL of 0.32 M KCl were added to 100 mL of 1-propanol. The mixture stirred for 2h at room temperature. And then 60 mL of mixture was added to 500 mL of EtOH and stirred for 2h at room temperature. The TiO_2 suspension was centrifuge for 10 min at 20000 rpm. The precipitate was redispersed in EtOH, followed by centrifugation under the same conditions. This centrifugarion-redispersion procedure was repeated more than two times. TiO_2 dispersed in EtOH solution was collected for the next step.

Surface modification of SiO_2 and TiO_2

3.0 mL of DETAS was added to the dispersed SiO_2 solution (400 mg of SiO_2 nanoparticles in 40 mL of EtOH), and the mixed solution was stirred at room temperature for 12 h. The mixture was centrifuged for 20 min at 20000 rpm, and then, the precipitate was redispered in EtOH. This centrifugation-

redispersion procedure was repeated more than two times to obtain the dispersed solution of the DETAS-modified SiO_2 nanoparticles (DETAS-SiO_2). The DETAS modified TiO_2 nanoparticles (DETAS-TiO_2) was obtained as the same method.

Nanoparticles with a large number of fluorine on the surface were obtained in EtOH/heptacosafluorotributylamine two-phase reaction system. 0.2 mL of 1,2-epoxy-1H,1H,2H,3H,3H-heptadecafluoroundecane dissolved in 5 mL of heptacosafluorotributylamine was added to the solution of 128 mg DETAS-SiO_2 in 5 mL of EtOH. The mixture was refluxed with vigorous stirring for 12 h. After cooling to room temperature, the heptacosafluorotributylamine was separated and extracted with ethanol twice. To remove ethanol and excess amount of 1,2-epoxy-1H,1H,2H,3H,3H-heptadecafluoroundecane, the heptacosafluorotributylamine phase was heated to 90 ℃ with N_2 bubbling for an hour. Surface modified nanoparticle dispersed in heptacosafluoro tributylamine was obtained for the next step (F-SiO_2). F-TiO_2 dispersed in heptacosafluorotributylamine solution was obtained as the same method.

Preparation of Cytop nanocomposite solutions

Four different samples with 0.1, 0.3, 0.5 and 1.0 mg of the modified nanoparticles (F-SiO_2 or F-TiO_2) dispersed in heptacosafluorotributylamine solution were added to the 1 g of Cytop solution and stirred vigorously at room temperature for a day.

Characterization

Thermal gravimetric analysis (TGA) measurements were performed using an SDT Q600 apparatus (TA Instruments Inc.) by heating the samples from 30°C

to 600°C at a heating rate of 10°C/min under N_2. Transmission electron microscopy (TEM) images were acquired using a Hitachi-7600 TEM instrument operated at 100 kV.

1.3 Results and Discussion

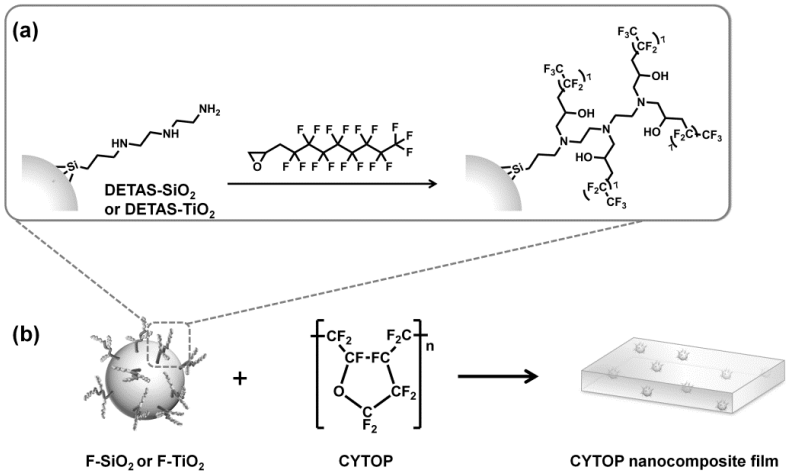

APPENDIX/Scheme 1.1. Schematic illustration of (a) the surface modification of silica nanoparticles by (3-trimethoxysilylpropyl) diethylenetriamine (DETAS) and the reaction between the suface amines and 1,2-epoxy-1H,1H,2H,3H,3H-heptadecafluoroundecane and (b) the preparation of SiO_2-Cytop (TiO_2-Cytop) nanocomposite.

Amorphous fluoropolymer (Cytop, Scheme 1.1b) is known to be very hydrophobic due to the nature of the fluorinated materials and insoluble in general organic solvent such as $CHCl_3$, THF, DMSO and alcohol but in fluorinated solvent, heptacosafluorotributylamine. Since as prepared SiO_2 and TiO_2 nanoparticles are hydrophilic and CYTOP is hydrophobic, surface modification is needed to increase compatibility between nanoparticles and polymer. To introduce a ligand which has a large number of fluorine on the surface of nanoparticles, amine groups were introduced in the nanoparticles surface by attaching DETAS to the surface of SiO_2 and TiO_2 to generate DETAS-SiO_2 (DETAS-TiO_2).[5] And then, the DETAS modified nanoparticles were reacted with 1,2-epoxy-1H,1H,2H,3H,3H-heptadecafluoroundecane, the

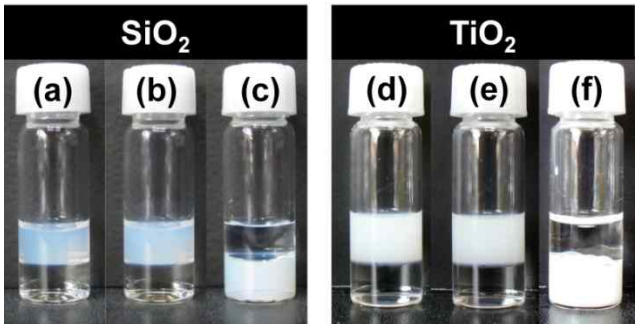

APPENDIX/Figure 1.1. Photographs of nanoparticle dispersions: the upper solvent is ethanol and the lower solvent is heptacosafluorotributylamine. (a) Bare SiO_2, (b) DETAS-SiO_2, (c) F-SiO_2, (d) bare TiO_2, (e) DETAS-TiO_2 and (f) F-TiO_2.

reaction involve ring opening of epoxide *via* nucleophilic attack of amine group of DETAS with the least hindered end of the epoxide in 1,2-epoxy-1H,1H,2H,3H,3H-heptadecafluoroundecane (Scheme 1.1a). Since Cytop is soluble in heptacosafluorotributylamine, the modified nanoparticles must be dispersed in heptacosafluorotributylamine in order to fabricate homogeneously fabricated Cytop nanocmposites. Therefore, the reaction was carried out in two phase reaction because EtOH and heptacosafluorotributylamine are unmixable. In addition, DETAS modified nanoparticles are well dispersed in EtOH (Figure 1.1b, e), however 1,2-epoxy-1H,1H,2H,3H,3H-heptadecafluoroundecane was not dissolved in EtOH but in heptacosafluorotributylamine. The epoxide-amine reaction occurred at the interface of the ethanol and heptacosafluorotributylamine phases. After the reaction, modified nanoparticles migrated to heptacosafluorotributylamine phase from ethanol phase (Figure 1.1c, f). TEM images indicated that modified nanoparticles were well dispersed in heptacosafluorotributylamine due to the ligand on the surface (Figure 1.2c, f).

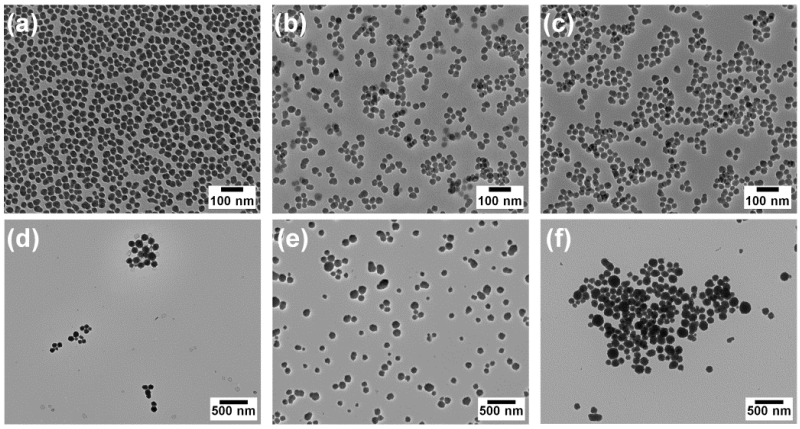

APPENDIX/Figure 1.2.TEM images of (a) bare SiO_2, (b) DETAS-SiO_2, (c) F-SiO_2, (d) bare TiO_2, (e) DETAS-TiO_2 and (f) F-TiO_2.

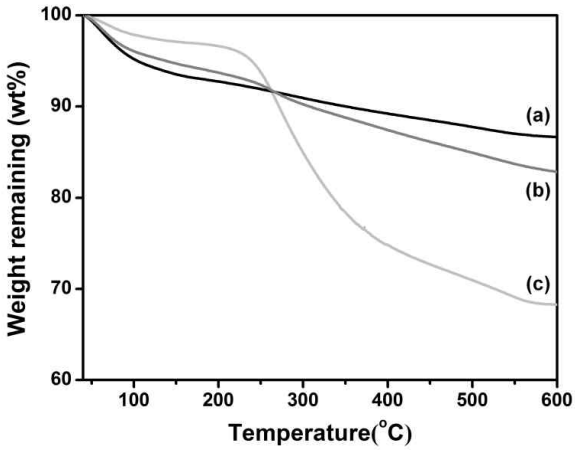

APPENDIX/Figure 1.3. TGA curves for (a) bare SiO_2, (b) DETAS-SiO_2 and (c) F-SiO_2.

After the modification, the surface of the SiO_2 nanoparticles was characterized by TGA. Figure 1.3, indicating weight losses of 17% and 32%, respectively, for the temperatures ranging from 30 to 600 ℃. An additional 15% weight loss seen in F-SiO_2 is attributed to the thermal degradation of fluorine compound binding with amine of DETAS.

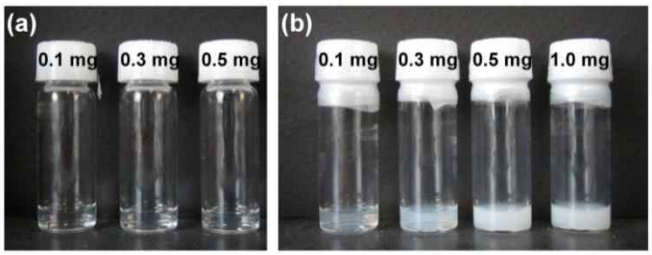

APPENDIX/Figure 1.4. (a) SiO_2-Cytop and (b) TiO_2-Cytop nanocomposite solutions with varying amount of nanoparticles.

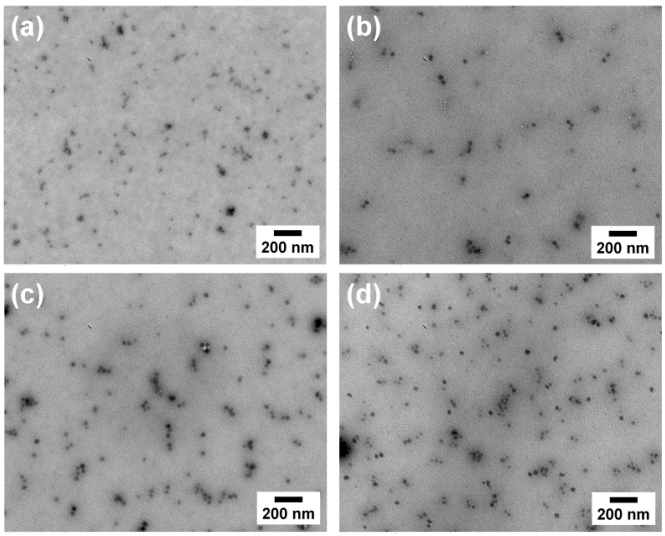

APPENDIX/Figure 1.5. TEM images of SiO_2-Cytop nanocomposites having: (a) 0.1, (b) 0.3, (c) 0.5 and (d) 1.0 mg of SiO_2 in 1 g of Cytop solution. The TEM images were obtained by spin-coating (900 rpm for 20 s) SiO_2-Cytop nanocomposite solutions onto a TEM grid, followed by curing at 130 °C for 1 h.

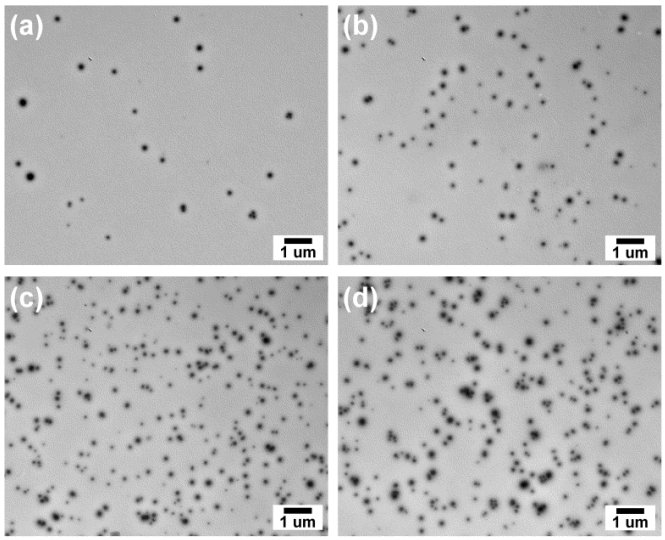

APPENDIX/Figure 1.6. TEM images of TiO_2-Cytop nanocomposites having: (a) 0.1, (b) 0.3, (c) 0.5 and (d) 1.0 mg of TiO_2 in 1 g of Cytop solution. The TEM images were obtained by spin-coating (900 rpm for 20 s) TiO_2-Cytop nanocomposite solutions onto a TEM grid, followed by curing at 130 °C for 1 h.

SiO_2-Cytop and TiO_2-Cytop nanocomposite solutions were prepared by mixing the Cytop solution with F-SiO_2 or F-TiO_2 nanoparticles dispersed in the heptacosafluorotributylamine. As shown in Figure 1.4, the F-SiO_2 and F-TiO_2 were well dispersed in the Cytop solution and no precipitation was found in any of the solution, even after few days. The TEM images of SiO_2- Cytop (Figure 1.5) and TiO_2-Cytop (Figure 1.6) nanocmopsites show that nanoparticles were homogeneously dispersed in the Cytop matrix and no significant aggregation was found in all samples. This result indicated that the chemical interaction between nanoparticles and polymer enhanced through a ligand on the surface of nanoparticles.

1.4 Conclusions

Cytop nanocmposites with high-*k* nanoparticles were successfully fabricated for the first time. To enhance compatibility between Cytop and nanoparticles, SiO_2 and TiO_2 nanoparticles were modified by simple two-step reaction: surface of nanoparticles were modified with (3-trimethoxy-silylpropyl) diethylenetriamine (DETAS), and then react with 1,2-epoxy-1H,1H,2H,3H,3H-heptadecafluoroundecane to introduce a large number of fluorine onto the surface. The modified nanoparticles were homogenously dispersed in the high fluorinated polymer, Cytop. It is expected that these Cytop nanocomposites is promising candidate for high-k dielectrics for OTFTs.

1.5 References

[1] Umeda, T.; Kumaki, D.; Tokito, S., *Org. Electron.* **2008,** *9*, 545-549.

[2] Park, J.; Bae, J. H.; Kim, W. H.; Kim, M. H.; Keum, C. M.; Lee, S. D.; Choi, J. S., *Materials* **2010,** *3*, 3614-3624.

[3] Choi, C. G.; Baez, B. S., *Electrochem. Solid-State Lett.* **2007,** *10*, H347-H350.

[4] Asahi Glass Company, Cytop amorphous fluoropolymer technical data sheet.

[5] Jung, H. S.; Moon, D. S.; Lee, J. K., *J. Nanomater.* **2012,** *2012*, 593471.

APPENDIX

Chapter 2. Au-PVP Nanocomposite Dielectrics

2.1 Introduction

Many researches have been studied to enhance dielectric constant of polymer by incorporating high-*k* ceramic nanoparitlces such as TiO_2, $BaTiO_3$ and ZrO_2.[1] In previous work, however, slight enhancement in dielectric constant of nanocomposite is obtained despite of the addition of a large amount of TiO_2[2]. Therefore, to obtain desired value of dielectric constant of nanocomposite dielectrics, high loading of the nanofiller is demanded. However, high loading of the nanofiller induces high-roughness on the dielectric surface and causes voids in polymer matrix, as a result dielectric properties of nanocomposites as well as the final OTFTs performance can be significantly degraded. In addition, high loading of the nanofiller deteriorates flexibility of the polymer nanocompsites[3].

On the other hand, conductive nanofiller such as metal nanoparticles overcome the limitation of ceramic-polymer nanocmpostie. Because conductive nanofiller induce interfacial polarization at the interface between nanofiller and polymer, as a result high-*k* nanocomposite can be achieved even at low loading.[4] Thus, specific surface area of conductive nanofiller significantly affects a dielectric constant of nanocomposites.[5] However, in these percolative composites, dielectric loss rapidly increases near the

percolative threshold. Therefore, preventing conductive nanofiller from connecting each other directly is a key for percolative nanocomposites dielectric to obtain high-*k* while retaining low dielectric loss.[6-7]

In here, Au-PVP nanocomposite is fabricated to obtain high-*k* nanocomposite without sacrificing the mechanical and dielectric properties of polymer at the same time. The compatibility between polymer and Au nanoparticles is increased by exchange of ligand on the Au surface by 4-hydroxythiophenol (4HTP), a ligand similar in structure to the repeat units in PVP. After ligand exchange, Au nanoparticles are homogenously dispersed in PVP matrix. It is expected that, Au-PVP nanocompsite may have high dielectric constant with low dielectric loss by improving interaction between surface of Au and PVP.

2.2 Experimental Section

Gold (III) chloride hydrate, dodecylamine, aqueous formaldehyde (37%), poly (4-vinylphenol) (PVP, Mw = 25,000) and poly(melamine-co-formaldehyde) methylated/butylated (PMF) were purchased from Aldrich. 4-Hydroxythiophenol was purchased from TCI. Acetone, tetrahydrofuran (THF), isopropyl alcohol, cyclohexane and chloroform were purchased from Samchun Chemical Co. Ethanol was purchased from J. T. Baker. All organic solvents were reagent grade and used without further purification.

Synthesis of Au nanoparticles

Au nanoparticles were obtained by two-phase synthesis.[8] 0.74 g of dodecylamine was dissolved in 25 mL of cyclohexane, and then 6 mL of aqueous formaldehyde (37%) was added. After stirring for 10 min at room temperature, the cyclohexane phase was separated and washed twice with distilled water. A solution of 40 mg of $HAuCl_4$ in 10 mL of water was added into the separated cyclohexane solution under vigorously stirring for 40 min at room temperature. The cyclohexane phased was separated and precipitated with ethanol and the precipitate was centrifuged for 10 min at 4,000 rpm. The precipitate was redispersed in a small amount of chloroform with vortexing and then reprecipitated with ethanol. This precipitation/redispersion procedure was repeated twice. A purple colored dodecylamine capped Au dispersed in chloroform was obtained (DA-Au).

A solution of 4-hydroxythiophenol (4HTP) dissolved in THF was added drop by drop to a dispersion of DA-Au. The mixture was stirred for 12 h at room temperature, the 4HTP-modified Au nanoparticles were precipitated by adding a large excess of chloroform followed by centrifugation for 10 min at

4,000 rpm. The precipitate was redispersed in a small amount of ethanol with vortexing and then reprecipitated with chloroform. This precipitation/redispersion procedure was repeated twice. The dispersion of 4HTP-modified Au nanoparticles in ethanol was centrifuged at 4,000 rpm for 10 min to remove any aggregated particles, and the 4HTP- Au was collected for the next step.

Preparation of Au-PVP nanocomposite solutions

PVP and PMF (2:1 wt. ratio) were added 4HTP-Au dispersed in ethanol solution and the mixture was stirred vigorously at room temperature for one day.

2.3 Results and Discussion

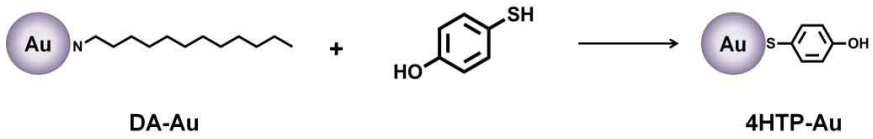

APPENDIX/Scheme 2.1. Ligand exchange reaction of Au nanoparticles with 4-hydroxythiophenol.

About 10 nm sized Au nanoparticle was obtained in water-cyclohexane two-phase system[8]. As prepared Au nanoparticles were well dispersed in chloroform due to the long alkane group, dodecyl amine, on the surface (Figure 2.1a). To obtain homogenous dispersion of Au in PVP matrix, ligand exchange with excess amount of 4-hydoxythiophenol (4HTP) was carried out (Scheme 2.1). 4-Hydroxythiophenol is suitable ligand for gold because thiol form stable and self-assembled monolayers on gold surface,[9-10] thus thiol is commonly used anchoring group to generate thiol-gold bond. In addition, 4-HTP on the gold surface can be cross-linked with PMF in a curing process. After surface modification, 4HTP-Au is well dispersed in EtOH with maintaining its shape and size (Figure 2.1b).

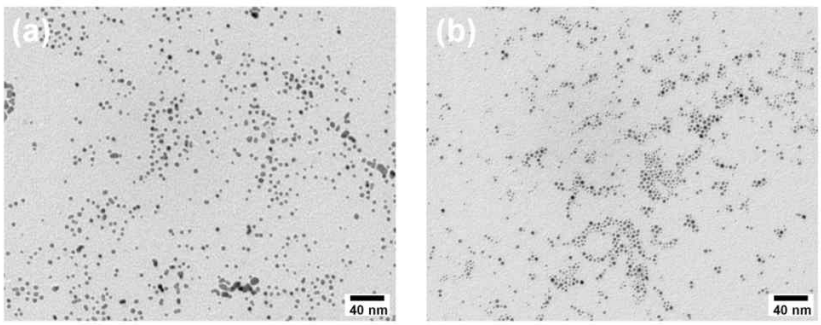

APPENDIX/Figure 2.1. TEM images of (a) DA-Au and (b) 4HTP-Au nanoparticles.

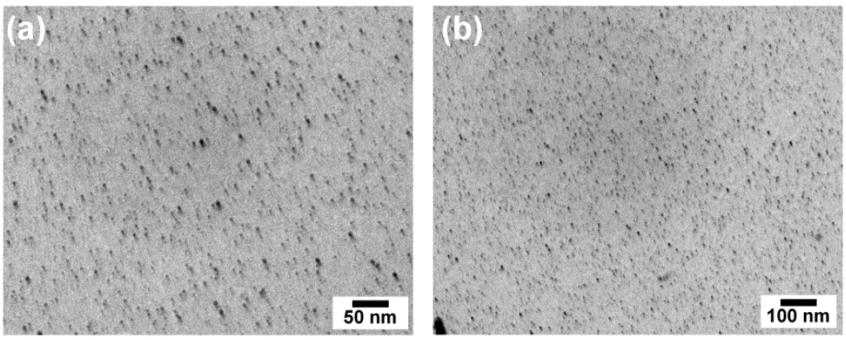

Figure 2.2. TEM images of Au-PVP nanocomposite (a) and (b) are in low and high magnification, respectively.

Au-PVP nanocomposite solution is obtained by directly mixing of 4HTP-Au dispersed in EtOH, PVP and PMF. Figure 2.2 shows the TEM images of Au-PVP nanocomposite prepared *via* spin-coating Au nanocomposite solutions onto a TEM grid, followed by curing at 200 ℃ for 1 h. It is clear that the gold nanoparticles are monodispersed in PVP matrix. This result indicated that the compatibility between gold and PVP improved by surface ligand exchange. It is expected that Au-PVP nanocomposite has high dielectric constant and low dielectric loss due to the homogenous dispersion of gold nanoparticles in the PVP and interfacial polarization induced by gold.

2.4 Conclusions

Au-PVP nanocomposite is successfully fabricated by surface modification of gold nanoparticles with 4-hydroxythiophenol. TEM images of Au-PVP nanocomposite indicated that interaction between Au and PVP is increased. High dielectric constant and low dielectric loss can be achieved due to the homogeneous dispersion of conductive nanofiller. In addition, it can be applied for charge trapping (or storage) layers in nano-floating gate memory devices due to charge trapping ability of gold nanoparticles.

2.5 References

[1] Ortiz, R. P.; Facchetti, A.; Marks, T. J., *Chem. Rev.* **2010,** *110*, 205-239.

[2] Kim, Y. J.; Kim, J.; Kim, Y. S.; Lee, J. K., *Org. Electron.* **2013,** *14*, 3406-3414.

[3] Nan, C.-W.; Shen, Y.; Ma, J., *Annu. Rev. Mater. Res.* **2010,** *40*, 131-151.

[4] Dang, Z. M.; Lin, Y. H.; Nan, C. W., *Adv. Mater.* **2003,** *15*, 1625-1629.

[5] Wang, B. H.; Liang, G. Z.; Jiao, Y. C.; Gu, A. J.; Liu, L. M.; Yuan, L.; Zhang, W., *Carbon* **2013,** *54*, 224-233.

[6] Shen, Y.; Lin, Y. H.; Li, M.; Nan, C. W., *Adv. Mater.* **2007,** *19*, 1418-1422.

[7] Huang, C.; Zhang, Q. M.; deBotton, G.; Bhattacharya, K., *Appl. Phys. Lett.* **2004,** *84*, 4391-4393.

[8] Chen, Y.; Wang, X., *Mater. Lett.* **2008,** *62*, 2215-2218.

[9] Neouze, M.-A.; Schubert, U., *Monatsh. Chem. Chem. Mon.* **2008,** *139*, 183-195.

[10] Leff, D. V.; Ohara, P. C.; Heath, J. R.; Gelbart, W. M., *J. Phys. Chem.* **1995,** *99*, 7036-7041.

APPENDIX

Chapter 3. High-sensitivity fluorescence imaging of iron in plant tissues

3.1 Introduction

Iron is a vital micronutrient that plays a critical role in a wide range of fundamental biological reactions in plants, such as electron transport chains in photosynthesis, respiration, cell division, and nitrogen fixation.[1] The versatile roles of iron arise from its chemical property: it exists in two alternative oxidation states, ferric ion (Fe^{3+}) and ferrous ion (Fe^{2+}). However, the dual oxidation characteristic of iron potentiates oxygen toxicity by generating reactive oxygen species, which cause oxidative damage to biomolecules. Therefore, plants tightly maintain iron homeostasis through coordinated regulation of its uptake, transport, and storage.[2]

The physiological roles of iron have been explored by molecular genetics and biochemical studies of mutant plants exhibiting defects in iron metabolism and by measurements of iron contents via inductively coupled plasma mass spectrometry.[3] In recent years, there has been a growing concern for high-resolution imaging of iron distribution in plant tissues, which is a prerequisite for understanding the dynamic iron metabolic processes in plant

growth and development and environmental stress responses. X-ray fluorescence microtomography and electron microscopy coupled to inelastically scattered electrons have been adopted for investigating the specific localization of iron in plants.[4-5] However, because of technical difficulties associated with these methods, histochemical staining methods, such as Perls staining,[6] are still routinely used. Although the Perls staining method has been improved,[7-9] a major sink of iron in plants, the leaves, is poorly stained by histochemical methods, and the resolution of iron detection remains poor. The experimental procedures involved are also complex and time-consuming.

An array of fluorescent probes has been developed for imaging of diverse biomolecules in plants and animals. Unlike absorbance-based probes for iron detection, such as the blue precipitate of Perls staining and the black precipitate of DAB-intensified Perls (Perls/DAB) staining, fluorescence-based sensors are highly sensitive, providing nearly infinite contrast by emitting light on a dark background. In addition to visualization of specific biomolecules with high sensitivity, detection by fluorescent probes is simple, precise, and quantitative. Recently, several fluorescent probes have been synthesized for the detection of iron in cells.[10-14] However, these have not yet been tested for their application in plant tissues.

When considering fluorescent probes that may be appropriate for selective detection of iron in plant tissues, MPNBD (7-(4-methylpiperazin-1-yl)-4-nitrobenz-2-oxa-1,3-diazole) is chosen as a photoinduced electron transfer (PET) fluoroionophore for the evaluation of its potential application in plants (Scheme 1),[10, 15-16] based on the following reasons. First, MPNBD displays high fluorescence enhancement in the presence of physiological concentrations of Fe^{3+} with low background emission. Second, chelation of

Fe^{3+} by MPNBD induces emission in the green region, which is easily distinguishable from red autofluorescence in plants. In addition, it is efficiently excited by wavelengths above 430 nm, thus avoiding cellular and tissue damage.

In here, a method for high-sensitivity fluorescence imaging of iron developed, which demonstrates the abundance and distribution of iron in plant tissues more precisely than conventional histochemical staining procedures. The fluorescence turn-on method is rapid (< 20 min), inexpensive to set up, and expected to be readily applicable to animal tissues.

3.2 Experimental section

Chloroform, 4-chloro-7-nitrobenzofurazan, 1-methylpiperazine, iron (Ⅲ) chloride hexahydrate, iron (Ⅱ) chloride tetrahydrate, magnesium chloride hexahydrate, manganese chloride tetrahydrate, zinc chloride, copper chloride dehydrate, and chromium (Ⅲ) chloride hexahydrate were purchased from Aldrich. Potassium chloride, sodium chloride, and calcium chloride were Samchum Chemical Co. Nickel chloride is purchased from Oriental Chemical Industry. Ethanol was purchased from J.T.Baker.

Synthesis of 7-(4-methylpiperazin-1-yl)-4-nitrobenzo-2-oxa-1,3-diazole (MPNBD)

MPNBD was prepared following the procedure that has been described previously,[10] but with some modifications. 4-chloro-7-nitrobenzofurazan (0.5 g, 2.5 mmol) was dissolved in $CHCl_3$ (20 mL). 1-methylpiperazine (0.28 mL, 2.5 mmol) was added and stirred for 30 min at room temperature. The reaction mixture was concentrated on a rotary evaporator. The residue was purified by column chromatography (SiO_2, eluent: CH_2Cl_2/MeOH = 10/1) to afford 0.43 g of orange powder in 66% yield. ^{1}H- and ^{13}C-NMR spectra were measured on a Varian NMR System 500 MHz NMR Spectrometer (Varian, Palo Alto, CA). Data were acquired as follows; chemical shifts in ppm from tetramethylsilane as an internal standard in $CDCl_3$, integration, multiplicity (s = singlet, d = doublet, t = triplet). ^{1}H-NMR (500 MHz, $CDCl_3$): δ ppm 2.32 (s, 3H), 2.61 (t, 4H), 4.06 (t, 4H), 6.25 (d, 1H), 8.35(d, 1H). ^{13}C-NMR (500 MHz, $CDCl_3$): δ ppm 145.18, 144.83, 144.78, 135.10, 123.54, 102.42, 54.55, 49.35, 45.84. HR-MS(FAB+) calculated for 264.1097 m/z, observed for 264.1097 m/z

Metal ion sensing by MPNBD

A stock solution of MPNBD (14.81 μM) and metal solutions of $FeCl_3 \cdot 6H_2O$ (4.51 mM), $FeCl_2 \cdot 4H_2O$ (5.90 mM), $CuCl_2 \cdot 2H_2O$ (7.10 mM), $CrCl_3 \cdot 6H_2O$ (4.24 mM), $CaCl_2$ (6.53 mM), $MgCl_2 \cdot 6H_2O$ (6.70 mM), $MnCl_2 \cdot 4H_2O$ (3.48 mM), $NiCl_2$ (4.65 mM), and $ZnCl_2$ (4.81 mM) were prepared in ethanol. Metal solutions of KCl (4.60 mM) and NaCl (6.55 mM) were prepared in water. Two mL of the MPNBD stock solution and each of metal ion stock solutions were mixed. Ethanol was then added to each mixture to match the concentration of MPNBD in each mixture to 9.88 μM. The mixtures were analyzed by UV-Vis spectroscopy (Sinco, S-3100, Seoul, Korea) and fluorophotometry (JASCO, FP-6500, Tokyo, Japan) at room temperature. Light source for fluorophotometry was the 150W Xenon lamp with a diffraction grating to select the excitation light. The emission spectra were measured in the wavelength range from 490 to 750 nm under the excitation at 470 nm.

Plant materials and growth conditions

Arabidopsis thaliana ecotype Columbia-0 (Col-0) was used. The *Arabidopsis* plants were grown on 1/2 X Murashige & Skoog (MS) media containing 0.6% (w/v) agar (hereafter referred to as MS-agar plate) in growth chamber at 22°C with white light illumination (120 μmol photons $m^{-2}s^{-1}$) provided by fluorescent FLR40D/A tubes (Osram, Seoul, Korea) under long day conditions (16-hour light and 8-hour dark).

Staining of iron in *Arabidopsis* plants

Four-day-old *Arabidopsis* plants grown on MS-agar plates were used. The

Perls and Perls/DAB (3,3'-diaminobenzidine) staining procedures were conducted as described previously.[14, 17] For the Perls staining, plants were vacuum infiltrated with a solution containing equal volumes of 4% (v/v) HCl and 4% (w/v) $K_4Fe(CN)_6$ for 15 minutes and subsequently incubated for 30 minutes in complete darkness at room temperature. For the DAB-intensified Perls staining, the Perls-stained plants were washed with distillated water, incubated in a methanol solution containing 0.01 M NaN_3 and 0.3% (v/v) H_2O_2 for 1 hour, and then washed with 0.1 M phosphate buffer (pH 7.4). For the DAB intensification, the plants were incubated for 10 to 30 minutes in 0.1 M phosphate buffer (pH 7.4) containing 0.0025% (w/v) DAB, 0.005% (v/v) H_2O_2, and 0.005% (w/v) $CoCl_2 \cdot 6H_2O$.

For fluorescence imaging of iron with MPNBD, four-day-old *Arabidopsis* plants were briefly washed with ethanol and vacuum infiltrated with a ethanol solution containing 50 μM MPNBD for 5 minutes. The plants were incubated in complete darkness for 10 minutes and washed with ethanol before fluorescence microscopy.

Fluorescence microscopy

Plants stained by the Perls and Perls/DAB methods were analyzed using the Olympus BX51 microscope (Olympus, Tokyo, Japan). Images were acquired using the Olympus DP70 digital camera system and processed with the DPController and DP Manager softwares (Olympus). For fluorescence detection in the MPNBD-treated plants, the U-MWB2 fluorescence detection system (excitation filter BP460-490, dichronic mirror DM500, and barrier filter BA520IF) (Olympus) was used. Light was provided by a 100W High Pressure Mercury Burner (Olympus, BH2-RFL-T3). Fluorescence images

were taken with an exposure time of 250 ms at 40X magnification. High-magnification images were visualized using the Zeiss LSM510 confocal microscope (Carl Zeiss, Jena, Germany) with the following filter setup: excitation 488 nm, emission BP510-530 nm. Fluorescence images were analyzed using the ImageJ software (http://rsbweb.nih.gov/ij/), as described previously.[14, 17]

3.3 Results and Discussion

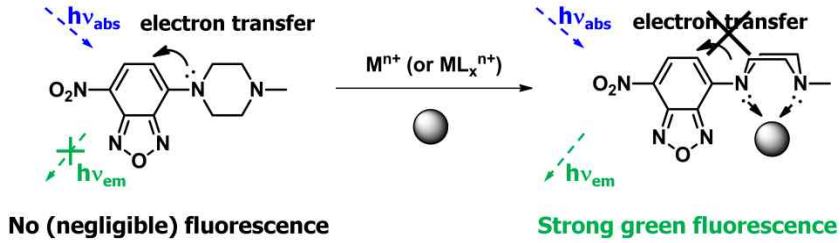

APPENDIX/Scheme 3.1. Chemical structure of MPNBD and its photoinduced electron transfer (PET) fluoroionophore mechanism. M, metal ion; n, oxidation number; L, solvent or other ligand molecule.

MPNBD was synthesized according to a previously described procedure,[10] and the purity and structural integrity of the synthesized MPNBD were verified by NMR spectra and mass spectrometry. To establish proper detection conditions, the absorption and emission spectra of MPNBD in water and ethanol along with the various amounts of Fe^{3+} was investigated. In ethanol, MPNBD showed a higher fluorescence response to Fe^{3+} in comparison to that observed for MPNBD in water (Figure 3.1), supporting the relevance of ethanol as the solvent of choice for MPNBD. It is well known that ethanol is compatible with most histological assays on plant tissues. Therefore, detection test were performed in ethanol-based condition

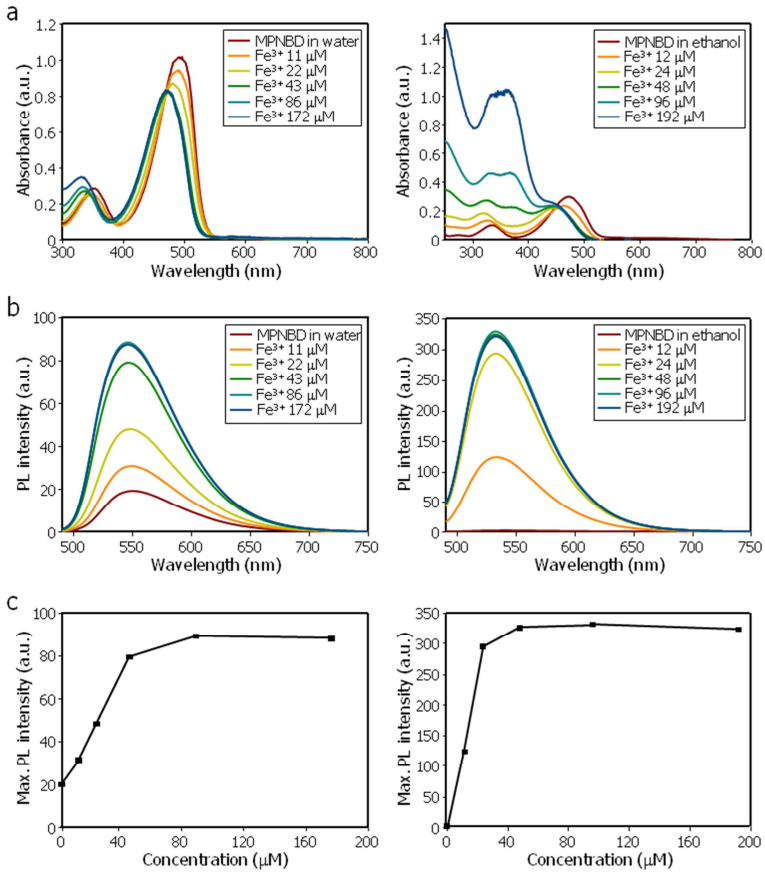

APPENDIX/Figure 3.1. Comparison of fluorescence responses of MPNBD in water (42.2 μM) and ethanol (11.8 μM) to various amounts of Fe^{3+}. (a) Changes in absorption spectra of MPNBD upon gradual addition of Fe^{3+} in water (left) and ethanol (right). (b) Changes in fluorescence spectra of MPNBD upon gradual addition of Fe^{3+} in water (left) and ethanol (right) under irradiation at 470 nm. (c) Fluorescence responses of MPNBD to different concentrations of Fe^{3+} in water (left) and ethanol (right). The excitation wavelength was 470 nm and the monitored maximum photoluminescence (PL) emission wavelengths were 548 nm (in water) and 533 nm (in ethanol), respectively, which are clearly shown in (b). a.u., arbitrary unit.

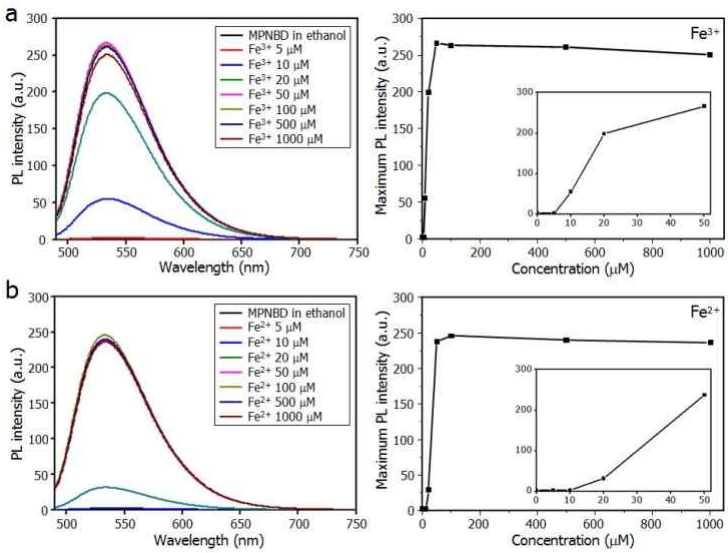

APPENDIX/Figure 3.2. Fluorescence response of MPNBD to (a) Fe^{3+} and (b) Fe^{2+} ions. Different concentrations of iron ions were added to MPNBD solution in ethanol, and the mixtures were subject to UV-vis spectroscopy and fluorophotometry. Fluorescence spectra under the irradiation at 470 nm are shown in the left panels. Plots of maximum photoluminescence (PL) emission intensity at 533 nm are shown in the right panels. The insets show plots of maximum PL intensities in the concentration range of 0 to 50 μM for Fe^{3+} or Fe^{2+}. a.u., arbitrary unit.

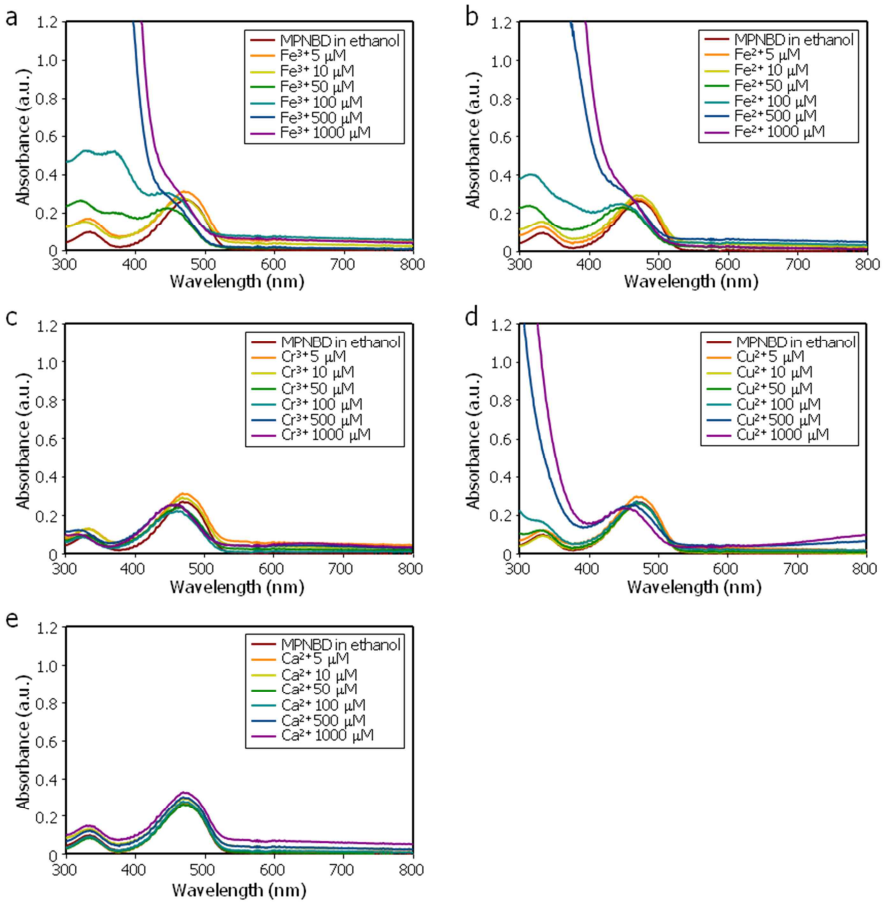

APPENDIX/Figure 3.3. Absorption spectra of MPNBD (9.88 μM) in the presence of Fe^{3+}, Fe^{2+}, Cr^{3+}, Cu^{2+}, and Ca^{2+}. Changes of absorption spectra of MPNBD upon gradual addition (0 to 1000 μM) of (a) Fe^{3+}, (b) Fe^{2+}, (c) Cr^{3+}, (d) Cu^{2+}, and (e) Ca^{2+} in ethanol were examined. a.u., arbitrary unit.

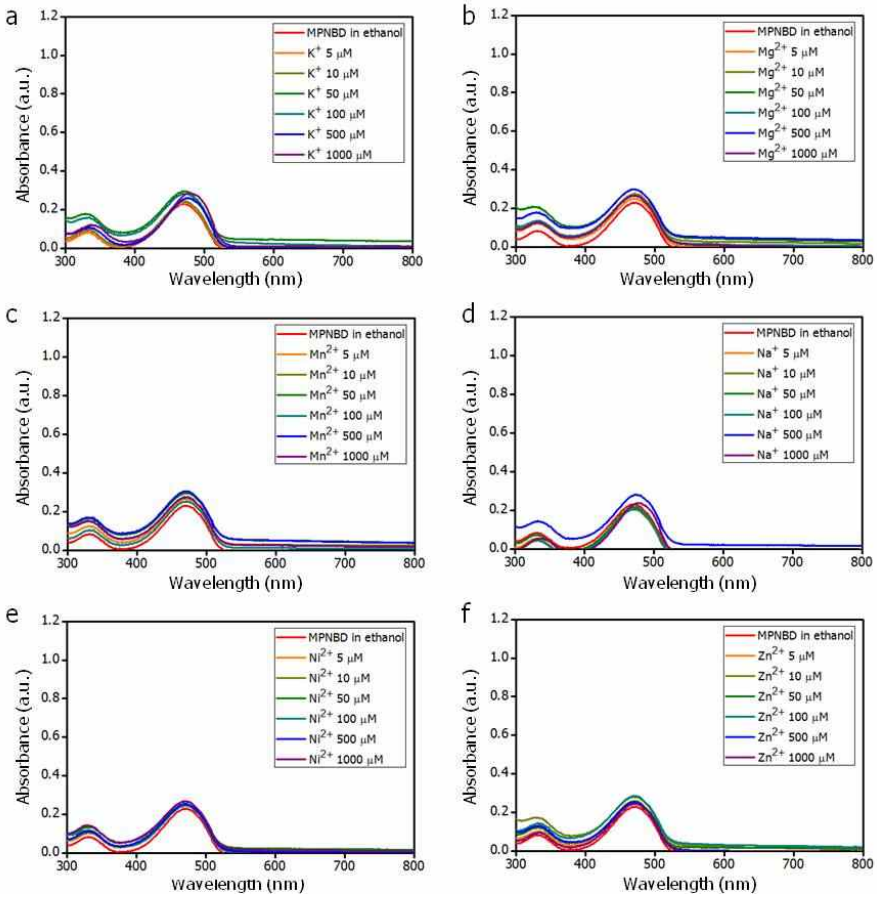

APPENDIX/Figure 3.4. Absorption spectra of MPNBD (9.88 μM) in the presence of K^+, Mg^{2+}, Mn^{2+}, Na^+, Ni^{2+}, and Zn^{2+}. Changes of absorption spectra of MPNBD upon gradual addition (0 to 1000 μM) of (a) K^+, (b) Mg^{2+}, (c) Mn^{2+}, (d) Na^+, (e) Ni^{2+}, and (f) Zn^{2+} in ethanol were examined. a.u., arbitrary unit.

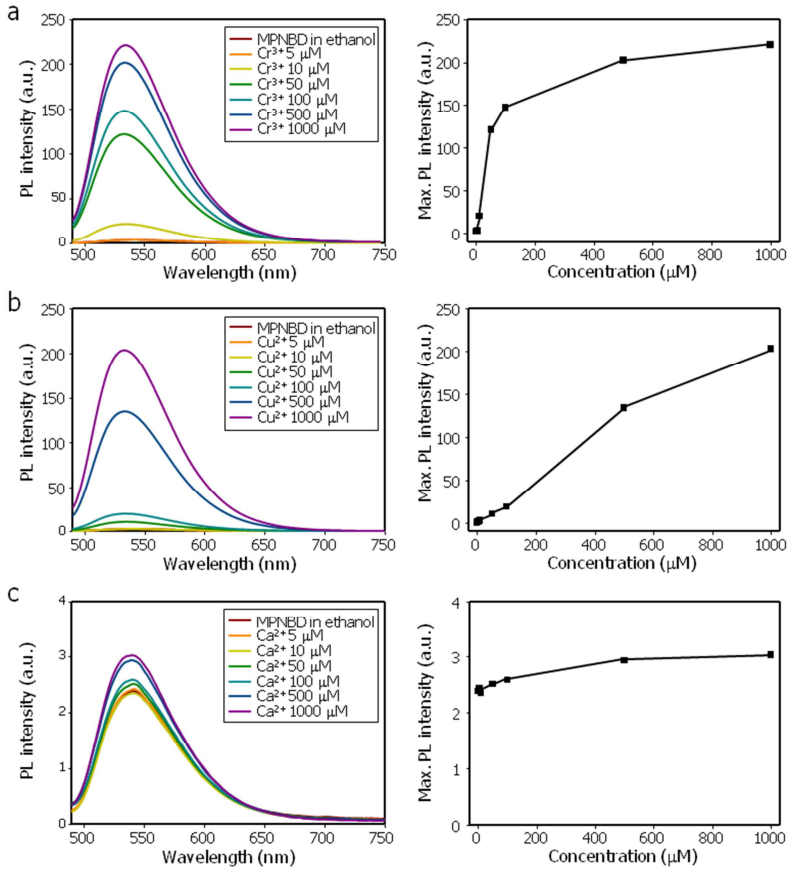

APPENDIX/Figure 3.5. Fluorescence responses of MPNBD to Cr^{3}, Cu^{2+}, and Ca^{2+}. Changes of fluorescence spectra and maximum emission intensity of MPNBD upon addition (0 to 1000 μM) of (a) Cr^{3+}, (b) Cu^{2+}, and (c) Ca^{2+} in ethanol were examined. The excitation wavelength was 470 nm and the monitored maximum photoluminescence (PL) emission wavelengths were 534 nm (Cr^{3+}, Cu^{2+}) and 540 nm (Ca^{2+}), respectively. a.u., arbitrary unit.

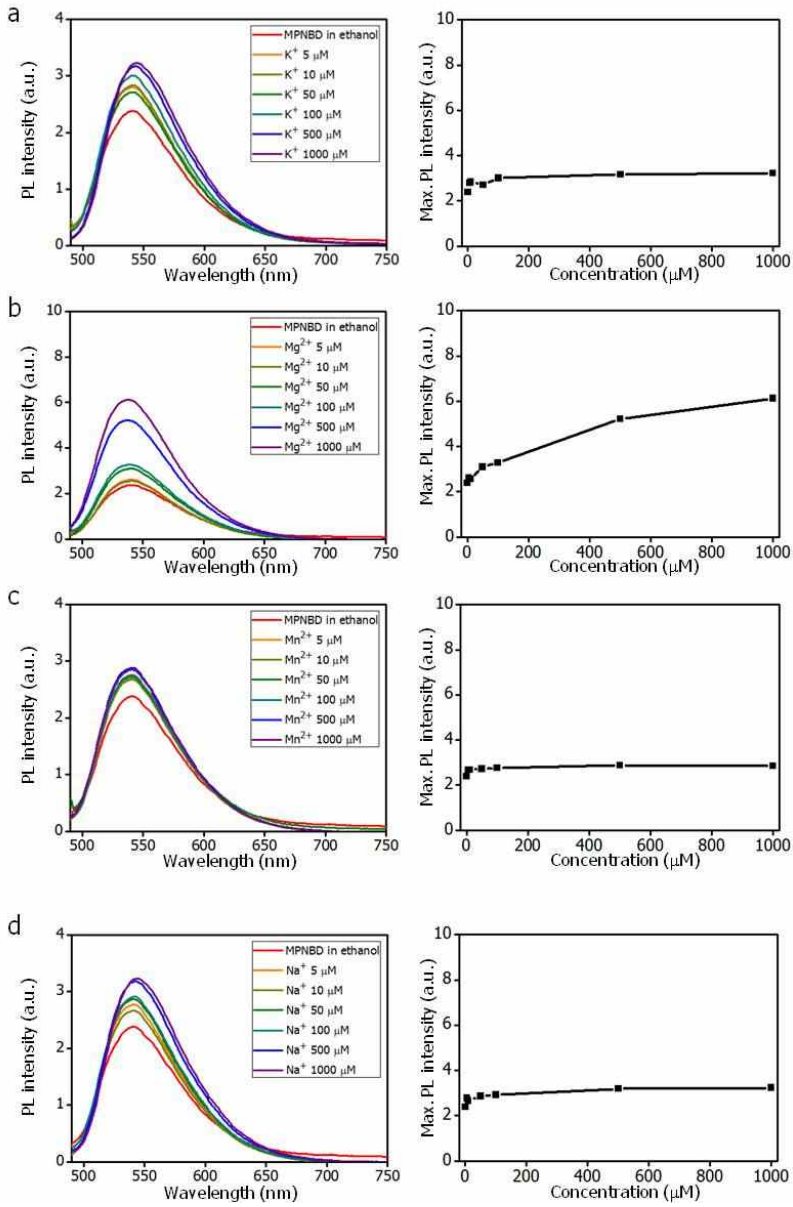
a
PL intensity (a.u.)
Wavelength (nm)
MPNBD in ethanol
K+ 5 μM
K+ 10 μM
K+ 50 μM
K+ 100 μM
K+ 500 μM
K+ 1000 μM
Max. PL intensity (a.u.)
Concentration (μM)
b
PL intensity (a.u.)
Wavelength (nm)
MPNBD in ethanol
Mg2+ 5 μM
Mg2+ 10 μM
Mg2+ 50 μM
Mg2+ 100 μM
Mg2+ 500 μM
Mg2+ 1000 μM
Max. PL intensity (a.u.)
Concentration (μM)
c
PL intensity (a.u.)
Wavelength (nm)
MPNBD in ethanol
Mn2+ 5 μM
Mn2+ 10 μM
Mn2+ 50 μM
Mn2+ 100 μM
Mn2+ 500 μM
Mn2+ 1000 μM
Max. PL intensity (a.u.)
Concentration (μM)
d
PL intensity (a.u.)
Wavelength (nm)
MPNBD in ethanol
Na+ 5 μM
Na+ 10 μM
Na+ 50 μM
Na+ 100 μM
Na+ 500 μM
Na+ 1000 μM
Max. PL intensity (a.u.)
Concentration (μM)

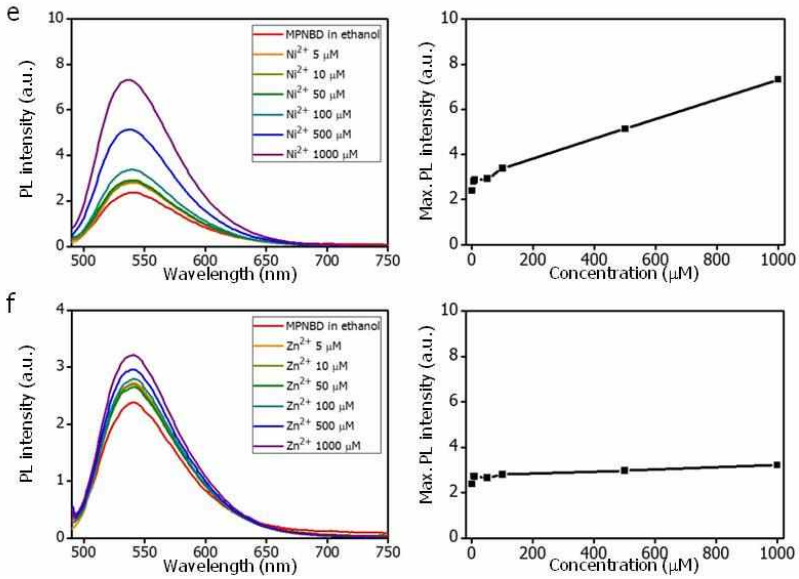

APPENDIX/Figure 3.6. Fluorescence responses of MPNBD to K^+, Mg^{2+}, Mn^{2+}, Na^+, Ni^{2+}, and Zn^{2+}. Changes of fluorescence spectra and maximum emission intensities of MPNBD upon gradual addition (0 to 1000 μM) of (a) K^+, (b) Mg^{2+}, (c) Mn^{2+}, (d) Na^+, (e) Ni^{2+}, and (f) Zn^{2+} in ethanol were examined. The excitation wavelength was 470 nm, and the monitored maximum photoluminescence (PL) emission wavelength was 541 nm. a.u., arbitrary unit.

Fluorescence responses of MPNBD to various metal ions in ethanol, including Fe^{3+} and Fe^{2+} were examined (Figure 3.2 and Figure 3.3-3.6). Notably, treatments with Fe^{3+} and Fe^{2+} induced obvious fluorescence turn-on responses at 533 nm (Figure 3.2). MPNBD showed different fluorescence responses to Fe^{3+} andFe^{2+}, depending on the concentration of ions. The emission intensity induced by Fe^{3+} was higher by approximately 6-fold than that induced by Fe^{2+} at low concentrations (<50 μM) (see Insets in Figure 3.2). In contrast, the emission intensities of Fe^{3+} and Fe^{2+} were similar at high

concentrations (>50 μM) (Figure 3.2).

The fluorescence signals enhanced by Fe^{3+} and Fe^{2+} were much higher than those enhanced by other metal ions that are plentiful in plants, such as K^{+}, Ca^{2+} and Mg^{2+} (Figure 3.5c and 3.6), suggesting that MPNBD is useful as a fluorescence probe for detection of iron ions in plants. The detection limit of MPNBD for Fe^{3+} was determined to be 8.08 μM (Figure 3.7), which is much lower than the detection limit of conventional histochemical staining methods.

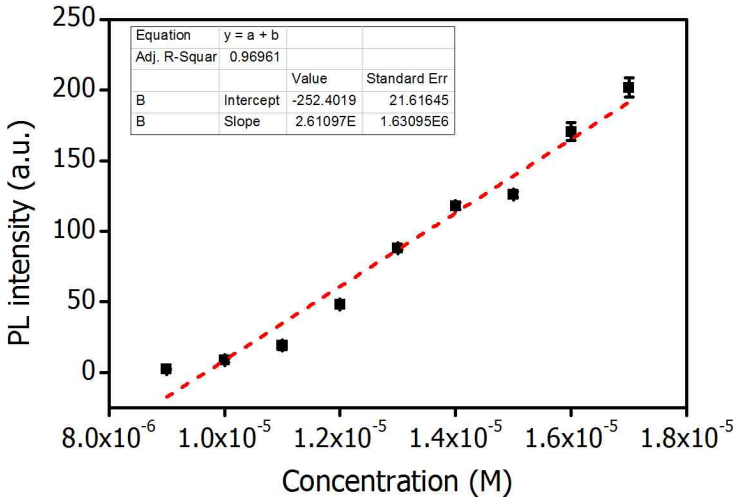

APPENDIX/Figure 3.7. Calibration curve of MPNBD-Fe^{3+} in ethanol solution. The excitation wavelength was 470 nm, and the monitored maximum photoluminescence (PL) emission wavelength was 533 nm. The detection limit (DL) of Fe^{3+} ions using MPNBD was determined from the following equation: $DL = K \times SD/S$, where K=3; SD is the standard deviation of the blank solution; S is the slope of the calibration curve. $DL = K \times SD/S$ = 3 x 0.07032/2.61 x 10^{7} = 8.08 x 10^{-6} M. The PL intensity was measured 3 times and averaged. Vertical bars indicate the standard error of the mean.

It was found that 50 μM Cr^{3+} elicited approximately half of the emission intensity by iron (Figure 3.5a). Since the concentration of Cr^{3+} is extremely low in plants, the fluorescence enrichment by Cr^{3+} would essentially be negligible in measuring the fluorescence enrichment of MPNBD by Fe^{3+} and Fe^{2+}. Fifty μM Cu^{2+} induced less than 1% of the emission intensity by iron (Figure 3.5b). Based on these results together with the relatively low concentration of Cu^{2+} compared to that of iron in plants, endogenous Cu^{2+} does not distort the sensing of iron by MPNBD.

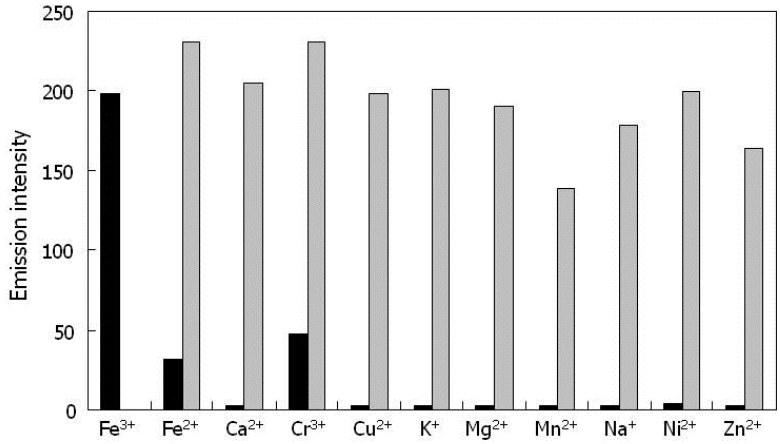

APPENDIX/Figure 3.8. Fluorescence response of MPNBD to various metal ions and to mixtures of Fe^{3+} and other metal ions. Fluorescence responses of MPNBD to Fe^{3+} (20 μM) or 20 μM of other metal ions (black bars) and to mixtures of Fe^{3+} (20 μM) and 20 μM of other metal ions (gray bars) in ethanol solution were compared.

To further evaluate the specific sensing of Fe^{3+} by MPNBD, competition experiments by including other metal ions in the assays were performed. The fluorescence intensities of the mixtures of Fe^{3+} and other metal ions were similar to that by Fe^{3+} alone (Figure 3.8). It was therefore concluded that the fluorescent turn-on probe MPNBD is suitable for the selective imaging of iron in plant tissues.

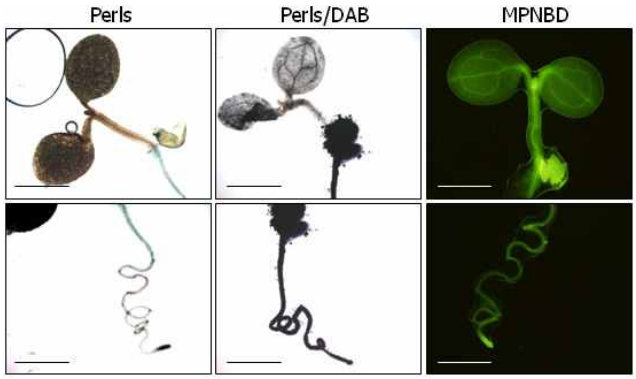

APPENDIX/Figure 3.9. Comparison of different iron detection methods in plants. Four-day-old whole *Arabidopsis* seedlings grown on 1/2 X Murashige & Skoog (MS) media containing 0.6% (w/v) agar (hereafter referred to as MS-agar plates) were subject to different iron detection methods as described in Table S1. The aerial plant parts are shown in the top panels, and the roots are shown in the bottom panels. Scale bars, 0.5 cm.

The validity of MPNBD as a fluorescent probe for the imaging of iron distribution in plants was examined by using the dicot model *Arabidopsis thaliana*. The *Arabidopsis* seedlings soaked in 50 μM MPNBD solution were subject to vacuum infiltration. The seedlings were then incubated in complete darkness and washed with ethanol before fluorescence microscopy. The Perls and Perls/DAB staining methods were also conducted in parallel for

comparative analysis using the *Arabidopsis* seedlings of the same age (Figure 3.9).

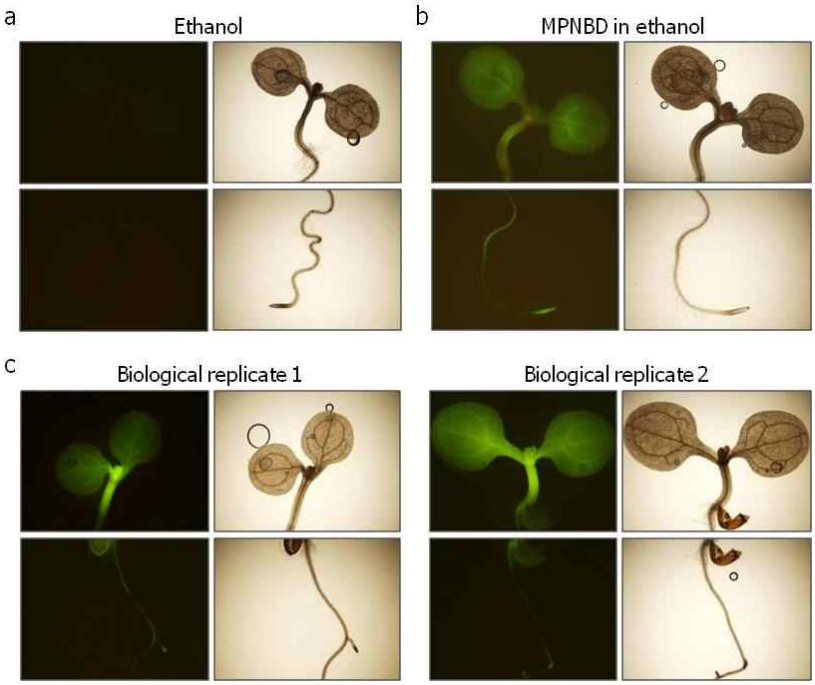

APPENDIX/Figure 3.10. Images of MPNBD-treated plants. Four-day-old whole *Arabidopsis* seedlings grown on ½ X Murashige & Skoog (MS) media containing 0.6% (w/v) agar (hereafter referred to as MS-agar plates) were treated with either ethanol (a) or 50 μM MPNBD in ethanol (b). The seedlings were visualized by optical and fluorescence microscopy. Fluorescence images are shown in the left panels and optical microscope images are shown in the right panels. Note that no fluorescent signals were detected in the ethanol-treated plants. To evaluate the reproducibility of the MPNBD-mediated fluorescent signals in plants, two additional plants (biological replicates 1 and 2) were treated with MPNBD independently under the identical conditions (c).

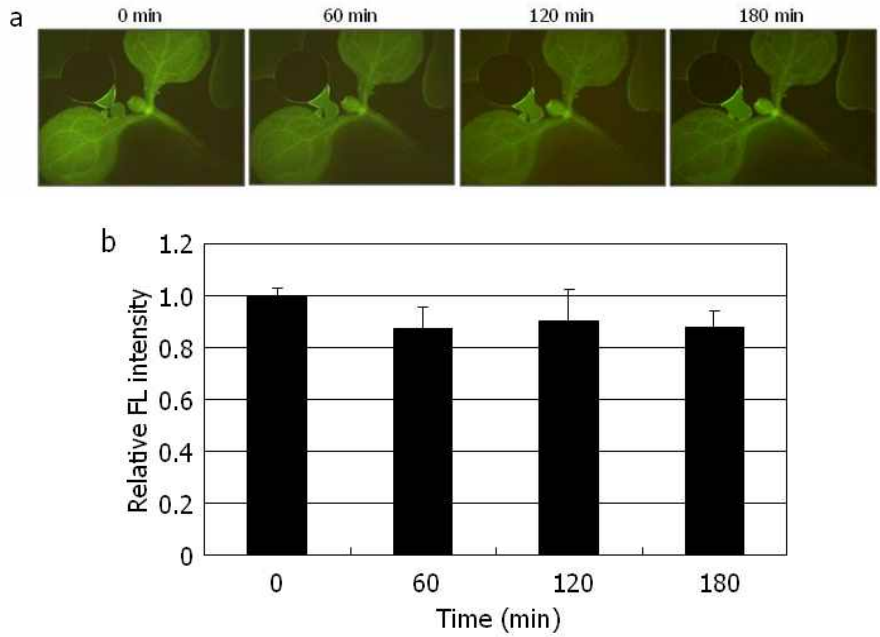

APPENDIX/Figure 3.11. Stability of MPNBD fluorescent probe. Four-day-old whole *Arabidopsis* seedlings grown on MS-agar plates were treated with 50 M MPNBD in ethanol, as described in Fig ure 3.9. (a) Fluorescence images obtained at the indicated time points after MPNBD treatments. (b) Quantification of the data in (a). The fluorescence (FL) intensity was measured using the ImageJ software (http://rsbweb.nih.gov/ij/), as described previously.[14, 17] Note that the fluorescent signals do not significantly diminish for up to 3 h.

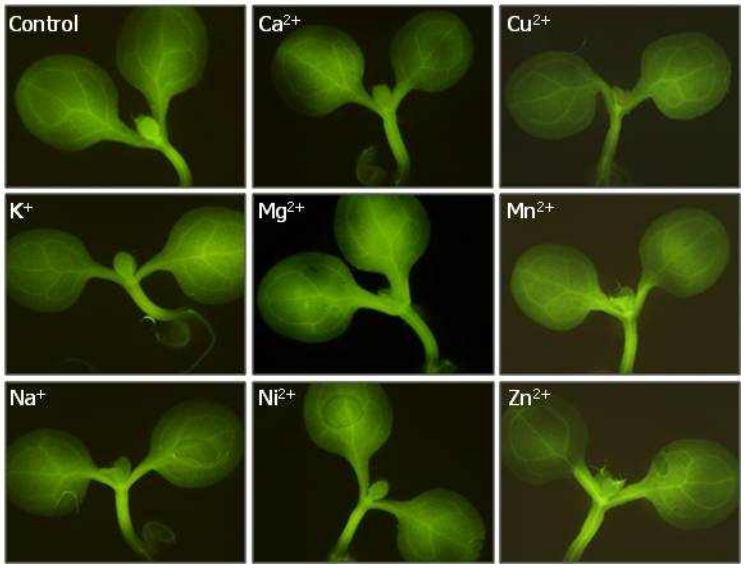

APPENDIX/Figure 3.12. Effects of various metal ions on the MPNBD imaging of iron in plants. Four-day-old whole *Arabidopsis* seedlings grown on MS-agar plates were treated with 500 μM of each metal ion for 12 h and treated with 50 μM MPNBD in ethanol, as described in Figure 3.10. Note that no significant changes in fluorescent signals were detected in the presence of other metal ions.

Significantly high fluorescence signals were reproducibly observed in the *Arabidopsis* plants treated with MPNBD (Figure 3.10.). However, no detectable signals were observed in mock-treated plants, indicating that autofluorescence does not interfere with the MPNBD-mediated fluorescence emission in plants. No significant diminishment of fluorescent signal even after 3h indicated that the MPNBD probe is relatively stable (Figure 3.11). In addition, the presence of other metal ions did not detectably interfere with the sensing of iron by MPNBD *in planta* (Figure 3.12). Cr^{3+} was not included in

the assays. Although MPNBD showed certain amount of fluorescence response to this metal ion (Figure 3.5a), its concentration is extremely low in plants.

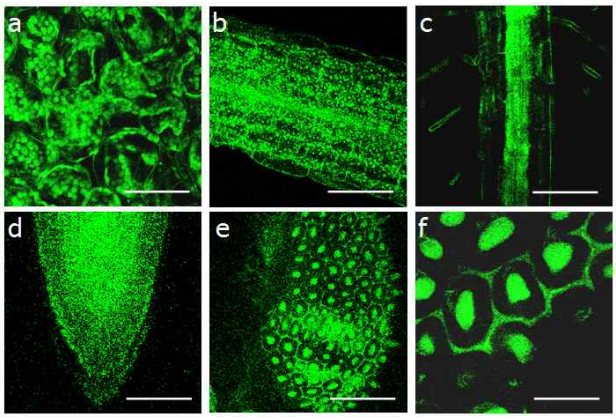

APPENDIX/Figure 3.13. Fluorescence images of plants treated with MPNBD. Four-day-old, whole *Arabidopsis* seedlings grown on MS-agar plates were treated with 50 μM MPNBD and visualized by fluorescence microscopy. (a) Fluorescence image of leaf epidermal cells. Scale bar, 60 μm. (b) Fluorescence image of the stem. Scale bar, 120 μm. (c and d) Fluorescence image of the root stem (c) and the root tip region (d). Scale bars, 110 μm (c) and 60 μm (d). (e and f) Fluorescence images of developing seed. *Arabidopsis* seed were cold-imbibed for 3 days in complete darkness and allowed to germinate for 12 hours before MPNBD treatments. An enlarged view (f) of the developing seed (e) was shown. Scale bars, 110 μm (e) and 40 μm (f).

The Perls staining gave signals primarily in the root tissues. However, it failed to detect discernible signals in the aerial plant parts, as reported previously.[18] The improved Perls/DAB staining produced signals from both the roots and aerial plant parts. However, it suffered from low resolution, as this detection method is based on black precipitates. Notably, the MBNBD-based fluorescence turn-on assays exhibited high fluorescence signals throughout all plant organs, including the leaves, within 20 min following MPNBD treatments (Figure 3.9).

A prominent feature of the MPNBD-based fluorescence detection method is the high-resolution imaging of iron distribution in the leaves (Figure 3.9). The localized distribution of iron in the leaf tissues is controversial. It has been reported that approximately 70% of the total iron measured in the leaves is found in the chloroplasts.[19] On the other hand, a considerable amount of iron has also been detected in the vasculature of the leaves.[20] The MPNBD fluorescence method visualized high-resolution signals in both the chloroplasts and vasculature of the leaves (Figure 3.13a and Figure 3.9, respectively), demonstrating that iron accumulates in both the chloroplasts and vasculature of the leaves. There was also high-level fluorescence emission in the vasculature of the stems and roots after MPNBD treatments (Figure 3.13b and Figure 3.13c, d, respectively). Moreover, the MPNBD-assisted high-resolution imaging revealed that iron accumulates at a high level in the epidermal cells of the seed coat (Figure 3.13e), especially in the volcano-shaped columella and hexagonal cell wall (Figure 3.13f). It has been reported that Ca^{2+} is deposited in a similar pattern in the seed coat.[21] Therefore, it is suspected that the fluorescence emission might be from MPNBD-Ca^{2+} complex. However, the fluorescence enrichment of MPNBD by Ca^{2+} was beyond the detection limit of our assay conditions (Figure 3.5c), indicating

that fluorescence emission in the seed coat was due to iron deposits. Nonetheless, the biological function of iron deposited in the seed coat is currently unknown.

The fluorescence turn-on probe MPNBD is able to image the distribution of total iron in all plant tissues with high resolution and high sensitivity (Table 3.1). In addition, the MPNBD-assisted fluorescence detection method can be readily applied to all plant organs with a simple procedure and low cost. Furthermore, due to the high binding affinity of MPNBD to iron, it is unnecessary to treat plant samples with acids to release iron from iron complexes prior to MPNBD treatment. Since the MPNBD method is based on fluorescence emission, sectioning of plants tissues is not necessary for small plants, such as *Arabidopsis*.

APPENDIX/Table 3.1. Procedures of different iron detection methods in plants.

Perls[7]	**Perls/DAB**[7, 22]	**MPNBD**
1. Vacuum infiltration for 15 min in 4% HCl/4% $K_4Fe(CN)_6$.	1. Vacuum infiltration for 15 min in 4% HCl/4% $K_4Fe(CN)_6$.	1. Wash with ethanol.
2. Incubation at room temperature for 30 min.	2. Incubation at room temperature for 30 min.	2. Vacuum infiltration for 5 min in 50 μM MBNBD in ethanol.
3. Wash with deionized water.	3. Wash with deionized water.	3. Incubation at room temperature for 10 min.
	4. Incubation for 1 h in 0.01M NaN_3 / 0.3% H_2O_2 in methanol.	4. Wash with ethanol.
	5. Wash with 0.1 M phosphate buffer (pH 7.4).	
	6. Incubation for 30 min in 0.025% DAB, 0.005% H_2O_2, 0.005% $CoCl_2$ in 0.1M phosphate buffer (pH 7.4).	
	7. Wash with deionized water.	
~ 1 h	~ 3h	< 20 min
Poor staining in the leaves Low sensitivity (Detection limit : 375 μM)	Moderate sensitivity (Detection limit : 100 μM) Longer time	High resolution and sensitivity (Detection limit : 8.44 μM) Fast and cheap
Ref 7	Ref 7 Ref 21	This work

3.4 Conclusions

The MPNBD fluorescence method provides high-resolution imaging of total iron in plant tissues. Therefore, dynamic information on the redox chemistry of iron can be obtained if it is applied in conjunction with Fe^{3+}- and Fe^{2+}-specific fluorescent probes. This method is potentially useful for the isolation of mutant plants that are defective in iron metabolism and deposit in a high-throughput manner. Moreover, this powerful method can be immediately adopted for the detection of iron distribution in animal cells or sectioned tissues.

Acknowledgements

MPNBD was synthesized by Hak-Sung Jung. Fluorescence imaging test in plant was done by Mi-Jeong Park, Young-Ju Kwon, and Prof. Chung-Mo Park.

3.5 References

[1] Briat, J.-F.; Curie, C.; Gaymard, F., *Curr. Opin. Plant Biol.* **2007**, *10*, 276-282.

[2] Jeong, J.; Guerinot, M. L., *Trends Plant Sci.* **2009**, *14*, 280-285.

[3] Long, T. A.; Tsukagoshi, H.; Busch, W.; Lahner, B.; Salt, D. E.; Benfey, P. N., *Plant Cell* **2010**, *22*, 2219-36.

[4] Kim, S. A.; Punshon, T.; Lanzirotti, A.; Li, L.; Alonso, J. M.; Ecker, J. R.; Kaplan, J.; Guerinot, M. L., *Science* **2006**, *314*, 1295-8.

[5] Lanquar, V.; Lelievre, F.; Bolte, S.; Hames, C.; Alcon, C.; Neumann, D.; Vansuyt, G.; Curie, C.; Schroder, A.; Kramer, U.; Barbier-Brygoo, H.; Thomine, S., *EMBO J* **2005**, *24*, 4041-51.

[6] Seo, P. J.; Park, J.; Park, M. J.; Kim, Y. S.; Kim, S. G.; Jung, J. H.; Park, C. M., *Biochem. J.* **2012**, *442*, 551-61.

[7] Roschzttardtz, H.; Conejero, G.; Curie, C.; Mari, S., *Plant Physiol.* **2009**, *151*, 1329-38.

[8] Roschzttardtz, H.; Conéjéro, G.; Divol, F.; Alcon, C.; Verdeil, J.-L.; Curie, C.; Mari, S., *Front. Plant Sci.* **2013**, *4,* 1-10.

[9] Bournier, M.; Tissot, N.; Mari, S.; Boucherez, J.; Lacombe, E.; Briat, J. F.; Gaymard, F., *J. Biol. Chem.* **2013**, *288*, 22670-22680.

[10] Xiao, Y.; Qian, X., *Tetrahedron Lett.* **2003**, *44*, 2087-2091.

[11] Liu, S.-R.; Wu, S.-P., *Sensor. Actuat. B-Chem.* **2012**, *171*, 1110-1116.

[12] Sahoo, S. K.; Sharma, D.; Bera, R. K.; Crisponi, G.; Callan, J. F., *Chem. Soc. Rev.* **2012**, *41*, 7195-7227.

[13] Goswami, S.; Aich, K.; Das, S.; Das, A. K.; Sarkar, D.; Panja, S.; Mondal, T. K.; Mukhopadhyay, S., *Chem. Commun.* **2013**, *49*, 10739-10741.

[14] Hirayama, T.; Okuda, K.; Nagasawa, H., *Chem. Sci.* **2013**, *4*, 1250-1256.

[15] Ramachandram, B.; Samanta, A., *J. Phys. Chem. A* **1998**, *102*, 10579-

10587.

[16] Mistri, T.; Alam, R.; Dolai, M.; Mandal, S. K.; Khuda-Bukhsh, A. R.; Ali, M., *Org. Biomol. Chem.* **2013**, *11*, 1563-9.

[17] Mancuso, M. R.; Davis, R.; Norberg, S. M.; O'Brien, S.; Sennino, B.; Nakahara, T.; Yao, V. J.; Inai, T.; Brooks, P.; Freimark, B.; Shalinsky, D. R.; Hu-Lowe, D. D.; McDonald, D. M., *J. Clin. Invest.* **2006**, *116*, 2610-2621.

[18] Green, L. S.; Rogers, E. E., *Plant Physiol.* **2004**, *136*, 2523-31.

[19] Shikanai, T.; Muller-Moule, P.; Munekage, Y.; Niyogi, K. K.; Pilon, M., *Plant Cell* **2003**, *15*, 1333-46.

[20] Stacey, M. G.; Patel, A.; McClain, W. E.; Mathieu, M.; Remley, M.; Rogers, E. E.; Gassmann, W.; Blevins, D. G.; Stacey, G., *Plant Physiol.* **2008**, *146*, 589-601.

[21] Voiniciuc, C.; Dean, G. H.; Griffiths, J. S.; Kirchsteiger, K.; Hwang, Y. T.; Gillett, A.; Dow, G.; Western, T. L.; Estelle, M.; Haughn, G. W., *Plant Cell* **2013**, *25*, 944-959.

[22] Meguro, R.; Asano, Y.; Odagiri, S.; Li, C.; Iwatsuki, H.; Shoumura, K., *Arch. Histol. Cytol.* **2007**, *70*, 1-19.

Korean Abstract

나노입자는 양자효과와 넓은 표면적으로부터 기인한 새로운 특성으로 인하여 광범위하게 연구되고 있다. 나노입자가 가진 특성들을 다양한 분야로 적용 시킬 수 있으며 그 중, 고분자 나노복합체는 고분자 매트릭스 내에 나노미터 크기를 갖는 무기입자들을 혼합한 것으로, 고분자의 유연성이나 가공의 용이성과 같은 장점들을 저해하지 않고, 열적 · 기계적 · 전기적 특성을 향상시킬 수 있다.

열적 · 기계적 · 전기적 특성이 우수한 금속 산화물 (SiO_2, TiO_2, $BaTiO_3$)의 표면을 각각의 고분자의 단량체와 구조적으로 유사한 리간드로 표면을 개질하여, 나노입자가 균일하게 분산된 SiO_2–triacethylcellulose (TAC), SiO_2–polyimide (PI), TiO_2–polyvinylphenol (PVP) 그리고 $BaTiO_3$–PVP 나노복합체를 합성하였다. SiO_2를 이용하여 고분자의 유리전이온도와 결정온도, 융해온도, 열팽창계수 등의 열적 특성들을 변화시킬 수 있었고, 강도와 탄성률과 같은 기계적 특성을 향상 시킬 수 있었다. 또한 유전상수가 큰 TiO_2와 $BaTiO_3$를 이용하여 유전상수가 증가된 고분자 나노복합체를 합성할 수 있었다. 뿐만 아니라 나노입자의 작은 크기와 높은 분산성으로 인하여 고분자 나노복합체의 투과율을 유지할 수 있었다. 고분자 나노 복합체 내의 나노입자 함량에 따른 각각의 특성을 분석하였고, 유전상수가 증가된 고분자 나노복합체를 유기박막 트랜지스터의 절연막으로 이용하여 전기적 특성이 향상된 소자를 얻을 수 있었다.

주요 핵심어: 고분자 나노복합체, 나노입자, 표면 개질, 열적·기계적 특성, 전기적 특성, 절연막

학번: 2008-20310